UNIVERSITÀ
DEGLI STUDI
DI PADOVA

Università degli Studi di Padova

Dipartimento di Astronomia

SCUOLA DI DOTTORATO DI RICERCA IN ASTRONOMIA

CICLO XXII

Spectral properties and photoionization models of the NLR in Seyfert galaxies

Direttore della Scuola: Ch.mo Prof. Giampaolo Piotto

Supervisore: Ch.mo Prof. Piero Rafanelli

Dottorando: Luigi Vaona

A Selene, camminatrice in montagna e nella fantasia,
Elio, grande disegnatore di serpenti e pipistrelli,
Zeno, in viaggio con il trattore per il mondo,
e Francesco, che ha appena iniziato ad esplorare.

Voglio esprimere i ringraziamenti più sinceri al Prof. Piero Rafanelli, al dott. Stefano Ciroi e al dott. Francesco Di Mille per il fondamentale supporto scientifico, per le preziose discussioni che hanno portato alla produzione di questa tesi e per il grande sostegno dimostratomi durante i tre anni trascorsi presso il Dipartimento di Astronomia.

Desidero ringraziare la dott.ssa Sonia Temporin per l'aiuto e gli importanti suggerimenti fornitemi durante la stesura della tesi. Un grazie ai colleghi e al personale del Dipartimento di Astronomia che durante il periodo del dottorato non sono mai venuti meno con il loro supporto professionale e con la loro amicizia. Infine un grazie particolare a mia moglie Anita che ha contribuito con la sua consulenza alla realizzazione dei codici sviluppati in questa tesi e a tutti gli amici che in vari modi mi hanno incoraggiato e sostenuto durante questa esperienza.

Padova 19 gennaio 2010 Luigi Vaona

Riassunto

Sebbene le proprietà della Narrow Line Region (NLR) dei Nuclei Galattici Attivi (AGN) siano stati studiati in modo approfondito da molti autori negli ultimi decenni, molte questioni sono ancora aperte, come l'origine del gas e le possibili differenze tra i diversi tipi di AGN. Noi qui intendiamo investigare le NLR delle galassie di Seyfert attraverso la misura di un grande campione di spettri e il confronto con modelli di fotoionizzazione. La fotoionizzazione da una sorgente non termica è il meccanismo di ionizzazione piú accreditato nel caso delle NLR. Infatti, molti lavori sostengono questa ipotesi con misure dirette e con il confronto con i modelli.

La tesi si basa su tre punti fondamentali: i) la selezione degli spettri, la relativa misura e classificazione; ii) l'analisi spettroscopica e la determinazione dei parametri; iii) i modelli di fotoionizzazione e il loro confronto con gli spettri osservati.

Lo scopo principale è la raccolta di un vasto campione di spettri di Seyfert 2 e di Seyfert intermedie con alto rapporto segnale rumore in modo tale da misurare in modo accurato un grande numero di righe.

Sono stati selezionati 3154 spettri dalla Sloan Digital Sky Survey - DR7 con un nuovo diagramma diagnostico, basato sui rapporti delle righe di emissione dell'Ossigeno (diagramma degli ossigeni). Tutte le righe in emissione, incluse le componenti larghe (broad) sono state misurate tramite un codice da noi sviluppato, chiamato GGFIT, dopo la sottrazione della componente stellare. Per ogni oggetto sono stati determinati i parametri fisici, come arrossamento, luminosità, temperatura, densità, dispersione di velocità del gas e delle stelle. Inoltre è stata fornita una stima della massa e del raggio della NLR, dell'energia cinetica del gas ionizzato, e del tasso di accrescimento della massa del buco nero.

Usando il codice di fotoionizzazione, CLOUDY, siamo stati in grado di riprodurre gli spettri osservati e di derivare i parametri di ingresso più probabili per le differenti tipologie di modelli. I parametri più importanti sono: la metallicità, l'indice di "power-law", il parametro di ionizzazione, la densità elettronica, la densità di colonna e il rapporto fra la quantità di polvere e di gas. Il confronto fra i modelli e gli spettri osservati è stato fatto tramite il test χ^2 sui flussi delle righe in emissione.

Dall'analisi delle righe in emissione, dalle proprietà fisiche misurate e dal confronto con i modelli appare chiaro che la distribuzione più probabile del gas è data da un mezzo a bassa densità ($N_e \sim 1 \div 10\, cm^{-3}$) che circonda nubi con densità maggiore ($N_e > 4 \times 10^5\, cm^{-3}$). La quantità di polveri dovrebbe essere ridotta nelle zone interne della NLR. Le correlazioni fra le righe di emissione suggerisce una ionizzazione stratificata, con nubi di alta e bassa ionizzazione. Nel campione di Seyfert intermedie abbiamo trovato un'estinzione ridotta (il cui valore mediano è $A_V \sim 1.0\, mag$), nessuna correlazione nella dispersione di velocità fra gas e componente stellare e la presenza delle righe coronali del ferro VII, risultati che suggeriscono fortemente che stiamo guardando in profondità nella NLR. D'altro canto nel campione delle Seyfert 2 troviamo una maggiore estinzione (il cui valore mediano è $A_V \sim 1.5\, mag$) e una parziale correlazione nella cinematica fra gas e componente stellare. Tutto questo è consistente con il Modello Unificato. La riga $[OIII]5007$ appare asimmetrica nella maggior parte dei casi, specialmente nel campione delle Seyfert intermedie. Il 75% delle righe $[OIII]5007$ asimmetriche mostra una asimmetria blu. Questo è consistente con un deflusso di gas ionizzato in un mezzo ricco di polveri. Infine, i modelli sembrano indicare un alto grado di metallicità della NLR ($1 \div 2.5\, Z_\odot$) e questo suggerisce che nella maggior parte dei casi il gas ionizzato appartiene alla galassia ospite.

Abstract

Although the properties of Narrow Line Region (NLR) of Active Galactic Nuclei (AGN) have been deeply studied by many authors in the past two decades, many questions are still open, like the origin of the gas and possible differences between different types of AGN. Here we intend to explore the NLR of Seyfert galaxies by means of measurements of a large set of observed spectra and comparison with photo-ionization models. The photo-ionization by a non-thermal source is the most reliable ionization mechanism for the NLR. Indeed, many works support this hypothesis with direct measurements and comparisons with models.

This thesis is based on three fundamental steps: i) the spectra selection, their measurement and spectroscopic classification of the targets; ii) the spectroscopic analysis and the physical parameters determination; iii) the photo-ionization models and their comparison with the observed spectra.

The main goal is to collect a large statistical spectroscopic sample of Seyfert 2 and Intermediate-type Seyfert galaxies having a high signal-to-noise ratio in order to take advantage of a high number of emission lines to be accurately measured.

3154 spectra were selected from Sloan Digital Sky Survey - DR7 with a new diagnostic diagram based on the Oxygen emission-line ratios (Oxygen diagram). All the emission lines, broad components included, were measured by means of a self-developed code, named GGFIT, after the subtraction of the stellar component. Physical parameters, such as internal reddening, luminosity, temperature, density, gas and stellar velocity dispersion were determined for each object. Furthermore, an estimate of mass and radius of the NLR, kinetic energy of the ionized gas, and mass accretion rate of the black-hole was provided.

Using the photo-ionization code, CLOUDY, we were able to reproduce the observed spectra, hence the most likely input parameters for different kinds of photo-ionization models were determined. The main parameters are metallicity, power-law index, ionization parameter, electron density, column density and dust-to-gas ratio. The comparison between models and observed spectra was performed by χ^2 test on the emission-line fluxes.

From the emission-line analysis, the measured physical properties and the comparison with the models it is clear that the most likely gas distribution is given by a low density medium ($N_e \sim 1 \div 10\, cm^{-3}$) surrounding clouds with higher density ($N_e > 4 \times 10^5\, cm^{-3}$). The dust should be reduced in the inner part of NLR. The emission line correlations suggest a stratified ionization, with high and low ionization clouds. In the Intermediate-type Seyfert sample we find lower extinction (the median value is $A_V \sim 1\, mag$), no correlation between gas and stellar velocity dispersion and the presence of the [FeVII] coronal lines, results which strongly suggest that we are looking deep inside the NLR. On the other hand in the Seyfert 2 sample we find higher extinction (the median value is $A_V \sim 1.5\, mag$) and a partial correlation between gas and stars kinematics. All is consistent with the Unified Model. The $[OIII]5007$ line is asymmetric in the vast majority of the cases, especially in the Intermediate-type Seyfert sample. 75% of the $[OIII]5007$ asymmetric lines show a blue asymmetry. This is consistent with gas outflow in a medium rich in dust. Finally, the models seem to indicate a generally high metallicity of the NLR ($1 \div 2.5\, Z_\odot$) and this suggests that in most of the cases the ionized gas belongs to the host galaxy.

Contents

Introduction

The ionized gas, characterized by a prominent emission-line spectrum, is one of the most powerful tools to study the physics of the interstellar medium and the ionizing sources, and a fundamental instrument in the investigation of the chemical evolution.

Classical examples of clouds of ionized gas, or gaseous nebulae, are HII regions, planetary nebulae, nova and supernova remnants. These objects differ greatly in origin, mass and evolution but the physical processes involved are quite similar. A source of ionizing photons, equilibrium between ionization and recombination and thermal equilibrium are the fundamental ingredients. Much of the known physics about these objects can be applied to the nuclei of Seyfert galaxies, even if additional processes, that involve high-energy photons must be taken into account (i.e. inner-shell photoionization and collisional excitation of H^0). Moreover, the ionized gas in Seyfert galaxies extends over *kpc* scales.

Seyfert galaxies are characterized by a bright star-like nucleus, whose spectrum shows emission lines covering a wide range of ionization. They belong to the radio-quiet AGN family (but this does not exclude the presence of radio activity). They are classified in two main groups: Seyfert 1 and Seyfert 2. The classification is based on the Full-Widths at Half Maximum (FWHM) of the emission lines: Seyfert 1, when the FWHM of recombination lines (HI, HeI and HeII) is higher than $1000\,km/s$ (broad lines) and the FWHM of forbidden lines is few hundred km/s (narrow lines), and Seyfert 2, when the FWHM of recombination and forbidden lines is the same, few hundred km/s. The difference between the groups is not well defined, in fact some spectra show recombination lines with both components, a narrow emission line overlapped to a broad emission line. These objects are generally classified as Seyfert 1.5 and called Intermediate-type Seyfert galaxies. Depending on the visibility of the broad component the classification may be further subdivided into Seyfert 1.2, when the narrow component is at the limit of the detection, Seyfert 1.8, when the broad component is very weak compared to the narrow component, but visible in H_α and H_β, and Seyfert 1.9, when the broad component is visible only in H_α, but not in H_β (Osterbrock & Ferland, 2006).

The narrow emission-lines come from the Narrow Line Region (NLR). The aim of this PhD thesis is to verify the properties of the NLR founded in the last two decades, through a detailed analysis of a large sample of Seyfert spectra, and to explore possible differences between Seyfert 2 and Intermediate-type Seyfert galaxies. The analysis will concern correlations among emission lines, reddening and emission line intensity distributions, and it will take advantage also of the weak lines, which are too often neglected. We will analyze the $[OIII]4959,5007$ and H_β asymmetries with the aim to investigate the statistics of the ionized gas outflows occurring in a dust rich medium. A comparison between the samples will be performed upon characteristic parameters such as mass of the gas, energy, life time-scale and mass accretion rate. Assuming photoionization by the central source as the main ionization mechanism, we will reproduce the observed spectra through single cloud and composite clouds models, which take into account the presence of dust inside the NLR. We will show that with these models it is possible to determine the physical parameters of the ionized gas, and in particular the metallicity content. This parameter plays a fundamental role in searching for the gas origin in the NLR.

This work is organized in five chapters: the first one is an overview of the spectroscopic and morphologic properties of the NLR, with particular attention to the ionized gas properties and its origin. In the second chapter the selection criteria of the samples are described, together with a new diagnostic diagram, measurements and spectra classification. A section concerns the new code dedicated to automatically measure all the emission-line of a spectrum by using a multi-Gaussian fitting. The spectra classification, in Seyfert 2 and Intermediate-type Seyfert, is described in the last section of the second chapter. The emission line analysis and the NLR physical characteristics are treated in chapter 3 and 4 respectively. In chapter 5, we present photo-ionization models, the comparison netween models and observations, the physical parameters determination and finally a suggestion about some diagnostic diagrams useful to determine the physical conditions of the ionized gas by extending the analysis in the UV and NIR ranges.

Note: figure labels are written without special characters, subscripts, upperscripts and greek characters, therefore unit of measure, math symbols, spectral lines or other are written as in the following examples: H_α =Ha, H_β =Hb, $erg\,s^{-1}\,cm^{-2}\,\mathring{A}^{-1}$ = erg/s/cm2/A, χ^2 = chi2, σ =sig, etc...

Chapter 1

The Narrow-Line Regions of Seyfert galaxies

In order to describe the probable structure of a Seyfert nucleus, we adopt the diagram introduced by Wilson (1992) (Figure 1.1). The main components are: a central source, the Broad-Line Region (BLR), a molecular dusty torus, the Narrow-Line-Region (NLR) and the Extended NLR (ENLR). The BLR has a typical size $< 1\,pc$ and it is surrounded by an optically thick torus. The torus confines the escaping ionizing radiation into two oppositely directed cones (see e.g. Storchi-Bergmann et al., 1992; Kriss et al., 1997; Pogge & De Robertis, 1993; Capetti et al., 1999; Tsvetanov & Walsh, 1992; Ferruit et al., 1999; Miyaji et al., 1992; Veilleux et al., 1993; Falcke et al., 1996; Wilson & Tsvetanov, 1994). Inside the cones the gas is directly ionized by the central source. This region is probably made of local gas and plasma which is ejected in the form of jets or discrete "plasmoids", along the rotation axis of the torus (Wilson & Tsvetanov, 1994), or winds which are driven by radiation pressure (Komossa et al., 2008, and references cited therein). This model, called Unified Model and based on the spectropolarimetric analysis of NGC 1068 performed by Antonucci & Miller (1985), is the most accepted AGN picture (Antonucci, 1993). The Unified Model is able to explain the main different characteristics of Seyfert 1 and Seyfert 2 galaxies. In the first case the torus is seen face on, then the BLR is directly observable, in the second case the line of sight intercepts the torus and the BLR is not visible.

In the last two decades, the Unified Model has been tested through multi-wavelength observations. Seyfert 2 galaxies have shown more complicated properties than previously believed: hidden broad-lines revealed in the polarized light (HBLR S2s), absence of permitted broad emission-lines in polarized light (Non-HBLR S2s), X-ray absorbed and non-absorbed HBLR S2s, X-ray absorbed and non-absorbed Non-HBLR S2s. Examples of different Seyfert 2 galaxies can be found in Ghosh et al. (2007) and Haas et al. (2007), while Table 1 from Wang & Zhang (2007) contains a complete list of the categories and observed properties of Seyfert galaxies. Therefore, it is very likely that other parameters have to be taken into account within the classical scheme, like the black-hole mass, the opening angle of torus and the gas-to-dust ratio in the torus (Wang & Zhang, 2007), even if the orientation of the torus remains the fundamental parameter.

Before Hubble Space Telescope observations no detailed structures were visible in the NLR, only a bright nucleus. In fact, if we assume $0.1 - 1\,kpc$ as typical NLR size, when the distance of an AGN is larger than $\sim 200\,Mpc$ ($z \sim 0.05$), the scale is larger than $1\,kpc/arcsec$ and with ground based telescopes it becomes difficult to analyze the NLR morphology even

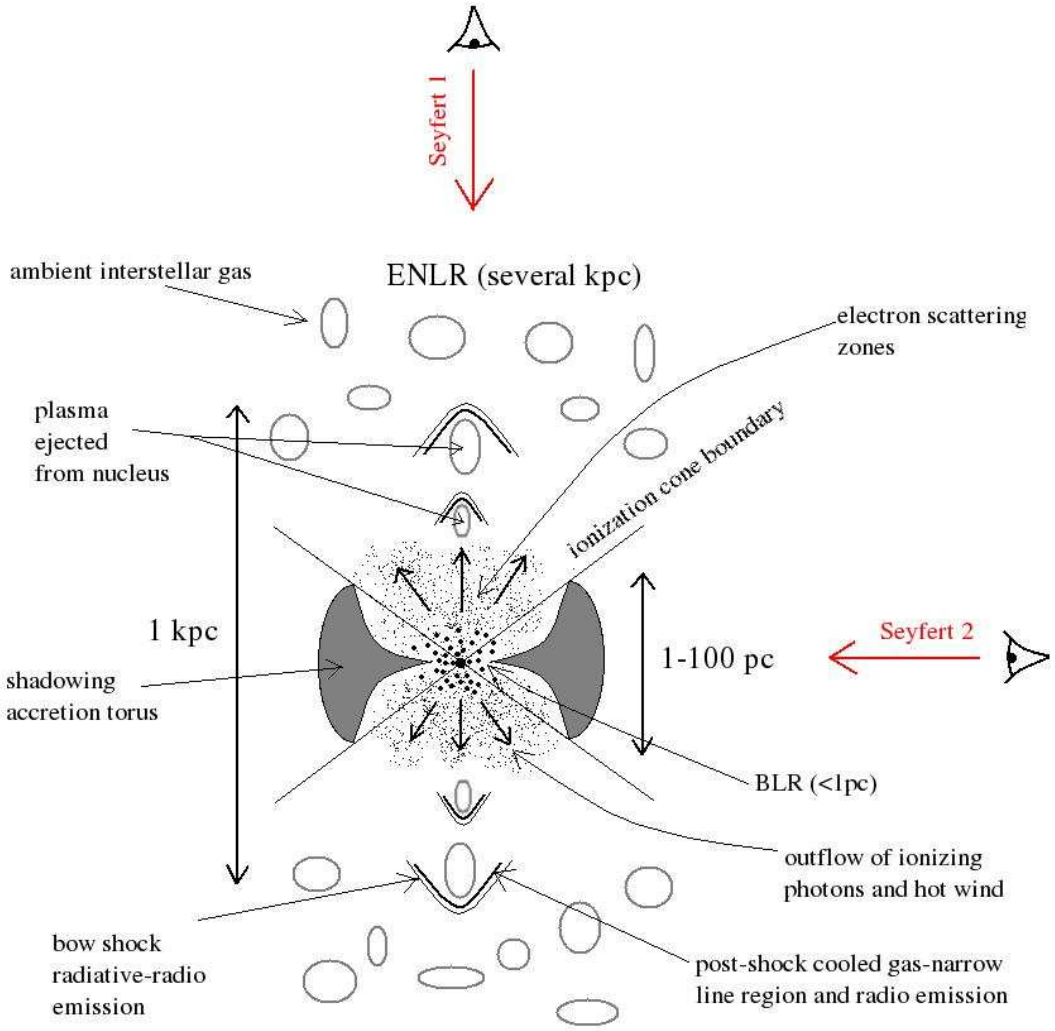

Figure 1.1: A schematic diagram of a Seyfert nucleus with the components descripted in the text, from Wilson (1992). The red arrows are the lines of sight, when the turus is seen face-on we have a Seyfert 1, when it is seen edge-on we have a Seyfert2.

in case of very good seeing conditions. The resolution of a ground based telescope permits only the analysis of the Extended Narrow-Line Region (ENLR), which is several kpc wide. The ENLR is characterized by FWHM$< 50\,km/s$ and high excitation gas, its spectrum is similar to that of the NLR (Unger et al., 1987). Deep CCD images of few nearby galaxies made through narrow band interference filters have revealed an extended structure very rich of gas clouds surrounding the active nucleus (Pogge, 1988, 1989; Tadhunter & Tsvetanov, 1989). With the advent of HST, it was possible to observe that ionization cones (Afanasiev et al., 2007; Wilson, 1997, and references therein) are in many cases closely associated with the radio jets and lobes (Wilson & Tsvetanov, 1994), and dust lanes (Martini et al., 2003a,b).

In the AGN framework (Lawrence, 1987) the NLR is characterized by low density clouds ($N_e \sim 10^2 - 10^6\,cm^{-3}$), temperature $T_e \sim 10000K$, size $\sim$ 1 kpc and Full-With at Half Maximum (FWHM) of the emission-lines in the range $\sim 200 - 1000\,km/s$. The gas is ionized by a non-thermal power-law spectrum from a central source even if other contributions should be taken into account, such as shocks (Dopita & Sutherland, 1995) and photoionization by star-forming regions near to the nucleus (Hill et al., 1999, composite galaxies).

Spatially resolved emission-line spectroscopy is a powerful tool to determine the physical conditions in the NLR and ENLR of AGNs (Wilson et al., 1989; Robinson et al., 1994; Radovich et al., 1998; Schulz et al., 1999; Temporin et al., 2003; Ciroi et al., 2005, e.g.). The electron density, determined using $[SII]6716, 6731$ doublet, show a decrement from the inner regions outwards, the same trend is observed in the ionization level (Bennert et al., 2006, 2007). The ionization level is defined by the ionization parameter U, which is the ratio between the number of ionizing photons at distance r from the source and the hydrogen density. It is expressed with the following formula

$$U = \frac{Q_{ion}}{c\,r^2\,N_H} \tag{1.1}$$

where Q_{ion} is the number of ionizing photons per second emitted by the source. An emission-line ratio which is directly connected with U is $[OII]3727/[OIII]5007$. The temperature is determined usually for the nuclear spectrum, where the S/N ratio is high, because of the faintness of the involved lines ($[OIII]4363$, $[OII]7325$, $[SII]4072$, $[NII]5755$). A great difference in temperature is measured between Seyfert 2 and Seyfert 1, $T_e \sim 10000K$ and $T_e > 20000K$ respectively. This difference has been interpreted by Osterbrock (1978) as a difference in densities ($N_e \sim 10^{6-7} cm^{-3}$ for Seyfert 1 galaxies and $N_e < 10^5 cm^{-3}$ for Seyfert 2).

Even if some spectroscopic differences between Seyfert 1 and Seyfert 2 have been found in visible narrow emission-line ratios (Zhang et al., 2008) and in IR emission and absorption lines (Deo et al., 2007), according to the Unified Model the NLR physical characteristics could be similar for all Seyfert galaxies. A purpose of this thesis is to point out possible differences in the NLR between Seyfert 2 and Intermediate-type Seyfert galaxies. In fact in Balmer emission lines of Intermediate-type Seyfert spectra it is possible to separate the broad from the narrow component. Two examples of optical spectra of these kinds of Seyfert galaxies are shown in Figure 1.2. They are useful to see the main emission-lines which will be treated in the analysis.

In order to determine the physical characteristics the first issue to fix is the ionization mechanism of the gas. The controversy upon the main ionization mechanism of the NLR has not settled yet: photoionization by a central source and ionization by shocks (photoionization in 'situ') are the possible ones. Wilson (1997) listed five parameters which, in his opinion, do not allow to distinguish between these two mechanisms: 1) the high electron temperature (up

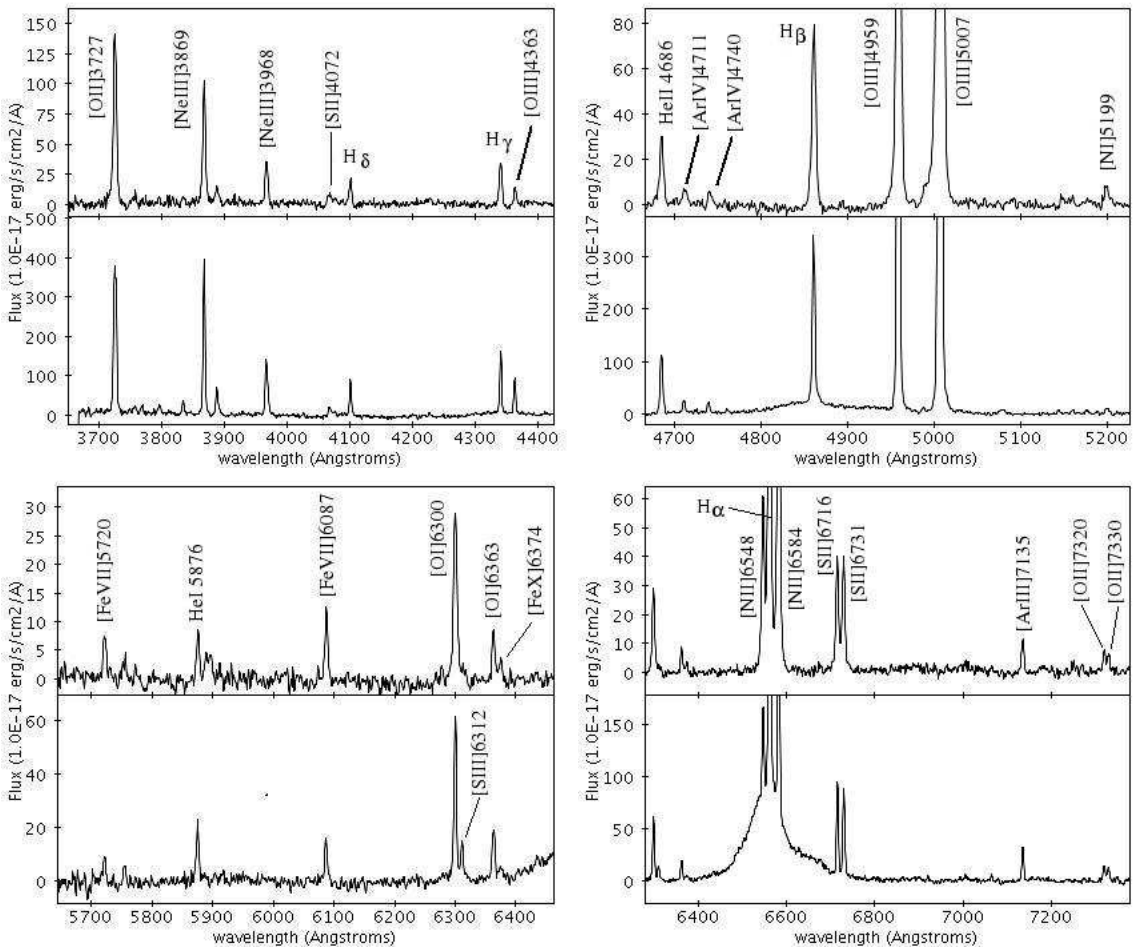

Figure 1.2: Two examples of SDSS spectra are shown in four different wavelength ranges: Seyfert 2 (*up*) and Intermediate-type Seyfert (*down*). In the figure are indicated the emission-lines. These spectra are correted by Galactic absorption, shifted to rest frame and stellar component subtracted (see chapter 3). The Intermediate-type Seyfert spectrum shows a clear broad and asymmetric H_α component and a weak H_β broad component.

to $\sim 18000K$) measured in some cases, 2) the strengths of high ionization lines, 3) the spatial variation of excitation within the NLR, 4) a correlation between excitation level and velocity dispersion and 5) the existence of 'energy deficits' in Seyfert 2 galaxies, that is the number of ionizing photons derived from the UV and optical continuum is not able to account for the observed recombination-line emission. This problem is solved once the torus obscuration is accepted. Recently, using XMM-Newton observations, Lamassa et al. (2009) showed that the torus obscuration is always present in their sample of Seyfert 2 galaxies. The NLR see directly the ionizing continuum whereas the observed continuum (UV and optical ranges) suffers a heavy obscuration.

Photoionization models using ionization bounded clouds (optically thick to the ionizing radiation) are able to reproduce most of the emission lines observed in the NLR and ENLR, with the exception of high ionization lines (such as $HeII4686$, $[FeVII]5879, 6087$, $[FeX]6374$ and $[FeXI]7892$, $[NeV]3426$, $CIV1549$, $CIII]1909$). This problem is avoided if two clouds, with different ionization levels, are taken into account: an ionization bounded cloud plus a matter bounded cloud (Binette et al., 1996). The first one accounts for the low ionization lines, the second one for the high ionization lines (with high temperature). It is also true that the high ionization UV lines can be interpreted in terms of emission from the cooling zone of a shock (Dopita & Sutherland, 1995). Anyway, with a matter bounded cloud (high ionization cloud) it is possible to justify the high temperature (high I_{4363}/I_{5007} ratio, hereafter $R[OIII]$) measured in many cases (items 1 and 2). On the contrary high density values must be required, $n_e > 10^5\, cm^{-3}$, which cannot be reasonable for spatially extended gas ($\geq 100\, pc$).

The spatial variation of excitation (item 3) could be explained using a two phase models, high and low density with low and high excitation respectively. The first one is the ionization bounded cloud and the second one the matter bounded cloud. If a thermal confinement is assumed (the pressure between the two clouds are the same) it is easy to show that in the same place different excitation clouds could be present. Following Netzer (2008), when two clouds with different temperatures (T_h and T_l, high and low temperatures respectively), densities and levels of ionization, are located in the same place, then the ionization parameters are

$$U_l = \frac{L}{c\, r^2\, (N_H)_l};\;\; U_h = \frac{L}{c\, r^2\, (N_H)_h} \tag{1.2}$$

At a given distance r, the radiation pressure is simply

$$P_{rad} \propto L/c\, r^2 \tag{1.3}$$

which is independent of the gas density. It means that

$$U \propto P_{rad}/N_H \Rightarrow U/T \propto P_{rad}/(T\, N_H) \tag{1.4}$$

$$P_{gas} \propto T\, N_H \Rightarrow U_l/T_l = U_h/T_h \propto P_{rad}/P_{gas} \tag{1.5}$$

Then, for all components at the same chosen location

$$U/T \propto 1/P_{gas} \propto 1/(T\, N_H) \tag{1.6}$$

If U/T are the same for both the components, temperatures and hence densities must be different.

Concerning the correlation between excitation level and velocity dispersion (item 4), it is clear that assuming the pressure equilibrium ($P \propto \rho\, V^2$), high density clouds (low ionization) have lower velocity and viceversa in the low density clouds.

Another important aspect of the NLR is the kinematics. There are three fundamental motions: a) turbulent motions, measured from the FWHM, b) bulk motions, connected to the jets and outflowing winds and c) gravitational motions (rotating disks, virialized motions). The gas velocity dispersion is scarcely correlated with the stellar velocity dispersion with the exclusion of low ionization lines, which are formed, presumably, in the outer region of the NLR. Then it is reasonable that at large distances from the nucleus the motion is governed by the gravitational field (Walsh et al., 2008). Single clouds in neaby Seyfert galaxies observed with HST, show a similar kinematic profile, in which the projected radial velocity gradually increases from the central point source out to $r \sim 100\,pc$, after that the velocities abruptly begin to decrease towards systemic (Kraemer et al., 2007). The gas is continuously accelerated, then begins to undergo a rapid deceleration. The dynamics of this process is still not clear (Das et al., 2007; Everett & Murray, 2007), but it is likely that radiation pressure from the continuum source gives an important contribution. Including turbulence and dissipative heating in the photoionization models it is possible to explain the strenght of the high ionization lines (i.e. $[HeII]1640$, $[NeV]3426$), otherwise these lines are often underestimated, moreover the turbulence increases the cloud stability (Kraemer et al., 2007).

$[OIII]5007$ line profiles indicate that gas outflows should be present in the vast majority of the NLR. There are three main mechanisms able to support a gas outflow: a) radiation pressure, b) radio source pressure and c) jet ram pressure. The second mechanism cannot explain the observed gas motions (Rosario et al., 2008). Even if the radiation pressure could be able to support an outflow in many cases, it seems that the most probable mechanism should be the ram pressure of the jet. In fact, connections between jets and ionized gas outflows have been well estabilished over the past decade (Rosario et al., 2008; Smirnova et al., 2007; Wilson, 1997, and references cited therein).

Recent observations in IR, with integral field spectroscopy at high spatial resolution, show the presence of a hydrogen molecular thick clumpy disk. *"The kinematics of the molecular gas reveals general rotation, although an additional significant component of random bulk motion is required by the high local velocity dispersion. The size scale of the typical gas disk is found to have a radius of* $\sim 30\,pc$ *with a comparable vertical height. Within this radius the average gas mass is estimated to be* $\sim 10^7\,M_\odot$ *based on a typical gas mass fraction of* 10%*, which suggests column densities of* $N_H \sim 5 \times 10^{23}\,cm^{-2}$*. Extinction of the stellar continuum within this same region suggests lower column densities of* $N_H \sim 2 \times 10^{22}\,cm^{-2}$*, indicating that the gas distribution on these scales is dominated by dense clumps." (Hicks et al., 2009).*

This picture is consistent with a recent model performed by Schartmann et al. (2009). This model shows a possible stellar feedback on the formation and evolution of the tori. The observations are consistent with a two-component model made up of a geometrically thin and warm central disk, surrounded by a colder, fluffy torus component (see Schartmann et al., 2009, and the references therein). The authors followed the evolution of the interstellar medium by taking discrete mass loss and energy ejection due to stellar processes, as well as optically thin radiative cooling into account. As the authors wrote: *"The interplay between injection of mass, supernova explosions and radiative cooling leads to a two-component structure made up of a cold geometrically thin, but optically thick and very turbulent disk residing in the vicinity of the angular momentum barrier, surrounded by a filamentary structure. The latter consists of cold long radial filaments flowing towards the disk and a hot tenuous medium in between, which shows both inwards and outwards directed motions."*

Ho (2009) showed that the mass budget of the NLR can be accounted by mass loss from evolved stars. From H_α (or H_β) luminosity it is possible to determine the ionized

gas mass (Osterbrock & Ferland, 2006). The author found $M_{NLR} \sim 3 \cdot 10^4\, M_\odot$ in a region of $200 \times 400\, pc$. Comparing this mass with the amount of material shed by evolved stars, and following the relation introduced by Padovani & Matteucci (1993), $\dot{M}_* \sim 0.05\, M_\odot\, yr^{-1}$, stellar mass loss can sustain the gas reservoir in the NLR if the stellar debris survives for periods longer than $\sim 2 \cdot 10^5 - 10^6\, yr$ before it dissipates and merges with the surrounding hot interstellar medium.

The mass loss from evolved stars gives account of the high metallicity found in the ionized gas of Seyfert galaxies (Storchi-Bergmann et al., 1998; Hamann et al., 2002) and only in rare cases the metallicity appears sub-solar (Groves et al., 2006; Izotov & Thuan, 2008).

Chapter 2

Samples selection and measurements

Traditionally, the classification of narrow emission line galaxies at optical wavelengths relies on a set of diagnostic diagrams based on emission-line ratios, such as $[OIII]5007/H_\beta$, $[NII]6584/H_\alpha$, $[SII]6716,6731/H_\alpha$, $[OI]6300/H_\alpha$ (Veilleux & Osterbrock (1987), hereafter VO or Baldwin et al. (1981), hereafter BPT). These diagrams are sensitive to the measurement of the H_β emission-line that is made difficult by the presence of the underlying stellar absorption. The lack of an adequate correction for this stellar component leads to an underestimate of the flux of the H_β emission-line and, consequently, to an over-estimate of the $[OIII]5007/H_\beta$ diagnostic ratio. As a direct effect, the diagnostic diagrams fail to correctly classify galaxies. This is true in particular for the AGN region of the diagrams. In order to show this effect we used the Garching DR4 database[1], where we found the original SDSS fluxes and those corrected by stellar component. In Figure 2.1 we show the classical diagnostic diagram $log([OIII]5007/H_\beta)$ vs $log([NII]6584/H_\alpha)$, built with both sets of fluxes, before (red) and after (blue) the correction for stellar absorption. After the correction both ratios decrease but in different measures, because the H_α emission-line is less sensitive to the stellar absorption. Therefore, the points in the diagram move down and slightly to the left. This means that using the original data the AGN region could be populated by HII galaxies but not viceversa. It is clear that the correction by stellar component is mandatory if we want a correct classification.

The investigation presented in this thesis aims at the analysis of the narrow line region (NLR) in a statistical sample of Seyfert galaxies. For building such a sample, we decided to exploit the Sloan Digital Sky Survey (SDSS) database. To perform the correction for stellar absorption we synthesized the composite stellar populations of the galaxies by using the code STARLIGHT (Cid Fernandes et al., 2005) and we subtracted them from the observed spectra. However, before undertaking this step, we had to tackle a problem concerning the selection of galaxies from SDSS database. In particular an automated selection of intermediate-type Seyfert galaxies (S1.5, S1.8, S1.9) is hampered by contamination with broad emission-lines. To overcome this problem we had to find out a suitable criterion for the identification of all type 2 and intermediate-type AGN from SDSS raw-data. This involved the use of a new diagnostic diagram, as explained in the next section.

[1] http://www.mpa-garching.mpg.de/SDSS/DR4/

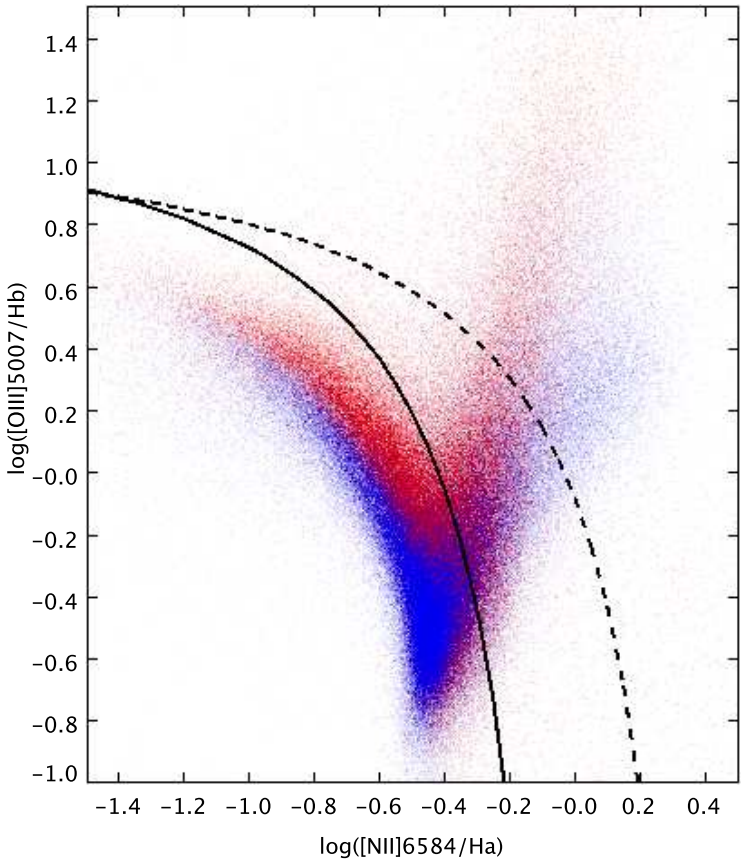

Figure 2.1: $log([NII]6584/H_\alpha)$ vs $log([OIII]5007/H_\beta)$ (SDSS-DR4), in blue the objects using the fluxes corrected by stellar component, in red, the same objects before the correction. In the diagram the solid and dashed lines separate star-forming galaxies (on the left of the solid line) from composite HII-AGN types (between solid and dashed lines) and AGN (on the right of the dashed line) (Kewley et al., 2006).

2.1 A new diagnostic diagram and spectra selection

In order to select the Seyfert 2 (hereafter S2) and the intermediate type Seyfert galaxies (hereafter I-t) from the SDSS using the data stored in the database, it was necessary to find a new diagnostic diagram which was able to include the emission line galaxies with broad components. We introduced a new diagram named Oxygen diagram (hereafter O_{123} diagram). This diagram is based on the $[OII]3727/[OIII]5007$ (hereafter O_{23}) and $[OI]6300/[OIII]5007$ (hereafter O_{13}) ratios. The first ratio gives a measure of the ionization level and is used in the new diagnostic diagram introduced by Kewley et al. (2006). The second ratio is very important because it is a tracer of the hardness of the ionizing spectrum at large radii from the source (Shields & Filippenko, 1990). The O_{13} ratio was employed for the first time in order to classify different regions of the galaxy IC 5135 by the previously mentioned authors (Shields & Filippenko, 1990, figure 13). Up to now this ratio has never been employed to classify a large number of objects. The great advantages of the O_{123} diagram are the following: i) the Oxygen lines are visible in all AGN spectra (with good S/N ratio), ii) Oxygen is the only element for which it is possible to see three different states of ionization in the visible range, iii) the employed ratios are sensitive to the ionization parameter and power-law index and are weakly dependent on the metallicity and density, iv) finally they are not contaminated by stellar spectral features, therefore we need not to subtract the stellar template from the original spectra before classifying the objects. Nevertheless this diagram has two main disadvantages: the ratios are not reddening free and the $[OI]6300$ is sometimes weak and difficult to be measured especially in $S/N_{[OI]6300} \leq 10$. From the SDSS DR7[2] (Abazajian et al., 2009) we extracted all galaxies with $[OII]3727$, $[OIII]5007$, $[OI]6300$ emission lines with the constrain $S/N_{[OI]6300} > 3$ obtaining 119000 (Figure 2.2).

For checking the effectiveness of Oxygen spectral lines in isolating Seyfert galaxies, we carried out a test. First we exploited the database of 85224 galaxies published by Kewley et al. (2006), which we cross-correlated with our sample obtaining more than 60000 sources. Then we plotted the VO diagnostic diagrams and we used the relations given in Kewley et al. (2006) to classify these objects as Seyfert, LINERs, star forming and composite Seyfert-H II galaxies. Since the Kewley et al. (2006) data are reddening corrected and the host galaxy spectrum is removed, they are not directly comparable with our sample. Therefore, we decided to extract from SDSS the spectroscopic information about the classified objects and we plotted the O_{123} diagram. The result was extremely encouraging: this plot (Figure 2.3) shows a V-shape where the upper side is populated by star forming galaxies, while the lower side is populated by Seyfert galaxies, LINERs and composite objects, but Seyfert and LINERs are sufficiently separated. This diagram is not new, since it was already used by Shields & Filippenko (1990) (see their figure 13), but the indicated areas where Seyfert galaxies, LINERs and H II regions are expected to be found, do not perfectly correspond to our data.

By applying the O_{123} diagram to our selected 119000 emission line galaxies we derived the empirical separation line to isolate Seyfert galaxies by splitting the $log(O_{23})$ in bins of 0.1 dex, in the range $[-1.2, 0.3]$, and plotting histograms of $log(O_{13})$ in bins of 0.1 dex. Then we estimated the value of the minimum between the two peaks of the distributions (Figure 2.4) and finally taking into account the mean point of the bin we interpolated these data with a polynomial function obtaining as result the following formula:

$$log(O_{23}) = 0.20 - 0.25 \cdot log(O_{13}) - 0.39 \cdot log(O_{13})^2 \tag{2.1}$$

[2] http://www.sdss.org/dr7/

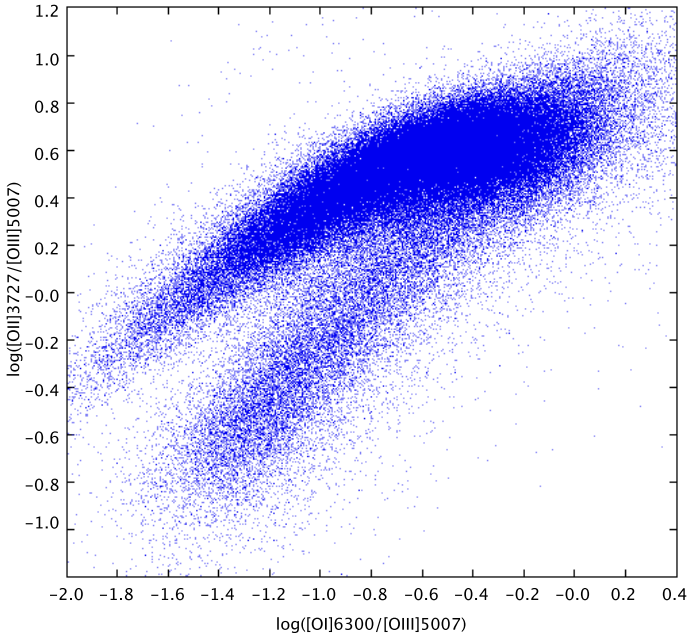

Figure 2.2: O_{123} diagram. 119000 galaxies are selected with the constrain $S/N_{[OI]6300} > 3$ (SDSS-DR7)

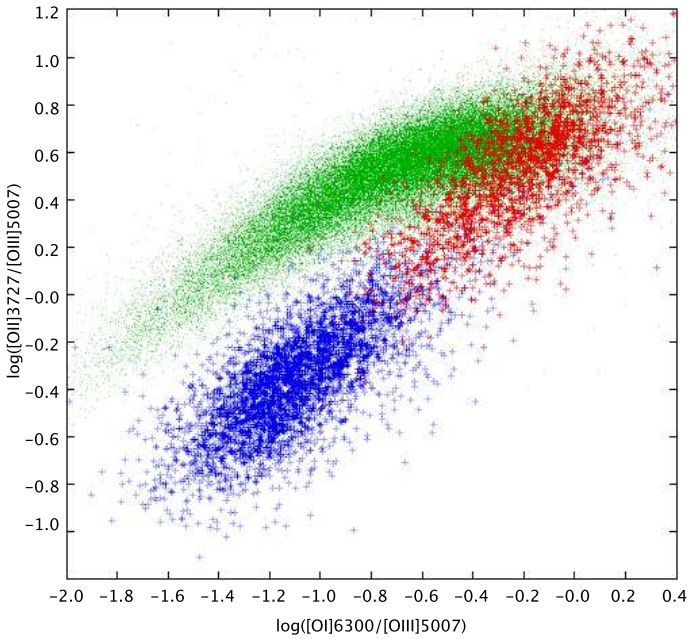

Figure 2.3: Kewley classification (Kewley et al., 2006) on O_{123} diagram: S2 (*blue plus*), LINERS (*red plus*) and star-forming galaxies (*green dots*).

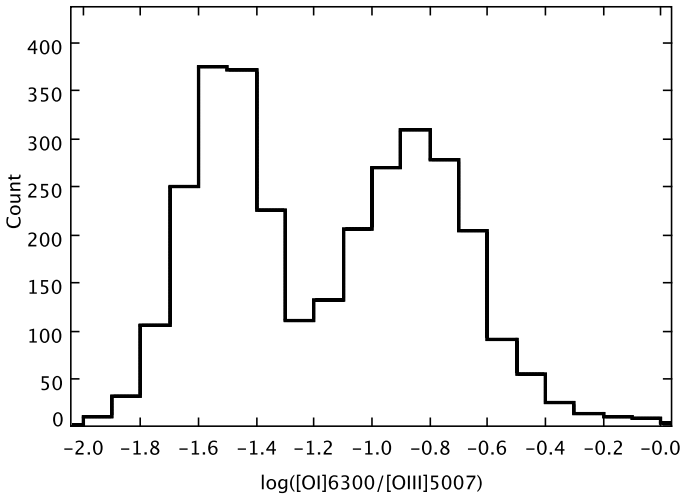

Figure 2.4: Distribution of $log(O_{13})$ with the $-0.1 \leq log(O_{23}) \leq 0$.

By selecting the objects under the curve we include 97% of the original sample of Seyfert galaxies. Of course this new sub-sample is contaminated by the other objects: in particular, it contains 60% Seyfert galaxies and 31% composite Seyfert-H II, but only 4% LINERS and 5% star-forming galaxies. So, we can conclude that about 10% of a sample selected by following this method consists of non-Seyfert galaxies. Finally we compared our sample with Garching SDSS DR4 data using the fluxes corrected by stellar template and reddening and we verified that our sample, after the correction by stellar component and reddening, is perfectly overlapped to the lower sequence. The upper sequence is the star-burst area as we verified using the VO diagrams. So we have now another diagnostic diagram which is able to distinguish between AGN and star-burst galaxies. It is interesting to stress that the lower sequence contains both narrow and broad AGN. This is due to the fact that it uses only the Oxygen lines. In conclusion the O_{123} diagram is useful for the classification of emission line galaxies in general and not only for narrow emission-line ones. Even if the lines are not corrected for reddening, this diagram is still valid because the distribution of the objects is only translated and it is really very unlikely that an object changes sequence.

By applying the previously mentioned conditions to the whole sample we found that about 16000 objects populate the AGN region on the O_{123} diagram.

Since the SDSS spectra are obtained with a 3 arcsec fibre aperture, a redshift threshold $z \leq 0.1$ is adopted to reduce the flux contamination by extranuclear sources (Kewley et al., 2006). However, in the AGN region of the O_{123} diagram we do not detect any variation in the point distribution in the redshift bins up to $z \leq 0.1$. The lower limit $z \geq 0.02$ is mandatory because the $[OII]3727$ line must be visible in the spectrum, where $[3800 - 9200]$ Å is the wavelength range covered by the SDSS spectra.

The total number of galaxies in the AGN region that satisfy the mentioned conditions is 5678 (Figure 2.5). This sample will be contaminated by LINERS, star-burst galaxies and composite galaxies and only after the subtraction of the stellar template will be possible to classify them correctly.

With the adopted redshift range the projected aperture corresponds to $1.2 - 5.2\,kpc$. It means that the analyzed area contains the NLRs and the inner part of the ENLRs if present.

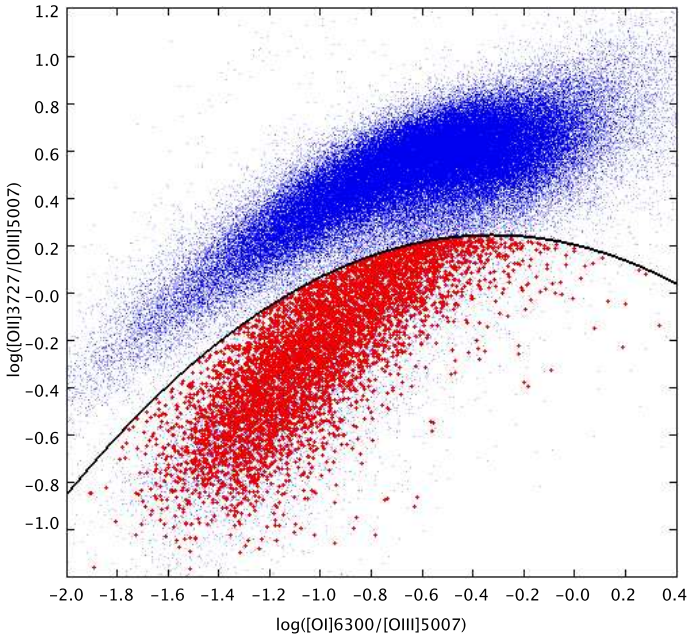

Figure 2.5: The sample (*red plus*), 5678 galaxies. The line indicates the separation between star-forming galaxies and AGN as explained in the text.

All the structures mentioned in Chapter 1 are inside this area with the exception of the nearest galaxies.

Figure 2.6 shows clearly that the S/N ratio of the spectra measured at rest-frame 5500 Å is in most cases between 10 and 40, with a peak around 20, so it means that the vast majority of the spectra are of acceptable quality.

2.2 Preparation of the spectra

The next step consisted of fitting and subtracting the underlying stellar continuum from each spectrum. This was done with the spectral synthesis code STARLIGHT (Cid Fernandes et al., 2005). This code makes a linear combination of synthetic spectra which are reddened and then convolved with a broadening function which allows to obtain the stellar velocity dispersion. Before being ready for use with this code, the spectra required some pre-processing that we did with IRAF packages. In particular, a correction for Galactic absorption was first applied by using DEREDDEN and A_V extinction values given by NED [3], then the spectra were shifted to rest-frame with NEWREDSHIFT by using z values given by SDSS, re-gridded to a dispersion of 1 Å/px with DISPCOR, converted into text format, and finally given as input to STARLIGHT. We used as base 92 synthetic spectra from Bruzual & Charlot (2003) by combining 23 ages (from $10^6\,yr$ up to $13{\cdot}\,10^9\,yr$) with 4 metallicities ($Z = 0.004, 0.008, 0.02$ and $0.05 Z_\odot$), and Cardelli et al. (1989) (hereafter CCM) as extinction function. We masked the emission lines in order to improve the quality of the fit.

The goodness of the STARLIGHT fit evaluated with χ^2 is peaked around 1 (Figure 2.7).

[3] NASA/IPAC Extragalactic Database http://nedwww.ipac.caltech.edu/

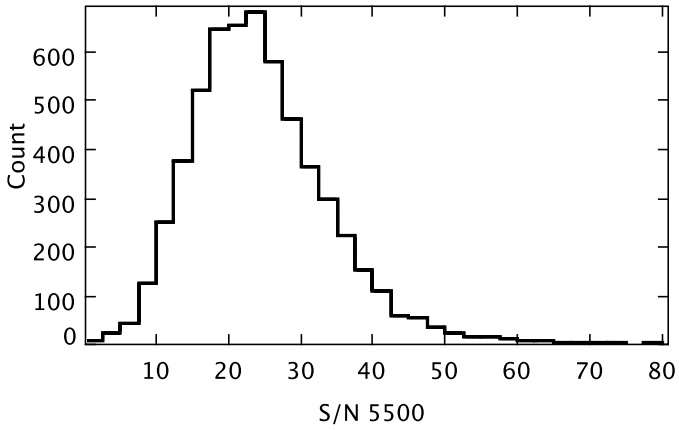

Figure 2.6: S/N ratio of the continuumat rest frame $5500\mathring{A}$ for the 5678 spectra of our sample.

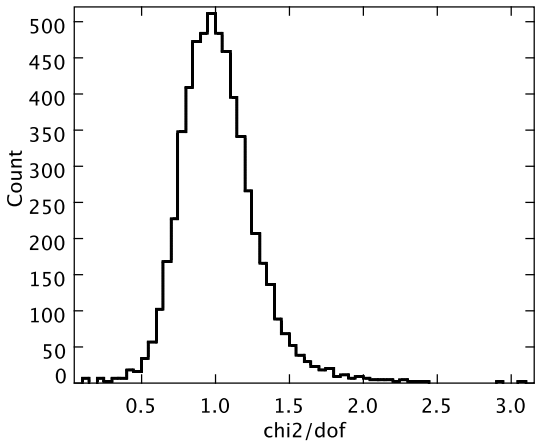

Figure 2.7: χ^2/dof distribution of STARLIGHT fits to the 5678 spectra.

The best-fitting synthetic spectrum of the continuum for each galaxy was subtracted from the observed one in order to obtain a pure emission line spectrum, where hydrogen and helium Balmer lines could be correctly measured (Figures 2.8 and 2.9).

2.3 The code GGFIT

The emission lines were fitted by means of a dedicated code written in C language. This code, named GGFIT, was developed in order to fit in automated way the emission lines of a group of spectra with a Multi-Gussian Non-linear Least Squares Fitting method[4]. The spectra are subdivided into lines and features, when more lines are very close to each other in wavelength such as $[NII]6548, 6584$ and H_α or $[SII]6716, 6731$ they must be treated together. The code

[4]Weisstein, Eric W. "Nonlinear Least Squares Fitting." From MathWorld–A Wolfram Web Resource. http://mathworld.wolfram.com/NonlinearLeastSquaresFitting.html

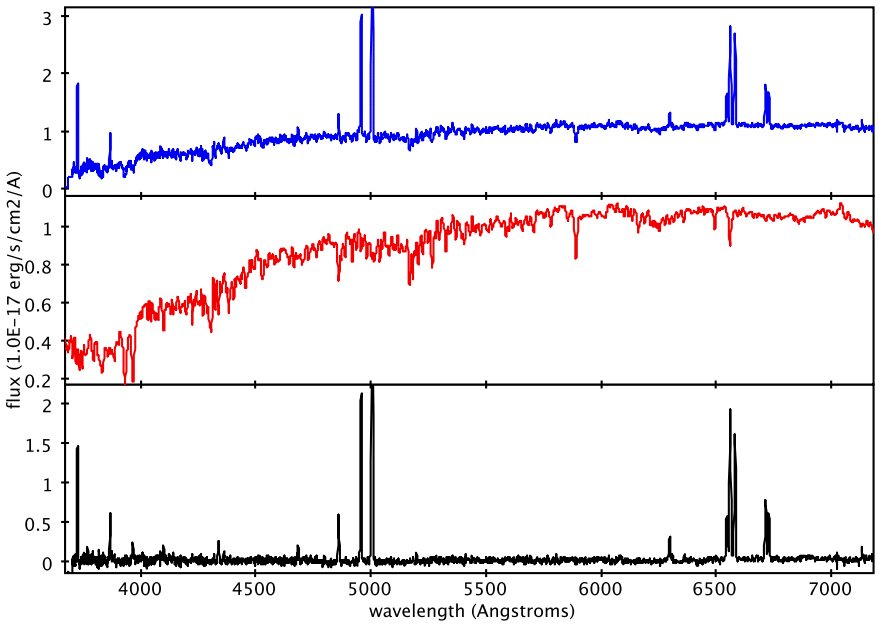

Figure 2.8: An example of correction for stellar component. The original spectrum (*blue*), the fit to the stellar component (*red*) and the residual pure emission-line spectrum (*black*).

returns a general table for all the measured spectra, each record summarizes 12 parameters for each line: the Gaussian parameters with errors, the central wavelength (x_0), amplitude (A) and sigma (σ) of the line, the measured flux (the integral of the feature, F_M), S/N, the R2 parameter (defined as $R^2 = dx_0 \cdot dx_0 + dA \cdot dA + d\sigma \cdot d\sigma$, this gives the goodness of the convergence, it must be ~ 0), Gaussian flux (F_G) and its error and the χ^2 of the fitting. The Gaussian flux (F_G) is derived from the following formula

$$F_G(\lambda) = \sqrt{2\pi}\,\sigma\,A_\lambda \qquad erg\,cm^{-2}\,s^{-1} \tag{2.2}$$

For each spectrum the code returns also a file with the original spectrum, the synthetic spectrum (the fitting) and the residuals.

The code needs two tables, the first one contains all the emission-line wavelengths to be measured and the number of Gaussians which could be used in the emission-line fit (Table 2.1), the second one the wavelength ranges occupied by features and isolated lines, within which the code must identify the peaks of the emission-lines and the boundaries of the emission-lines/features, and two continuum ranges, one at each side of a line or feature (Table 2.2).

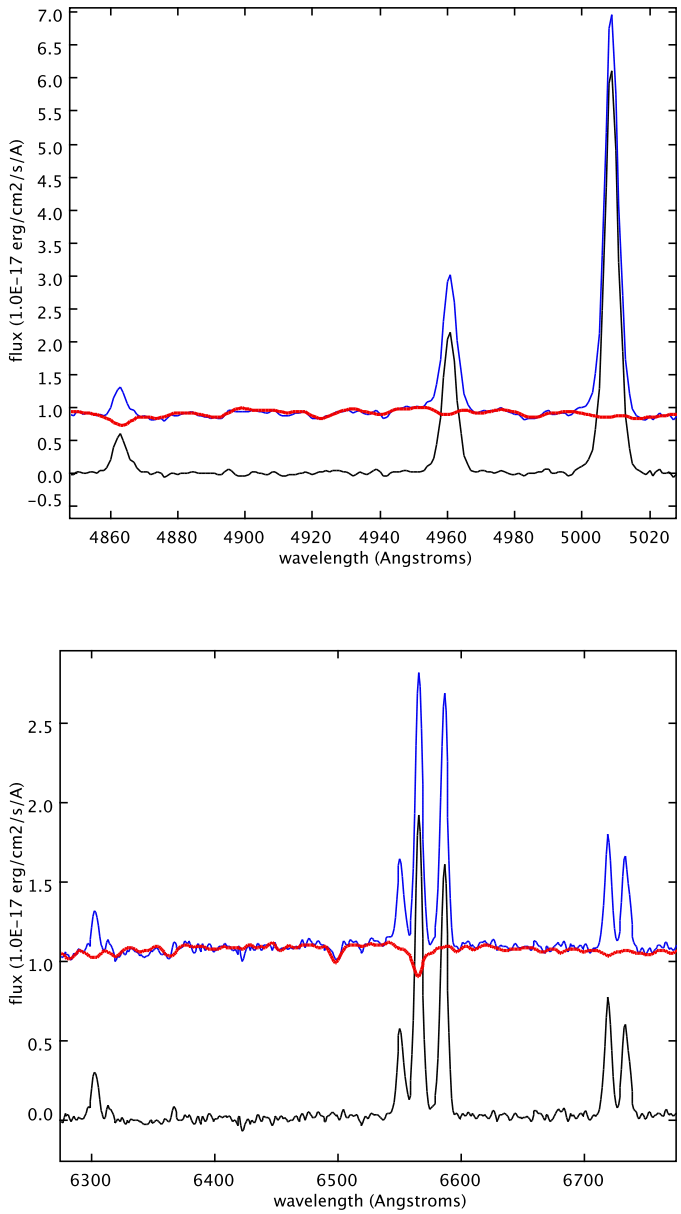

Figure 2.9: A more detailed comparison between the observed spectrum and the synthetic one. Colors are like in Figure 2.8. $H_\beta + [OIII]4959, 5007$ (*top*), $H_\alpha + [NII]6548, 6584$ and $[SII]6716, 6731$ (*bottom*).

Table 2.1: Measured lines

wavelength	components	line	IP low eV	IP high eV	$log(n_c\, cm^{-3})$
3727.4	1	[OII] 3727	13.62	35.12	3.7
3868.8	1	[NeIII] 3869	40.96	63.45	7.0
3967.5	1	[NeIII] 3967	40.96	63.45	7.0
4070.0	1	[S II] 4070	10.36	23.34	6.4
4101.7	1	H_δ 4102	13.60	–	–
4340.5	1	H_γ 4340	13.60	–	–
4363.2	1	[O III] 4363	35.12	54.94	7.5
4685.7	1	He II 4686	24.59	54.42	–
4711.3	1	[Ar IV] 4711	40.74	59.81	4.4
4740.2	1	[Ar IV] 4740	40.74	59.81	5.6
4861.3	2	H_β 4861	13.60	–	–
4958.9	2	[O III] 4959	35.12	54.94	5.8
5006.7	2	[O III] 5007	35.12	54.94	5.8
5199.1	1	[N I] 5199	0	14.53	3.3
5720.9	1	[Fe VII] 5720	99.1	124.98	7.6
5875.6	1	He I 5876	0	24.59	–
6087.0	1	[Fe VII] 6087	99.1	124.98	7.6
6300.3	1	[O I] 6300	0	13.62	6.3
6363.8	1	[O I] 6300	0	13.62	6.3
6548.1	1	[N II] 6548	14.53	29.60	4.9
6562.8	2	H_α 6563	13.60	–	–
6583.4	1	[N II] 6583	14.53	29.60	4.9
6716.5	1	[S II] 6716	10.36	23.34	3.2
6730.8	1	[S II] 6731	10.36	23.34	3.6
7135.8	1	[Ar III] 7136	27.63	40.74	6.7
7320.0	1	[O II] 7320	13.62	35.12	6.8
7330.0	1	[O II] 7330	13.62	35.12	6.8

Notes. The left hand side table shows the line wavelengths and the number of components used in the fit, this part is used by GGFIT. On the right, the table shows the measured lines with the ionization potential, low and high values, and the logarithm of the critical density.

Table 2.2: Spectral features and ranges

feature wavelength	peak range		feature range min		feature range max		blue range cont		red range cont		wavelength peak		
3727.4	3725	3730	3718	3736	3710	3744	3680	3710	3760	3840	3727.4	3727.4	3727.4
3868.8	3866	3871	3860	3875	3855	3885	3760	3840	4000	4050	3868.8	3868.8	3868.8
3967.5	3965	3970	3962	3973	3950	3990	3760	3840	4000	4050	3967.5	3967.5	3967.5
4070.0	4067	4073	4062	4079	4058	4082	4000	4050	4150	4250	4070.0	4070.0	4070.0
4101.7	4098	4105	4095	4108	4090	4113	4000	4050	4150	4250	4101.7	4101.7	4101.4
4340.5	4337	4344	4332	4348	4320	4352	4150	4250	4400	4500	4340.5	4340.5	4340.5
4363.2	4360	4366	4355	4371	4351	4375	4150	4250	4400	4500	4363.2	4363.2	4363.2
4685.7	4683	4689	4679	4693	4650	4720	4550	4650	4730	4775	4685.7	4685.7	4685.7
4711.3	4709	4712	4705	4716	4702	4719	4550	4650	4750	4820	4711.3	4711.3	4711.3
4740.2	4738	4742	4734	4746	4731	4749	4550	4650	4750	4820	4740.2	4740.2	4740.2
4861.3	4859	4863	4854	4868	4760	4940	4550	4650	5050	5150	4861.3	4861.3	4861.3
4958.9	4956	4962	4947	4970	4929	4985	4750	4820	5050	5150	4958.9	4958.9	4958.9
5006.7	5004	5010	4990	5024	4978	5042	4750	4820	5050	5150	5006.7	5006.7	5006.7
5199.1	5197	5201	5193	5205	5180	5215	5050	5150	5230	5300	5199.1	5199.1	5199.1
5720.9	5719	5723	5710	5734	5685	5755	5600	5684	5941	6000	5720.9	5720.9	5720.9
5875.6	5870	5880	5860	5885	5820	5940	5600	5684	5941	6000	5875.6	5875.6	5875.6
6087.0	6085	6089	6081	6093	6050	6120	5941	6000	6150	6250	6087.0	6087.0	6087.0
6300.3	6298	6302	6293	6307	6275	6320	6150	6250	6390	6410	6300.3	6300.3	6300.3
6363.8	6362	6365	6359	6370	6340	6380	6150	6250	6390	6410	6363.8	6363.8	6363.8
6563.0	6558	6568	6540	6594	6400	6705	6150	6250	6800	6900	6548.1	6562.8	6583.4
6720.0	6715	6733	6706	6738	6695	6770	6670	6695	6800	6900	6716.5	6730.8	6730.8
7135.8	7134	7138	7125	7147	7120	7152	6900	7100	7160	7250	7135.8	7135.8	7135.8
7325.0	7321	7329	7310	7340	7305	7345	7160	7250	7400	7600	7320.0	7330.0	7330.0

Notes. feature wavelength: the number indicates the approximate wavelength of the feature or isolated line.

peak range: wavelength range where the peak of the feature/line is found.

feature range min/max: minimum/maximum wavelength range occupied by the feature/line.

blue/red range cont: wavelength range where the continuum level is evaluated (blue/red side of the feature/line).

wavelength peak: in a feature there are at maximum three lines (excluding the broad or asymmetric components of the same line), if the numbers in these columns are different the code is treating a feature with three lines (i.e. $[NII]6548 + H_\alpha + [NII]6584$), if two numbers are equal there are two lines (i.e. $[SII]6716, 6731$), otherwise the line is isolated.

The continuum is evaluated with a linear interpolation because the spectra are corrected for stellar component and the mean baseline is about zero. The code measures the peak coordinates and the FWHM, with a simple linear interpolation, after the continuum subtraction. The algorithm uses these estimates as first guesses for the non-linear least squares fitting procedure and determines the final parameter values. In $H_\alpha + [NII]6548, 6584$ and $[SII]6717, 6731$ features the lines could be heavily blended and the first guess of the FWHM of each line could not be determined. In this case the $[OIII]5007$ FWHM is assumed. The algorithm begins respectively with three Gaussians in $H_\alpha + [NII]6548, 6584$ feature, two in $[SII]6717, 6731$ and $[OII]7320, 7330$ and a single Gaussian in the other cases (Table 2.1).

For $[OIII]4959, 5007$, H_β and H_α lines, when the convergence is reached a χ^2 test is performed. If the convergence is not reached or χ^2 is not acceptable, with a level of significance of 1%, a new Gaussian is added. The code makes three different attempts with two Gaussians and with different input parameters, then if the convergence is achieved the best fitting (the best χ^2) is adopted. In some cases the best fit has two Gaussians but one of them cannot be physically meaningful (having an excessively low flux and/or being is either extremely narrow or extremely broad). In this case a single Gaussian fitting is adopted. The spectra where the diagnostic lines could not be fitted were excluded from the analysis. The lines are the following: $[OII]3727$, H_β, $[OIII]5007$, $[OI]6300$, H_α, $[NII]6584$, $[SII]6717$, $[SII]6731$.

The main problem is determining in an automated way the line boudaries, i. e. the wavelengths at which the line profile fades into the continuum noise on the blue and on the red side of the line. For this purpouse, the algorithm evaluates the intensity value of each pixel from the line peak towards bluer wavelengths until it reaches a minimum. If this minimum is lower than the value of the continuum plus its *rms* (hereafter σ_c), the associated wavelength is retained as the blue boundary of the line. If not, the algorithm searches for a new minimum. The same procedure is executed on the red side of the line. A maximum value for the full width at zero intensity (FWZI) of the line has been imposed to prevent non-convergence. If this value is reached, the algorithm starts again the procedure by comparing the intensity at each pixel with the value of the continuum plus 2 or 3 times σ_c.

The flux error is evaluated by propagating Equation 2.2. This requires an estimate of the errors in the parameters A and σ_c. As an estimate of the error in the amplitude we adopt the value σ_c determined in proximity of the emission-line. Estimating the error of σ is more complicated. For this purpose we chose to apply a Monte Carlo method during the fitting procedure.

After obtaining the Gaussian parameters the code generates 3000 possible models near the best fit solution (inside the fixed intervals: $-\sigma_c < A < \sigma_c$ counts, $-1 < \sigma < 1$ Å, $-1 < x_0 < 1$ Å) changing randomly the parameter values. A χ^2 test is performed and only the models with a significance level above 70% are considered. This procedure was applied only to the features with one or two lines (the H_α features, for example, requires too long a computational time). The accepted models give us the range of variability of the parameters. The amplitude error results always lower than σ_c, whereas the other two parameters depend on the S/N in the same way. In Figure 2.10 the case of H_β is presented. As it can be seen, the relation between $log(\sigma)$ and $log(S/N)$ can be represented by a linear fit to the points. This is true for all the measured lines and the linear fits are similar. Therefore the σ error model of H_β was applied to each line. Hence, once the S/N is measured the σ error ($\Delta\sigma$) is given by

$$log(\Delta\sigma) = -1.2 \cdot log(S/N) + 0.7 \tag{2.3}$$

The same technique was employed from Corsini et al. (1999) (their figure 1) in order to

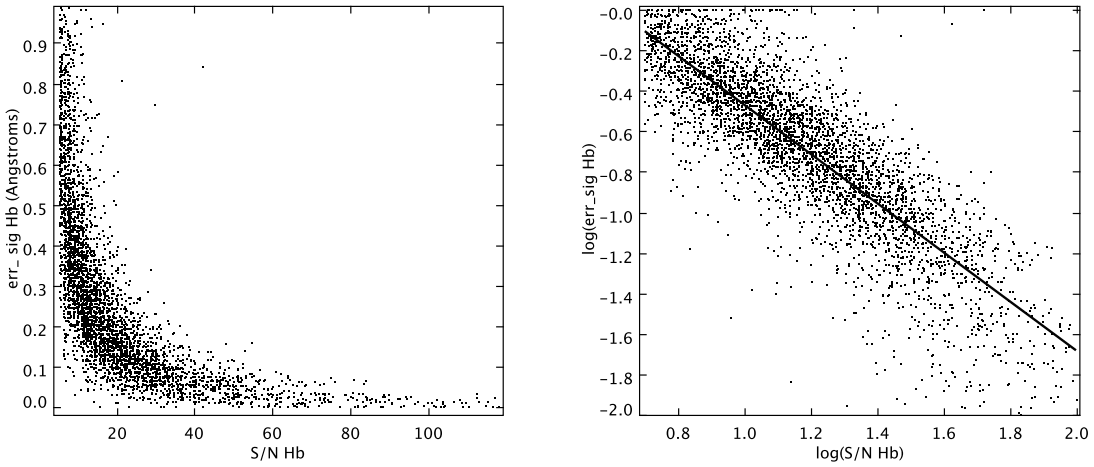

Figure 2.10: *left*: $\Delta\sigma_{H\beta}$ distribution vs the $S/N_{H\beta}$ for measured 5678 spectra, *right*: the same plot in logarithmic values and the fit adopted to derive $\Delta\sigma$ (Equation 2.3).

evaluate the velocity errors from Gaussian fitting.

The line wavelength error, Δx_0, correlates very well with $\Delta\sigma$ and S/N (Figure 2.11). The typical error on the wavelength is about 0.5 Å when the S/N is around 10.

In order to check the reliability of the automatic fitting procedure, about 1300 spectra were measured by hand (tha spectral analysis of this sample is in Rafanelli et al. (2008)). The line boundaries limits and the fluxes obtained are the same with very rare exceptions. The number of failures increases when the $S/N < 5$. From this analysis we selected the measurable emission-lines (Table 2.1). No other line was taken into consideration because too weak or not reliable, as $H\epsilon$ and successive Balmer lines. In any case only the lines with a $S/N > 5$ were measured.

Our software was able to fit successfully 4254 spectra: the others were rejected because either the most important emission-lines (i.e. those used in diagnostic diagrams) had $S/N < 5$ or (in a few cases) their fit did not converge.

In Figure 2.12 we compare the distributions of the $[OIII]5007/H\beta$ ratio as obtained with the original SDSS data (red, dashed line) and after the correction for stellar component (blue, solid line). It appears clearly that this correction is absolutely mandatory if we want to correctly classify the spectra.

2.4 Spectral classification through $FWHM_{H_\alpha}$

The classification of Seyfert galaxies is based on the visibility of the Balmer line broad components (Osterbrock & Ferland, 2006) but this criterion is a bit subjective and depends on the spectra quality. Additionally, visually classifying a large number of spectra is very difficult and extremely time-consuming. In this work the criterion adopted for the spectral classification is based on the presence of a second component in the H_α emission-line and on its FWHM. Out of the 4254 measured spectra, 1938 show a secondary H_α component. In Figure 2.13 we present the $FWHM_{H_\alpha}$ distribution of both components (when present) after correction for instrumental width. The $FWHM_{H_\alpha}$ distribution of the second component shows two peaks, between 500 and 1000 km/s and between 1500 and 2200 km/s respectively.

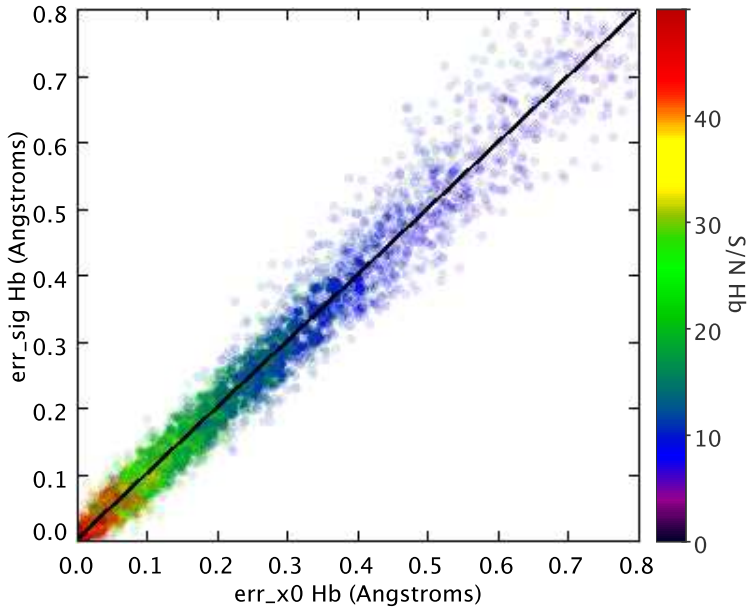

Figure 2.11: $\Delta\sigma_{H\beta}$ vs Δx_0 vs S/N_{H_β}, the correlation coefficient of the interpolation is 0.95.

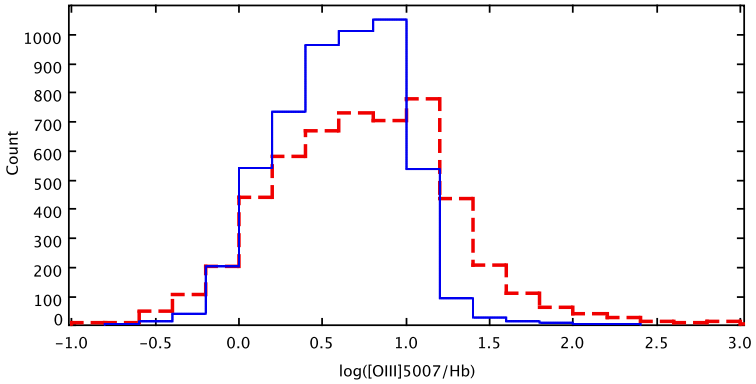

Figure 2.12: Comparison between the distributions of log([OIII]5007/H_β) obtained with raw fluxes (*red dashed line*) and with fluxes corrected for the stellar component (*blue solid line*).

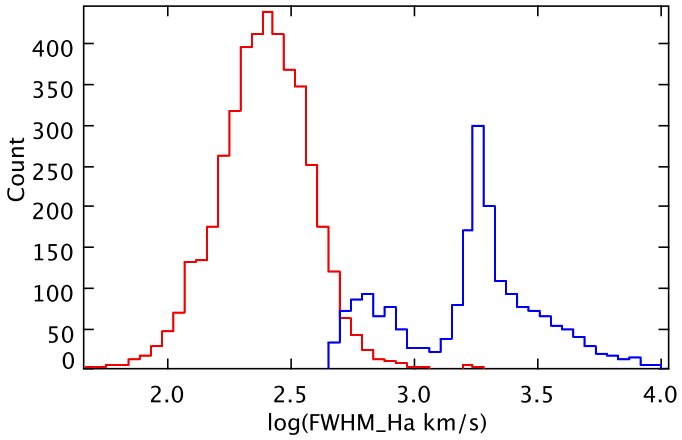

Figure 2.13: Distribution of $FWHM_{(H_\alpha)}$ for the first component (*red*) and second component (*blue*) of the emission-line.

The first one is related to the asymmetries of the H_α profile, the second one resembles more to a spurious spike rather than a reliable distribution. In fact if the $FWHM_{H_\alpha}$ of the second component is lower than 2000 km/s the line is hidden in the $H_\alpha + [NII]6548, 6584$ and H_α feature. The SDSS spectral resolution is too low and it is very difficult to disentangle the true components. The second component may be a true broad H_α but also it may be a mere mathematical result of the fit too. In fact the median wavelength peak distribution of these spectra is 6568 Å, systematically displaced toward the $[NII]6584$ (Figure 2.14). Another explanation could be the use of different line profiles, for example if the Voigt profile with extended wings is assumed it could more easily to reproduce the observed profile of the $H_\alpha + [NII]$ feature.

Since H_α and H_β are emitted by the same gas component(s), they are expected to have the same FWHM. To verify that this is the case, we compared the widths of both the narrow and broad H_α and H_β components for all 4254 measured spectra. The corresponding plot, in logarithmic scale, is shown in Figure 2.15. We notice that for $FWHM_{H_\alpha} < 2000$ km/s (3.3 in logarithm) the expected correlation between the widths of the two emission-lines (second components, blue crosses in the figure) is not found any more. In some cases the widths of the lines totally differ from each other. We interpret this behaviour as an indication that either the detected second component of H_β is not the broad one, or the broad H_β component is undetectable or poorly fitted. Moreover when $FWHM_{H_\alpha} < 1250$ km/s (3.1 in logarithm) the H_β second component disappears with the exclusion of few objects.

All the spectra with narrow H_α or with a second component narrower than 1250 km/s were classified as narrow-line spectra. The errors where taken into account, and the condition was fixed to $FWHM_{H_\alpha} - 3 \cdot \Delta FWHM_{H_\alpha} < 1250\, km/s$. The H_α flux was obtained as the sum of two fluxes when a second component was present. The H_β broad component could be detected when a broad H_α component does exist, not viceversa. The spectra which show a second H_α component with $FWHM_{H_\alpha}$ greater then 2000 km/s are classified broad-line spectra ($FWHM_{H_\alpha} + 3 \cdot \Delta FWHM_{H_\alpha} > 2000\, km/s$). In this second class a further constraint was imposed to insure the reliability of the broad component detection. The broad component was confirmed only if its height above the continuum at 6531 and 6595 Å was greater then $2\sigma_c$. The factor 2 was adopted based on visual tests on the visibility of

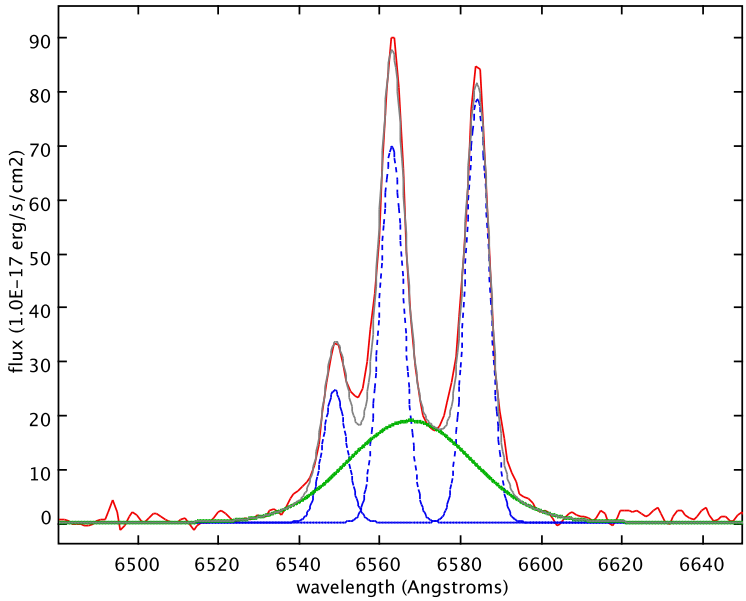

Figure 2.14: An example of the spectrum with a secondary component (*in green*) that is completely hidden within the $H_\alpha + [NII]$ feature. The resolution does not permit to recognize whether it is a true broad component. The figure shows the original feature profile (*red*), the narrow components (*blue dashed line*) and the resulting fit (*grey*).

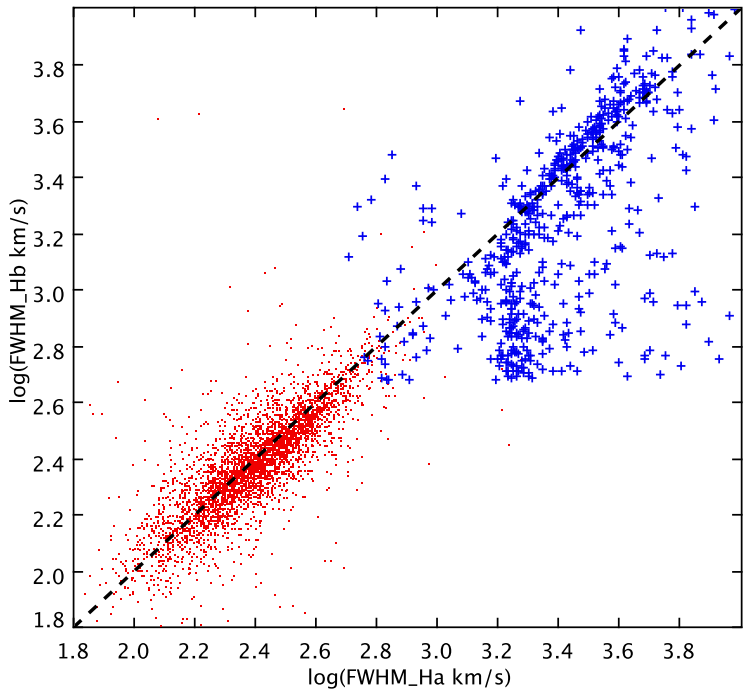

Figure 2.15: $FWHM_{H_\beta}$ vs $FWHM_{H_\alpha}$ for 4254 spectra. *Red dots* are the narrow component, *blue dots* the secondary component.

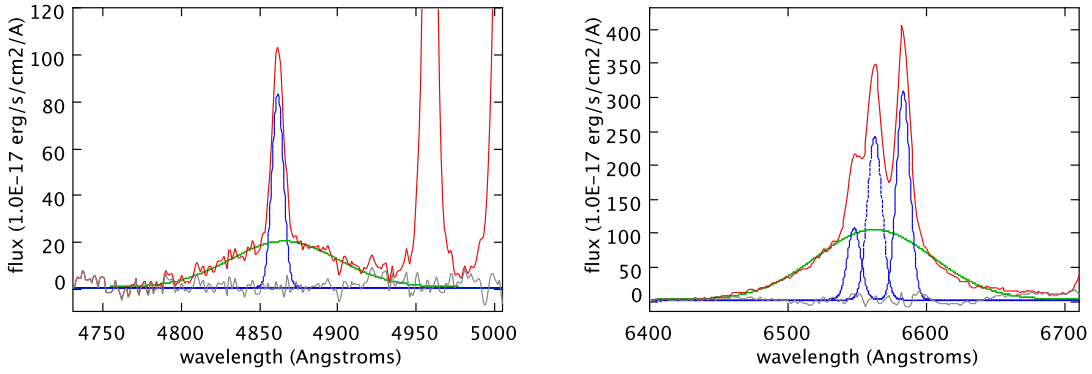

Figure 2.16: Example of H_β (left hand panel) and H_α (right hand panel) with a broad secondary component (*green line*). The observed spectrum is in *red*, the narrow components in *blue* and the residuals in *grey*.

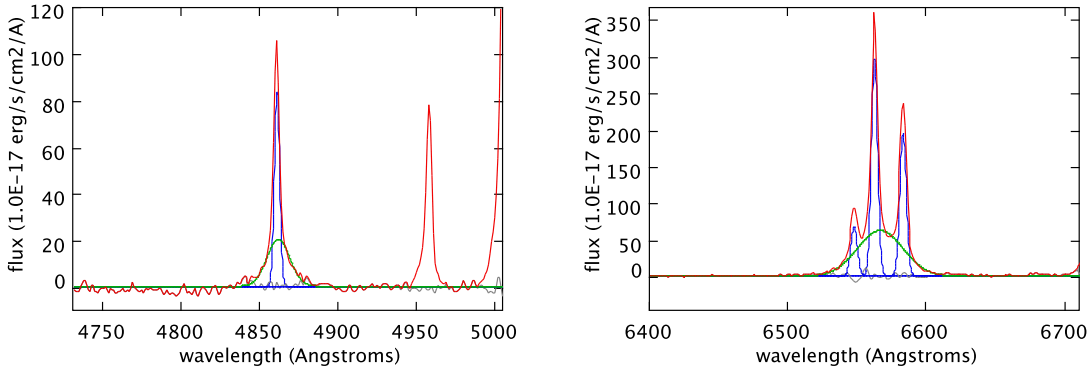

Figure 2.17: As in Figure 2.16, but for a case of relatively narrow secondary component.

the broad component. In Figures 2.16 and 2.17 there are two examples of broad-line spectra which satisfy the previously mentioned conditions.

The third group are the remaining spectra, with $1250 < FWHM_{H_\alpha} < 2000\,km/s$. The distributions of the second component $FWHM_{H_\alpha}$ of these groups are showed in Figure 2.18.

At the end, 598 objects were classified as broad-line AGN, 2836 as narrow-line AGN and 820 showed a second component (broad?) that could not be reliably confirmed. These spectra were re-fitted with the constrain of a single Gaussian in the H_α and H_β lines.

As a check we calculated the differences between the total measured flux of the H_α feature and the sum of the Gaussian fluxes used in the fit ($H_\alpha + [NII]6548, 6584$). The mean differences in percentage are 2.3%, 3.7% and 4.5% for the narrow-line, the broad-line and the third group of 820 spectra respectively (Figure 2.19). 90% of the spectra has a difference lower than 4% in the narrow-line spectra and lower than 8% in the other groups. Anyway these differences are acceptable and within the flux errors.

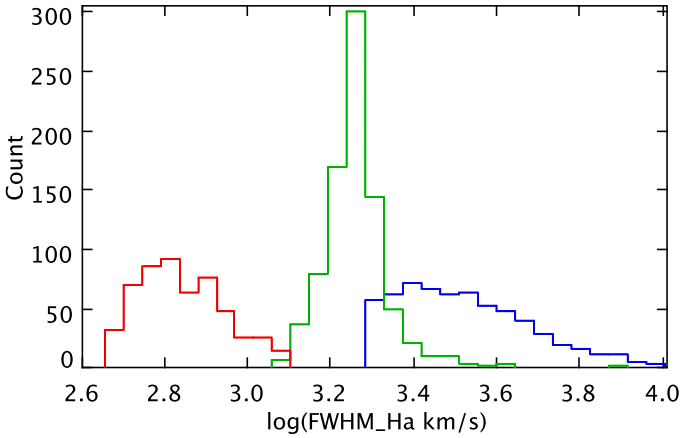

Figure 2.18: $FWHM_{H_\alpha}$ distribution for the second component, in *red* all the spectra which show a H_α second component with $FWHM < 1250\,km/s$, in *blue* the selected broad-line spectra, $FWHM > 2000\,km/s$, and in *green* the spectra with $1250 < FWHM < 2000\,km/s$.

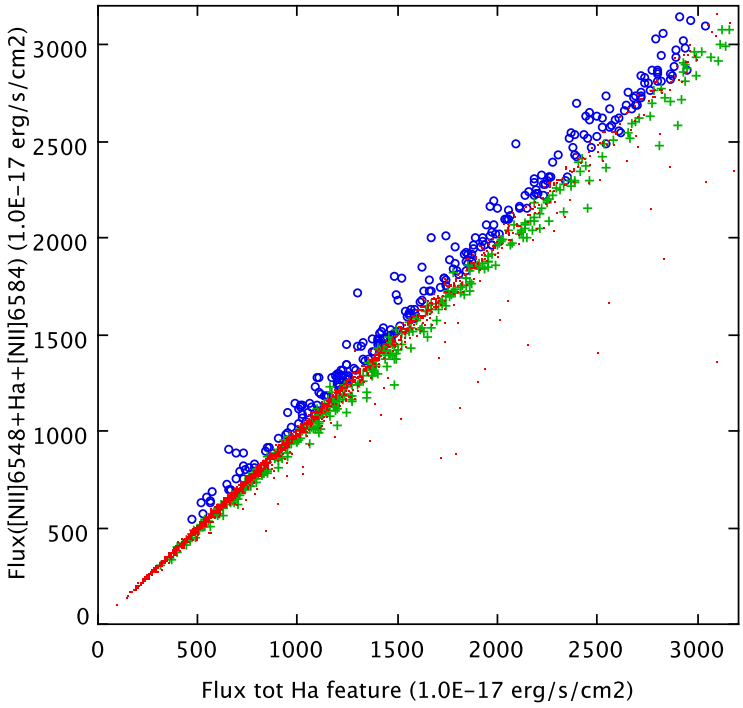

Figure 2.19: Sum of Gaussian fluxes used in the fit of $[NII]6548$, H_α and $[NII]6584$ vs the measured total flux of H_α feature. Narrow-line spectra are indicated with *red dots*, broad-line spectra with *blue circles* and the 820 re-fitted spectra (see the text) with *green plus*.

2.5 Classification with VO diagrams

The narrow-line spectra could be classified using directly the classical Veilleux & Osterbrock (1987) diagnostic diagrams, but some problems arised with the broad-line spectra and with the previously mentioned 820 spectra because the H_β line appeared overestimated by about $10-20$ percent when compared with the H_α flux. In some cases the H_α/H_β ratio is below 2.85 while this ratio is usually assumed to be 3.1 according to the Balmer Decrement. The H_β could have a second component (broad) even if it is not detected or it is underestimated when detected. A non-detection or an underestimate of the broad component could be due either to the limited sensitivity of the measure algorithm or to a low S/N ratio, such that the wings of the broad component are hidden in the noise. The detection of the broad component begins when its height is greater then σ_c at the borders of the narrow-line, so it is reasonable that a pedestal could be present in the H_β line when the broad component is seen only in the H_α. The H_β lines were manually measured in about 50 broad-line spectra by using a double Gaussian fit in order to define a possible relation between the H_α and H_β narrow component. So if the σ_{H_β} of the narrow component is assumed to be equal to the σ_{H_α}, expressed in km/s, a reasonable estimate of the expected narrow H_β flux can be calculated as it follows

$$F_{(H_\beta)} = \sqrt{2\pi}\,\sigma_{H_\alpha}\,(A-\sigma_c)\,4861.3/6562.8 \tag{2.4}$$

where the amplitude is reduced of the σ_c (the broad component could be detected if the amplitude was greater than σ_c). In Figure 2.20 the calculated $F_{(H_\beta)}$ vs the measured narrow H_β flux is plotted: the red filled circles show the sample measured by hand, the variation is very small and the correlation coefficient 0.97. Typical 1 σ error bars are shown in black. It is clear that the fluxes are very similar with few exceptions. The error on the calculated flux (σ_F) was obtained by applying the propagation on the errors of the amplitude and $\sigma_{H\alpha}$. This error is systematically lower than the measured one of a factor ~ 1.5, then we assumed as standard error $1.5\,\sigma_F$.

The amount of correction for the broad-line spectra is shown in Figure 2.21 where it is clear the trend between the measured $F(H_\alpha)/F(H_\beta)$ of the narrow components and the percentage contribution of the H_α broad component to the total H_α flux. When the H_α broad component increases the H_β overestimation increases. The circles show the $F(H_\alpha)/F(H_\beta)$ ratio after the application of the mentioned model, only few objects have the ratio below 3.

At this point it is possible to classify the spectra using the Veilleux & Osterbrock (1987) diagnostic diagrams. The galaxies of each family are classified using the relations introduced by Kewley et al. (2006). The diagnostic ratios were obtained using the H_β calculated flux for the broad-line spectra and the 820 spectra and the sum of the two components, when present, of the $[OIII]5007$ line. All the objects which can belong to the Seyfert regions within 1σ error in the diagnostic ratios are taken into consideration (Figures 2.22, 2.23, 2.24). After the classification there are three samples: 521 I-t Seyfert and 2153 S2, while 479 spectra are classified as S2 after the new fitting but they are not included in the previous sample, this sample is named Seyfert 2b (hereafter S2b). Of course these spectra show a larger $FWHM_{H_\alpha}$ compared with the S2. The median $FWHM_{H_\alpha}$ is 250 km/s for the S2 and 350 km/s for the S2b (Figure 2.25). Hereafter in the figures we will use the same colors when referring to the samples, red S2, green S2b and blue I-t.

In summary, out of 5678 spectra 1424 are excluded because they have not all the 8 diagnostic lines, another ~ 200 were excluded because their H_α could not be fitted (these are mostly Seyfert 1 and narrow line Seyfert 1), 3153 are Seyfert (S2, S2b, I-t) and about 900 are LINERS, composite and Star-burst galaxies. Hence about 85% of the entire sample

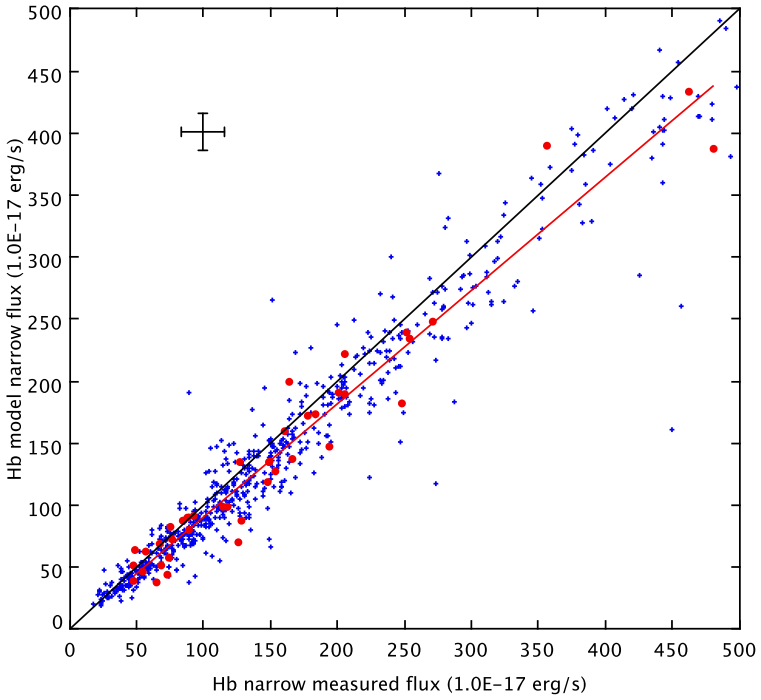

Figure 2.20: The calculated flux for the narrow H_β component vs the measured one for the Intermediate-type Seyferts (*blue plus*). *Red dots* are spectra measured by hand in order to determine a correction for the overestimate H_β fluxes. See the text for details.

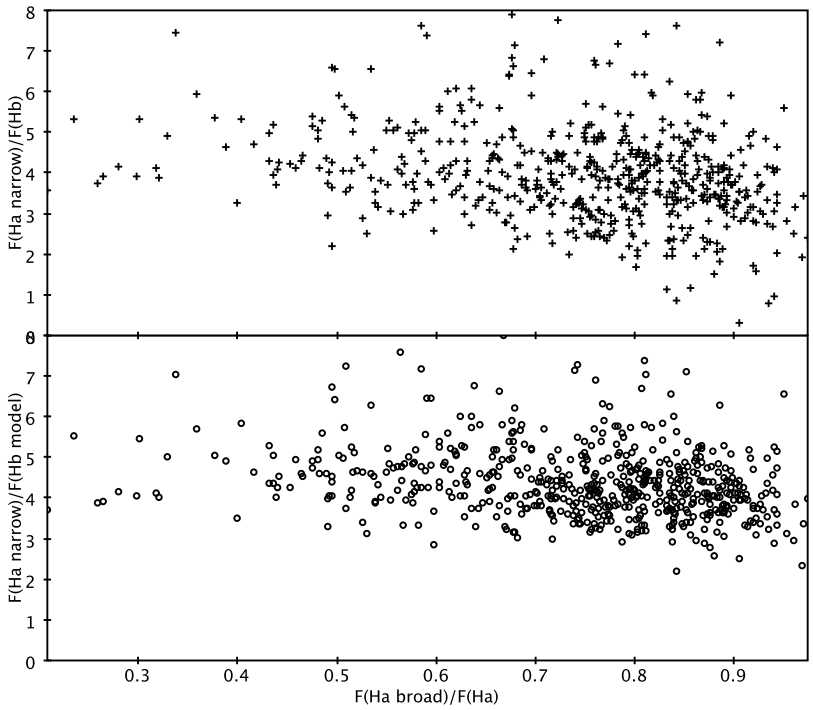

Figure 2.21: $F(H_\alpha)/F(H_\beta)$ narrow component vs the $F(H_{\alpha_{broad}})/F(H_\alpha)$, using the measured $F(H_\beta)$ (*top*), and the $F(H_\beta)$ model (*bottom*). The distribution using the H_β model has a low dispersion compared with the upper case and there are few spectra with ratio values lower than 3.

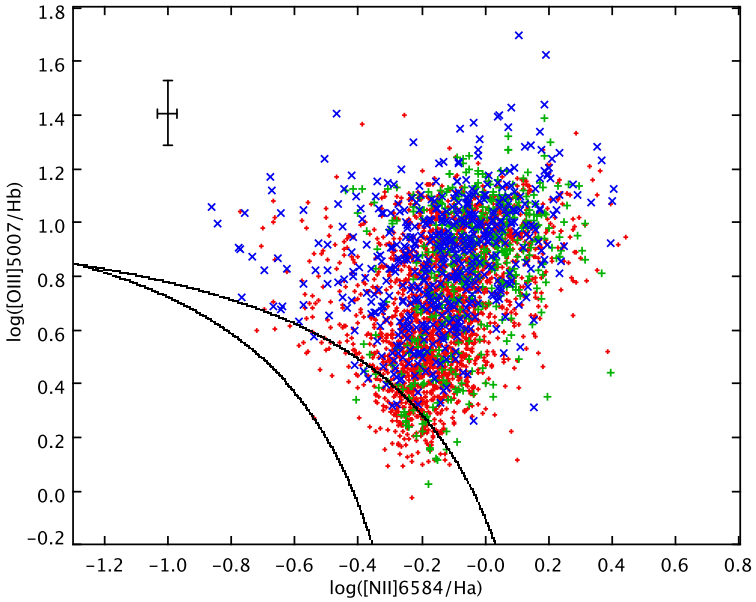

Figure 2.22: $log([OIII]5007/H_\beta)$ vs $log([NII]6584/H_\alpha)$. S2 sample is indicated with *red dots*, S2b sample with *green plus* and I-t sample with *blue crosses*. The lines separate the AGN region from composite and star-forming galaxies following the relation introduced by Kewley et al. (2006).

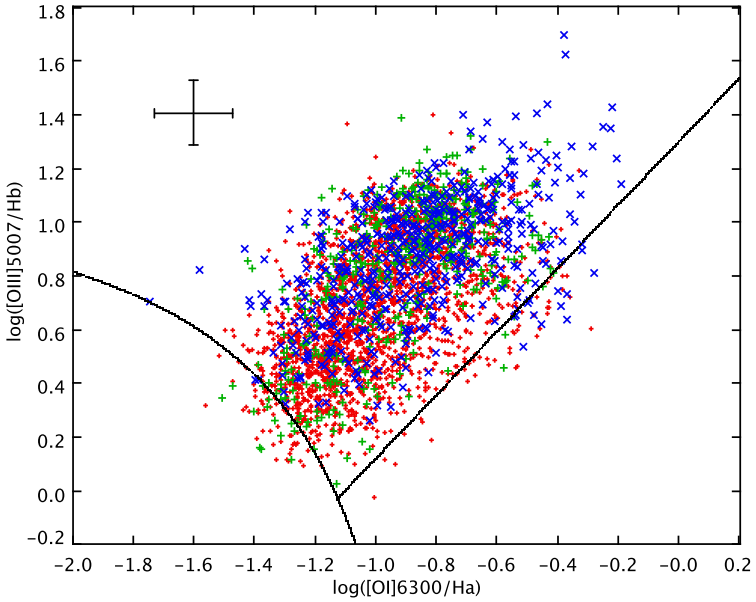

Figure 2.23: $log([OIII]5007/H_\beta)$ vs $log([OI]6300/H_\alpha)$. Symbols and colors are as in the previous figure. The stright line separates the Seyfert from the LINERS (Kewley et al., 2006).

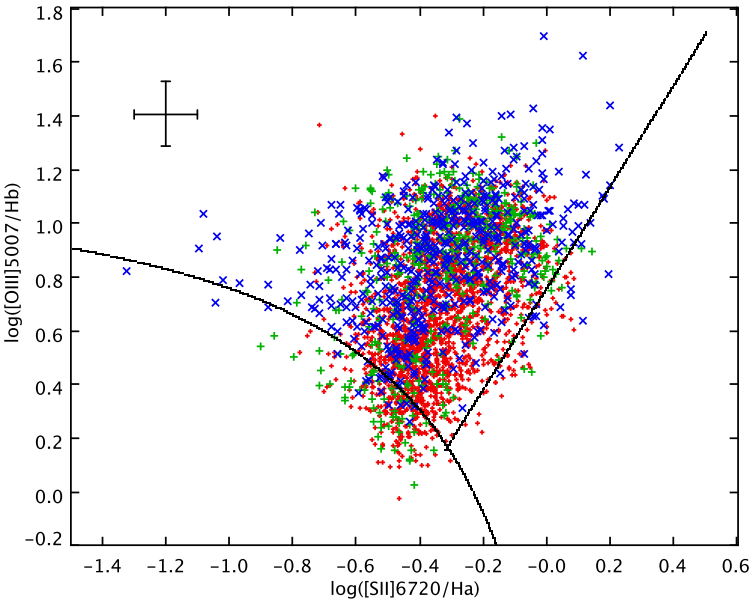

Figure 2.24: $log([OIII]5007/H_\beta)$ vs $log([SII]6720/H_\alpha)$. Symbols and colors are as in the previous figure. The stright line separates Seyfert galaxies from LINERS (Kewley et al., 2006).

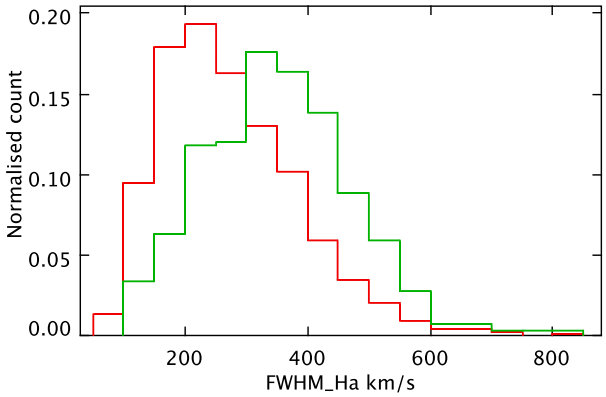

Figure 2.25: $FWHM_{H_\alpha}$ distributions of S2 (*red*) and S2b (*green*).

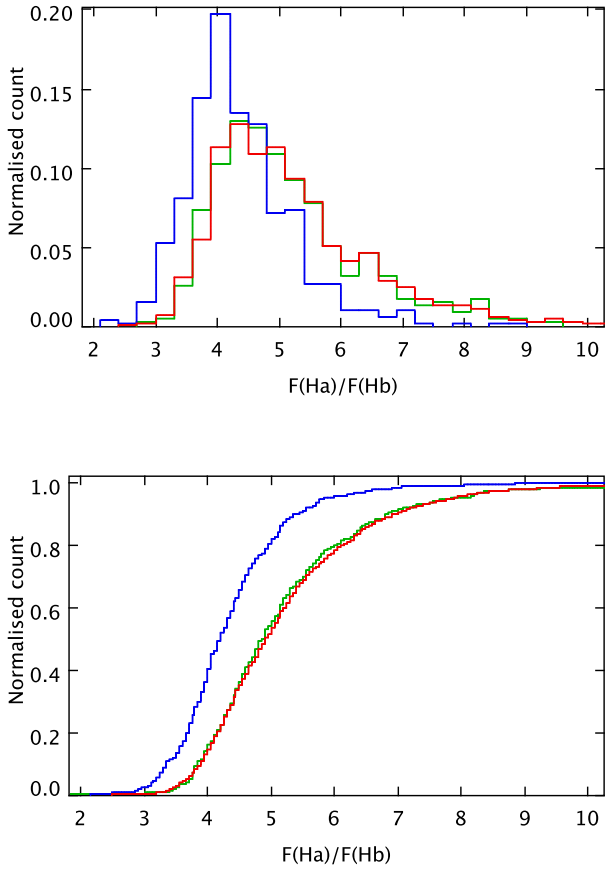

Figure 2.26: *top*: $F(H_\alpha)/F(H_\beta)$ ratio distribution for I-t (*blue line*), S2 (*red line*) and S2b (*green line*). *bottom*: $F(H_\alpha)/F(H_\beta)$ ratio cumulative distribution.

(acceptable spectra) are Seyfert galaxies. It means that the Oxygen diagram is really useful in the AGN selection.

In Figure 2.26 (*top*) $F(H_\alpha)/F(H_\beta)$ narrow component ratio distribution for the three samples is plotted. The I-t show a different distribution with lower $F(H_\alpha)/F(H_\beta)$ values, which could indicate a lower amount of extinction. The Kolmogorov-Smirnov test between S2 and I-t rejects the null hypothesis (H_0), that the two distributions are from the same parent population, at the 1% level of significance. The critical value of D[5] for the Kolmogorov-Smirnov two-sample test is 0.08, the obtained value is 0.3, whereas the S2 and S2b have the same distribution (Fig 2.26 *bottom*).

[5] $D = max[S_m(X) - S_n(X)]$ where $S_m(X)$ and $S_n(X)$ are the cumulative frequency distributions of two samples (Wall & Jenkins, 2003).

Chapter 3

Emission line analysis

3.1 Internal reddening

In the analysis presented in this chapter the internal reddening correction was calculated using the parametrization introduced by (Cardelli et al., 1989) under the assumption $H_\alpha/H_\beta = 3.1$ (Osterbrock & Ferland, 2006). Unfortunately the H_γ/H_β ratio is not reliable because H_γ has a low S/N in most of the spectra; furthermore this line was fitted with a single component, so when a broad component exists the fitting is wrong. In fact, we verified that for Seyfert 2 spectra with $S/N_{5500\mathring{A}} > 10$ the H_γ/H_β ratio assumes a value of 0.50 ± 0.05, which is higher than expected according to the Balmer decrement in the case of photo-ionization by a non-thermal source ($H_\gamma/H_\beta \approx 0.47$, Osterbrock & Ferland (2006)). Therefore, only the H_α/H_β ratio was used to estimate the internal extinction. Figure 3.1a shows the distributions of the derived values of A_V, the median values are 1.4 (90% of the sample has $A_V < 2.5$) for the S2 and 2b, 0.9 (90% of the sample has $A_V < 1.8$) for the I-t. Assuming a level of significance of 1%, the Kolmogorov-Smirnov test (Figure 3.1b) gives a clear difference of A_V between S2 and I-t. This result is in favour of the expected difference of the reddening between narrow and broad emission line objects, even if the correction for stellar component, obtained with STARLIGHT, is not completely reliable when the spectra show a strong broad component. The A_V values appear correlated, even if weakly, with stellar absorption (A_V*) evaluated by STARLIGHT (Figure 3.2). However the low values of A_V*, that are distributed in a smaller interval, would suggest that stars are located in a relatively unadsorbed region. while most of the dust is mixed to the gas of the NLR in all 3 classes of objects.

3.2 Line luminosities

The emission line luminosities were calculated from the reddening-corrected fluxes by using the z values provided by SDSS and assuming $H_o = 74.2\ km\ s^{-1}\ Mpc^{-1}$ (Riess et al., 2009). The distributions are not Gaussian, they are more similar to the Poissonian distribution, so it is more sensible to calculate the mode and the median values in order to compare the results of the three samples. Table 3.1 summarizes the number of line detections, the mean, mode and median values of luminosity (in units of $10^{40}\ ergs^{-1}$) for each line of each family. The 2nd, 7th and 13th columns report the class amplitudes employed in the calculation of the mode respectively for the S2, S2b and I-t. These amplitudes were found in such a way as to have a single absolute maximum in the luminosity distribution between 5 to 60 percent of the sample. With this condition we have a partition with the best resolution, not so high to

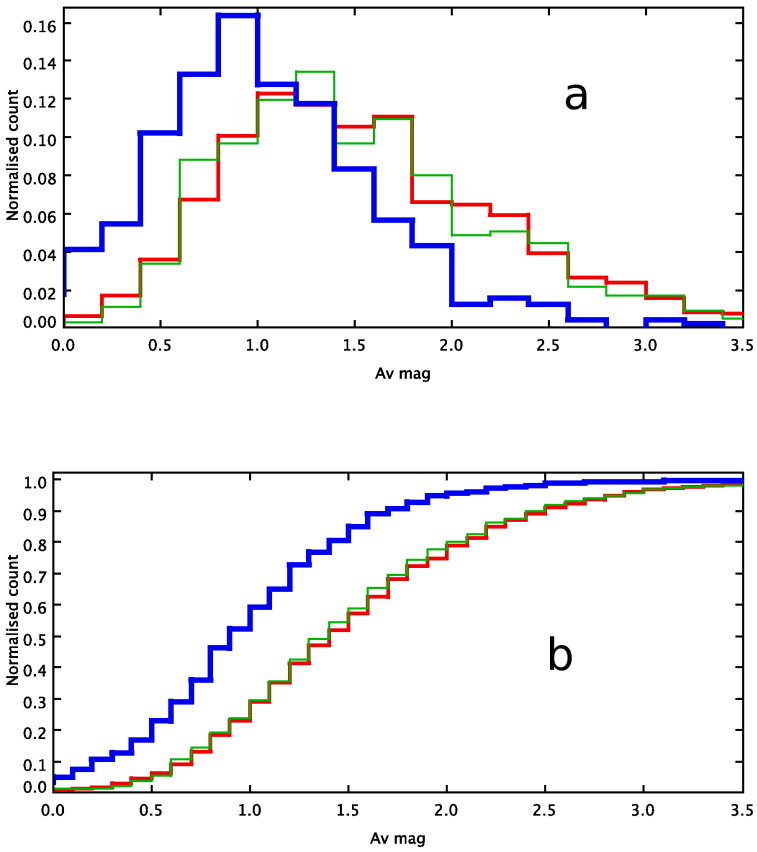

Figure 3.1: A_V distribution (a) and cumulative A_V distribution (b) for the samples: S2 (*red line*), S2b (*green line*) and I-t (*blue line*).

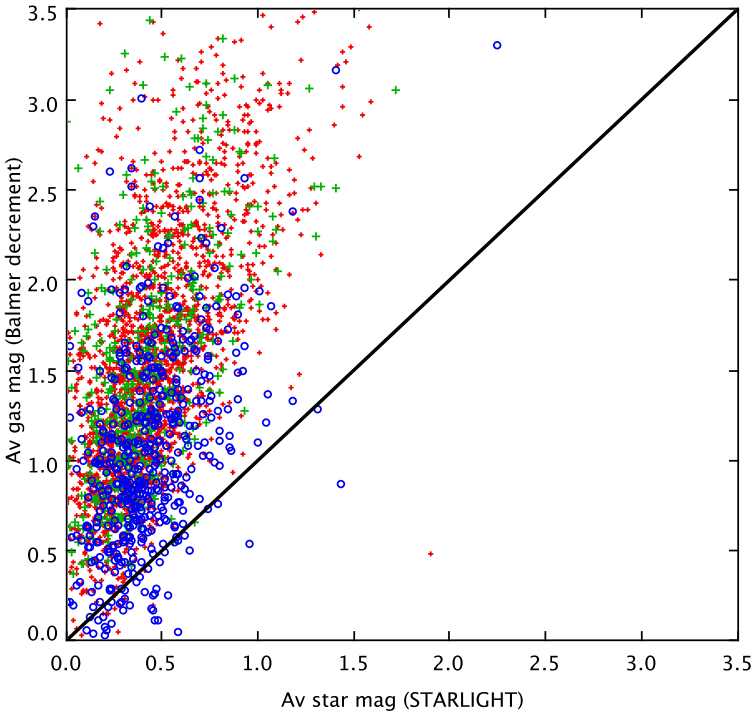

Figure 3.2: $A_{V_{gas}}$ vs $A_{V_{star}}$, the samples are indicated with the usual colors.

have more than a maximum and not so low to lose information in the distribution. The mean values were calculated after the exclusion of outliers that could heavily affect the mean.

Table 3.1: Mean, Mode and Median of the Luminosity distributions

line	amp	mean S2	mode S2	median S2	nobj S2	amp S2b	mean S2b	mode S2b	median S2b	nobj S2b	amp I-t	mean I-t	mode I-t	median I-t	nobj I-t
[OII] 3727	5.0	26.58	7.5	17.09	2153	2.0	14.07	5.0	10.75	784	5.0	19.71	7.5	12.71	521
[NeIII] 3869	2.0	5.31	3.0	3.64	1143	0.5	4.0	1.25	3.08	580	2.0	6.55	1.0	4.56	437
[NeIII] 3968	0.5	3.05	1.75	2.39	305	1.0	3.5	1.5	2.29	275	1.0	5.09	1.5	4.29	247
[SII] 4074	0.25	1.12	0.38	0.83	73	0.25	0.74	0.62	0.96	110	1.0	2.29	0.5	2.0	94
H_γ 4102	0.5	2.13	0.75	1.7	549	0.5	2.04	0.75	1.54	327					306
H_δ 4340	1.0	3.63	1.5	2.48	1309	0.5	2.73	1.25	2.02	581					445
[OIII] 4363	0.5	1.13	0.25	0.95	86	0.5	1.27	0.75	1.0	112	2.0	5.21	1.0	3.91	223
HeII 4686	0.5	1.55	0.75	1.33	362	0.25	1.46	0.38	1.32	233	1.0	2.19	0.5	1.78	201
[ArIV] 4711	0.5	0.58	0.25	0.5	13	0.1	0.8	0.25	0.5	22	0.25	0.44	0.38	0.5	10
[ArIV] 4740	0.5	0.88	0.25	0.75	16	0.25	0.34	0.38	0.47	22	0.5	0.54	0.25	0.38	7
H_β 4861	0.5	5.53	2.25	4.04	2153	1.0	3.85	1.5	2.76	784	1.0	5.16	1.5	3.74	521
[OIII] 4959	2.0	9.29	3.0	6.24	2072	2.0	8.76	3.0	5.95	772	5.0	19.87	7.5	13.26	293
[OIII] 5007	5.0	27.53	7.5	18.31	2153	5.0	29.66	7.5	18.35	784	10.0	40.01	15.0	28.91	446
[NI] 5199	0.5	1.44	0.25	0.96	169	0.5	1.34	0.25	0.83	158	0.5	1.26	0.25	1.21	90
[FeVII] 5721	0.25	0.65	0.62	0.67	29	0.5	0.8	0.75	0.81	41	0.5	0.8	0.75	0.83	51
HeI 5876	0.1	0.87	0.35	0.8	277	0.25	1.03	0.38	0.93	176	1.0	3.53	0.5	2.32	197
[FeVII] 6087	0.25	0.79	0.12	0.64	96	0.5	1.04	0.25	0.89	83	0.5	1.26	0.75	1.06	97
[OI] 6300	0.5	1.9	0.75	1.35	2153	0.25	1.71	0.62	1.4	784	0.5	2.26	1.25	1.52	521
[OI] 6364	0.25	0.81	0.38	0.62	343	0.25	0.93	0.38	0.67	264	0.25	1.17	0.38	0.94	192
[NII] 6548	1.0	4.67	1.5	3.27	2153	0.5	3.77	0.75	2.59	784	0.5	4.03	1.25	2.8	521
H_α 6563	2.0	17.57	7.0	12.5	2153	2.0	11.13	3.0	8.32	784	2.0	13.11	3.0	11.39	521
[NII] 6584	2.0	12.78	5.0	9.29	2153	2.0	11.36	3.0	7.59	784	1.0	9.92	3.5	8.09	521
[SII] 6716	0.5	4.05	1.75	3.13	2153	1.0	3.95	1.5	2.76	784	1.0	3.98	1.5	2.75	521
[SII] 6731	1.0	3.5	1.5	2.58	2153	0.5	3.25	1.25	2.34	784	0.5	2.57	0.75	2.32	521
[ArIII] 7135	0.25	0.79	0.38	0.67	226	0.25	0.95	0.38	0.81	195	0.25	1.14	0.62	0.94	118
[OII] 7320	0.25	0.36	0.12	0.41	41	0.25	0.35	0.38	0.4	33	0.25	0.48	0.38	0.5	19
[OII] 7330	0.25	0.45	0.38	0.41	41	0.25	0.34	0.12	0.34	32	0.5	0.62	0.25	0.6	19

Notes. The values are expressed in unit 10^{40} $erg\ s^{-1}$. *amp* is the class amplitude used in the distributions (see the text). *nobj* is the number of spectra used in the statistics.

Table 3.2: Number of spectra with two components in the $[OIII]4959, 5007$ lines

Sample	№ objects	$[OIII]4959$	$[OIII]5007$
S2	2153	605	1383
S2b	479	297	431
I-t	521	293	446

The H_γ and H_δ of I-t are excluded from this analysis because a single Gaussian was employed in their fitting, so their fluxes are not reliable. There is coherence between the NLRs of these three families with the exception of the recombination lines, and $[OII]3727$ and $[OIII]4363, 5007$ (Figure 3.3). The I-t show higher luminosity values in $HeI5876$, $[OIII]4363, 5007$, about double with respect to the other families. The $HeI5876$ emission-line was fitted with a single Gaussian but in many cases shows a broad component, so the flux is not totally related to the NLR, instead the $[OIII]$ lines are intrinsically more luminous. The H_α has a lower luminosity compared to the Seyert 2, whereas there is about the same value for the S2b. It is interesting to point out the $[OII]3727$ case where the S2 show a higher luminosity. This could be due to the reddening correction but it seems quite unlikely, and there are no systematic effects on nearby emission-lines. A possible explanation could be a different ionization level of the gas, greater for the I-t (the higher the ionization, the higher the $[OIII]5007/[OII]3727$ and $[OIII]5007/[OI]6300$ ratios).

3.2.1 [OIII]4959,5007

The $[OIII]5007/4959$ luminosity ratio of the total sample, with the condition $(S/N)_{4959} > 10$ in the line flux is 3.03 ± 0.23 (2193 objects) coherently with the theoretical ratio ($[OIII]5007/4959 = 2.98$, Dimitrijević et al. (2007)). The $[OIII]$ lines of many spectra were fitted with two components in order to achieve a good χ^2. Table 3.2 reports the numbers of spectra with two components in the $[OIII]$ lines. Figure 3.4 show the luminosity ratio distribution respectively for the total luminosity, the 1st component and 2nd component. In some cases, it appears that when the components are treated singularly the ratio is not consistent with the theoretical value. In these cases the secondary component is a mere result of the fitting. But in the vast majority of the cases the secondary components are real as we will see later in the profile analysis (§6.2.2). Looking at the FWHM, the first component was assumed to be the narrowest and the second the broadest. The number of spectra with secondary components in both $[OIII]$ lines are 1141, whereas 819 show the secondary component only in $[OIII]5007$ line.

Considering only spectra showing two components in both the $[OIII]$ lines, we note that: i) there is a large difference in percentage about the number of spectra with two components between S2 and the other two samples (Table 3.3); ii) the total $[OIII]4959, 5007$ luminosities are greater when there are two components (Figure 3.5); iii) there is no significative difference between the samples in the $[OIII]5007$ luminosity distribution. These observations could be explained either assuming a greater absorption when the lines are narrow or an actual greater gas quantity in the NLR when two components are necessary in the fitting. In the first case the I-t should be seen deeper inside the NLR. In the second one the S2 NLRs had low gas mass compared to the Intermediate Seyfert. The third observation tells us that the ionized gas mass is comparable between the components.

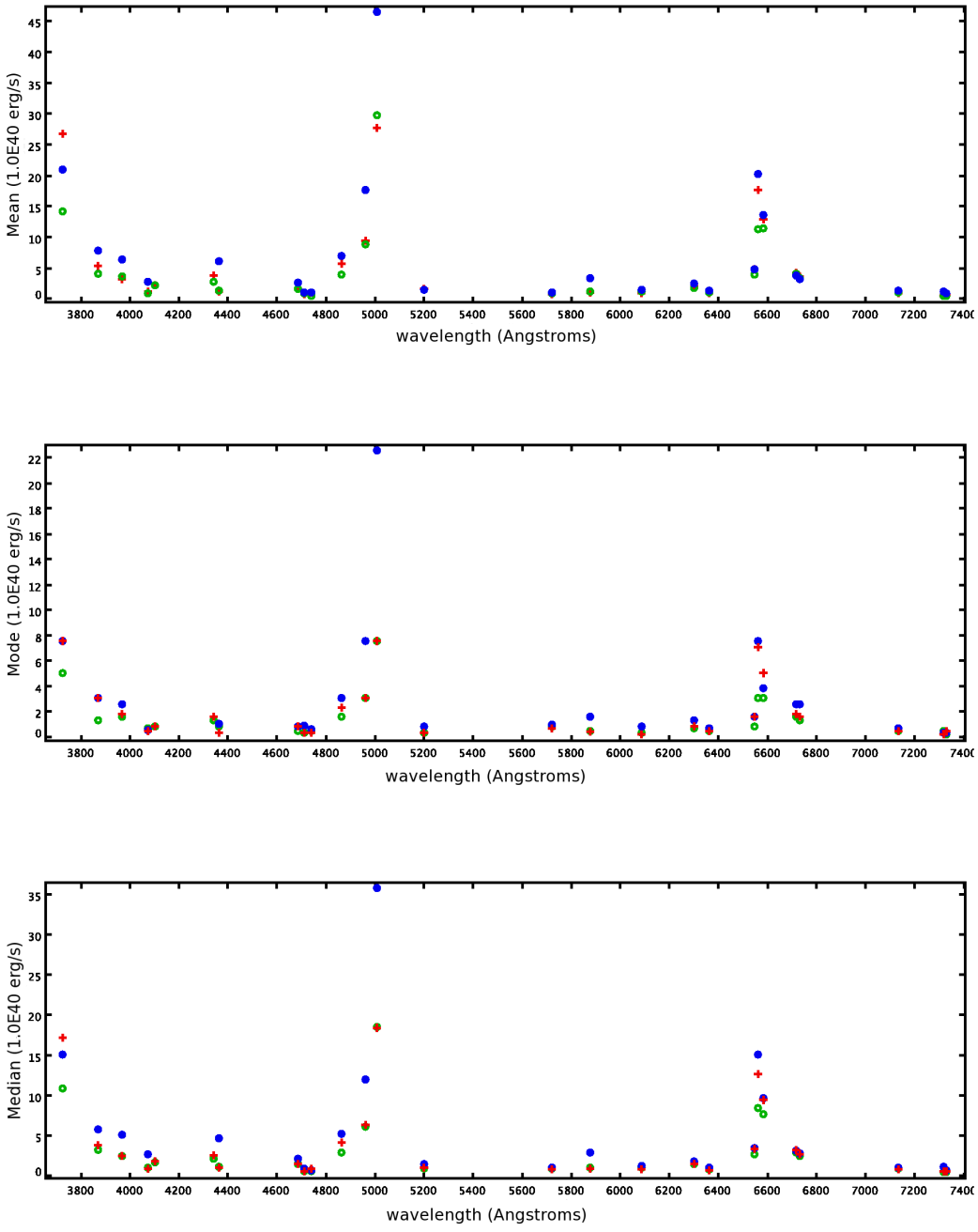

Figure 3.3: mean, mode and median luminosity of the measured lines for each sample. S2, S2b and I-t are indicated with *red crosses*, *green open circle* and *fill blue circles* respectively.

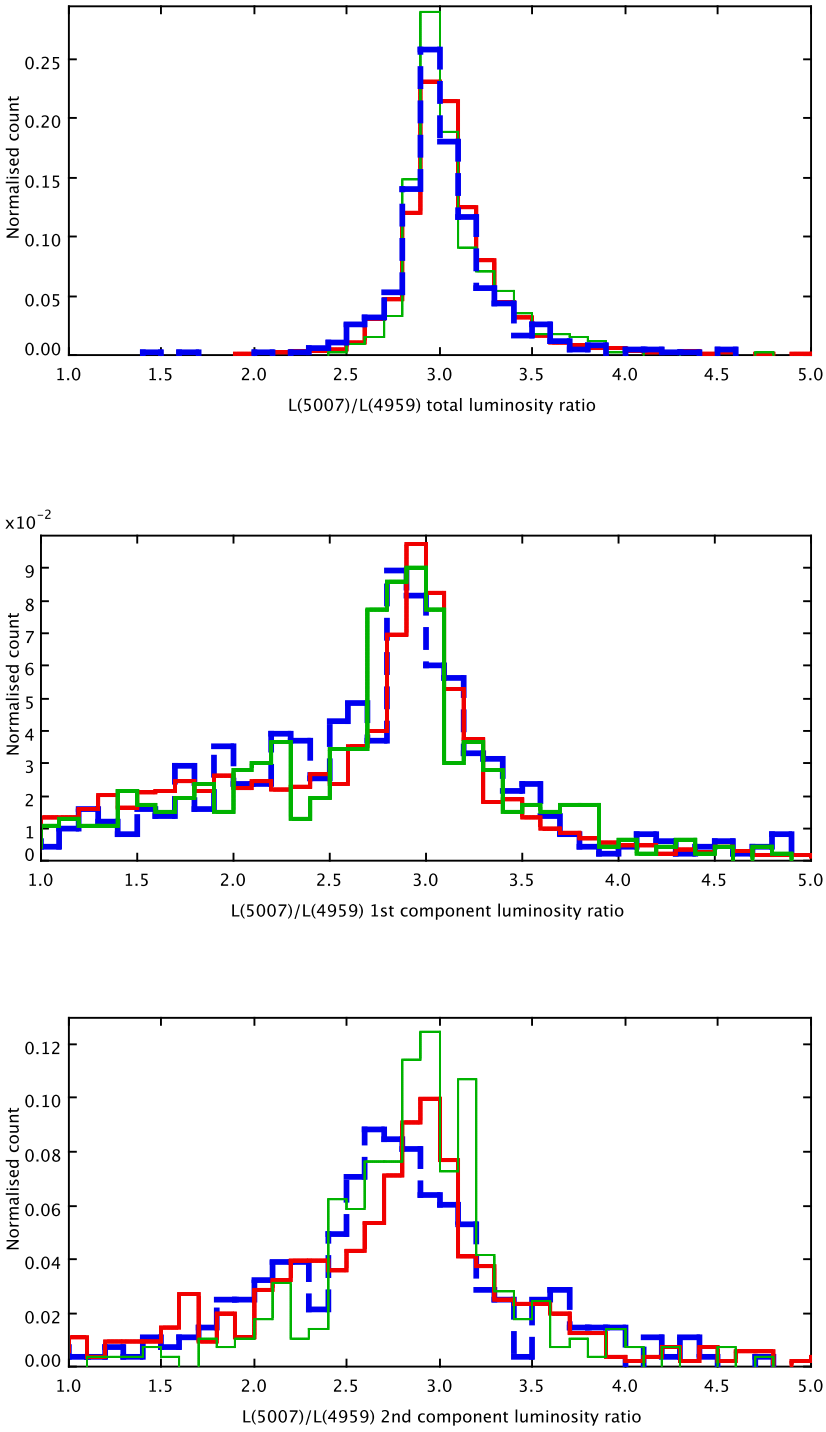

Figure 3.4: [*OIII*]5007/4959 ratio luminosity distribution. The different colors and line styles represent the samples: S2 (*red line*), S2b (*green line*) and I-t (*blue dashed line*).

Table 3.3: $[OIII]4959, 5008$ luminosity of two components

Sample	line	mean	mode	median
S2	4959 1st	9.9	1.5	4.5
565	4959 2nd	12.3	2.5	5.5
26%	5007 1st	29.6	7.5	15.5
	5007 2nd	34.9	7.5	15.2
S2b	4959 1st	12.2	3.0	7.5
291	4959 2nd	15.0	6.0	8.2
61%	5007 1st	36.5	15.0	24.0
	5007 2nd	43.9	12.5	24.0
Intermediate	4959 1st	10.6	3.0	6.0
285	4959 2nd	12.3	3.0	5.3
55%	5007 1st	32.3	7.5	21.0
	5007 2nd	33.1	7.5	14.5

Notes. The table summarizes the luminosity distribution paramenters (mean, mode and median) of the $[OIII]4959, 5007$ lines (the values are expressed in units 10^{40} $erg\,s^{-1}$). For each sample there are the number of spectra with the second component in both the lines, the percentage as respect with the total number of spectra and the parameter values for 1st and 2nd component for $[OIII]4959$ and $[OIII]5007$ respectively.

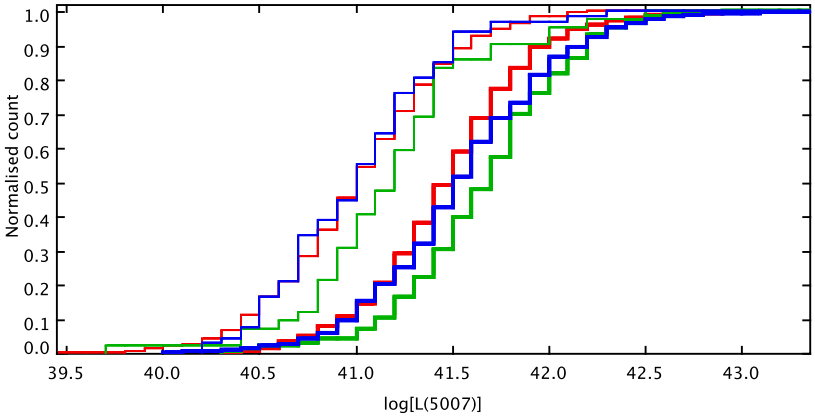

Figure 3.5: $[OIII]5007$ Luminosity cumulative distributions: *thin line* when the $[OIII]5007$ is fitted by a single Gaussian, *thick lines* when two Gaussians are necessary. Colors are as in Figure 3.4.

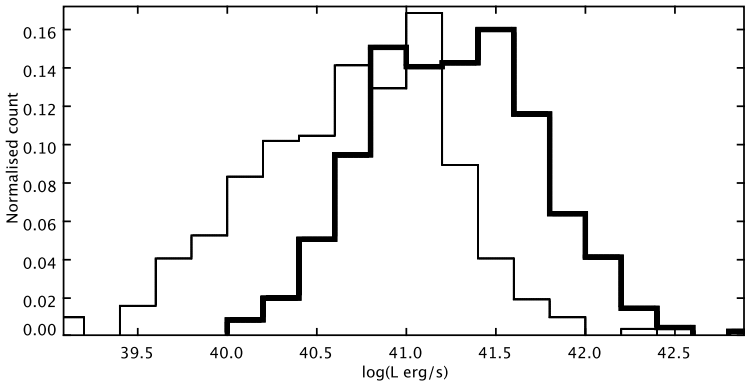

Figure 3.6: Log luminosity distributions of H_β (*thin line*) and H_α (*thick line*).

3.2.2 Balmer lines broad component

In the Intermediate Seyfert sample the H_β broad component was fitted in 327 spectra, although it is possible that in some other cases the broad component could be really present, depending on the adopted measurement criteria. In any case even if the H_β broad component is measured it is difficult to determine correctly the Balmer decrement because the H_β wings are confused in the noise and the flux may be underestimated. Additionally, the STARLIGHT correction is not particularly good in the Intermediate Seyfert spectra. Nevertheless, it could be interesting to see the observed luminosities of the broad component, overall for H_α much easier to determine. In the Figure 3.6 we show the observed H_α and H_β luminosities of the broad components; these values are slightly lower than the luminosity distributions founded by La Mura et al. (2007) in their samples (broad line emitting objects and NLS1).

Figure 3.7 shows the observed Balmer decrement of the broad component for I-t sample. The peak value is around 4, in agreement with Osterbrock & Ferland (2006) ($H_\alpha/H_\beta \sim 4.9$). When the density is higher than $\sim 10^{10}\, cm^{-3}$ (a typical BLR density) the H_β emission line is weakened because the collisions enhancement. The H_α/H_β ratio shows an extended tail toward the high values (73 objects show a ratio > 10); this could be due to the H_β underestimation even if there is no correlation or particular trend between the $(S/N)_{H_\beta}$ and the Balmer decrement.

3.3 Line intensity correlations

The emission-line fluxes normalized to H_β and corrected for reddening were analysed following the Koski method (Koski, 1978). They were subdivided in high and low ionization lines (Table 3.4) and the relative fluxes were plotted versus the $[OIII]5007$ or $[SII]6720$ relative flux assumed as reference lines. Koski introduced another diagram, $HeI5875$ vs $HeII4686$ in order to compare the Helium recombination lines. These diagrams show the correlations between lines with similar ionization state, Figures 3.8, 3.9. There is a good correspondence with the Koski diagrams but with many more objects, although the mean S/N of our spectra is lower than Koski spectra's. The choice of the limits in the axes diagrams was performed excluding very few objects, max 5 in each diagram, with too high values of fluxes. These spectra showed very high errors or high χ^2 in the fitting so these measures were not reliable.

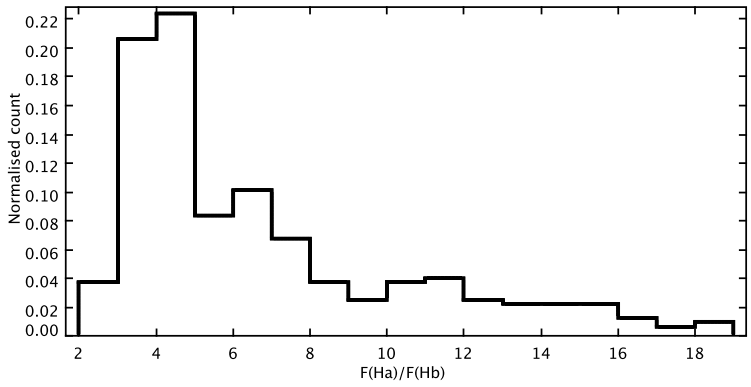

Figure 3.7: $F(H_\alpha)/F(H_\beta)$ broad component distribution of the I-t sample.

Table 3.4: Correlation coefficients between lines of similar ionization potential

	S2			S2b			It		
$[OIII]$5007 vs									
	m	c	r	m	c	r	m	c	r
$[NeIII]$3869	0.1	0.1	**0.7**	0.1	0.2	**0.7**	0.1	0.3	**0.7**
$[ArIII]$7135	0.0	0.0	**0.7**	0.0	0.0	**0.8**	0.0	0.0	**0.7**
$HeII$4686	0.0	0.1	**0.6**	0.0	0.1	**0.6**	0.0	0.2	**0.4**
$[SII]$6720 vs									
	m	c	r	m	c	r	m	c	r
$[OII]$3727	2.8	0.9	**0.5**	3.0	0.2	**0.6**	1.9	1.0	**0.6**
$[NI]$5199	0.1	0.1	**0.3**	0.1	0.1	**0.6**	0.0	0.0	**0.5**
$[OI]$6300	0.3	-0.1	**0.8**	0.3	0.0	**0.8**	0.3	0.0	**0.8**
$[NII]$6584	1.1	0.8	**0.6**	1.1	1.2	**0.7**	0.9	1.0	**0.7**

Notes. m is the angular coefficient, c is the intercept and r is the correlation coefficient.

Table 3.4 shows there are the linear interpolation coefficients, m and c, with the correlation coefficients, r. There is no correlation between the HeI and $HeII$ lines, as found by Koski. In the case of I-t sample these lines should be fitted by two components because many times the helium lines show a broad component. $[NeIII]$3869, $[ArIII]$7135 and $HeII$4686 lines show a good correlation with the $[OIII]$5007 line. The result is consistent with Koski one for S2. The other two samples show similar results, except for a tendency towards higher values in I-t, although with more scatter. Weaker or even absent correlation between lines with very different ionization potentials supports the existence of two independent ionization zones. This is confirmed by the analysis of the gas density and velocity dispersion. Other high ionization lines are $[FeVII]$5721,6087 and $[ArIV]$4711,4740; these lines do not show any correlation with the $[OIII]$5007 line. The $[FeVII]$ lines are coronal lines and are very peculiar (see next paragraph), they may originate from shock-heated gas and have an higher critical density compared to the $[OIII]$ lines. The $[ArIV]$ lines have higher ionization potential and lower critical density, therefore these lines could be formed in different regions compared with the $[OIII]$ lines. There are good correlations between lines with similar critical density: $[SII]$6720 vs $[OII]$3727 and $[NI]$5199 just seen before; $[ArIII]$7135 vs $[OII]$7325 with a correlation coefficient $r \sim 0.6$ for S2 and S2b, but a null coefficient for the I-t sample; $[ArIII]$7135 vs $[NeIII]$3869 with $r \sim 0.5 \div 0.7$, the higher values being found for the I-t sample. There is no correlation between $[ArIII]$7135 and $[OI]$6300 and $[SII]$4074, these lines have similar critical densities but a very different ionization potentials.

3.4 Line intensity distributions

A comparison between the three families of Seyfert galaxies was performed by applying the Kolmogorov-Smirnov test (Wall & Jenkins, 2003) to the line intensity distributions. It is interesting to note that if we assume an increase of the excitation degree from S2 to I-t, due to an increase of the radiation field hardness, it is possible to explain and to describe the discrepancy or similarity between the samples. The test was performed only for lines that were measured in a sufficient number of objects. The nebular lines that have a constant ratio with their homologue were excluded. The lines in Table 3.5 were considered. This table lists the number of spectra involved for each family and the Kolmogorov-Smirnov test value for the rejecting hypothesis (H_0) assuming 1% significance. There are three additional columns, one for each combination between the samples. Different significant values were adopted (between 0.5% to 10%) but with no substantial difference in the results. The partition adopted in the line intensity distributions was 0.1, the intensities are normalized to H_β. The intensities adopted were corrected by reddening but the same results can be obtained using the relative fluxes (no-reddening corrected line intensities) or using H_α line intensity as reference for the lines in the red spectral range. Table 3.6 lists the measured values D, and its last three columns contain a flag, 1 if the H_0 is accepted and 0 if it is rejected.

Figures 3.10, 3.11 show the cumulative distributions used in the Kolmogorov-Smirnov test. The results are analysed line by line, because every spectral line has a different behaviour and peculiarities depending on the sample.

$[OII]$3727: the distributions of S2 and 2b are similar and the I-t sample has lower intensity.

$[NeIII]$3869: the distributions of S2b and I-t are similar, the S2 sample has lower intensity.

$[SII]$4074: the distributions show a trend between the samples with S2 $\sim$ S2b and S2b $\sim$ I-t.

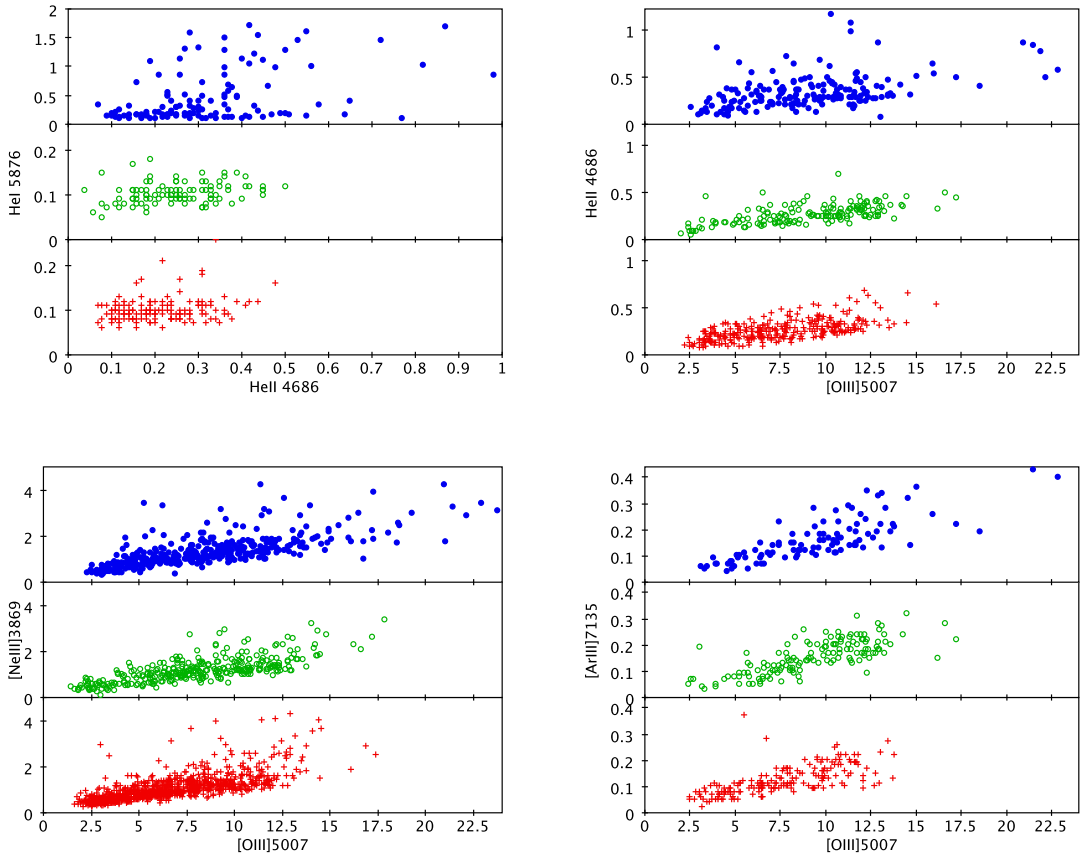

Figure 3.8: Koski diagrams, high ionization lines. The fluxes are relative to H_β and corrected by reddening.

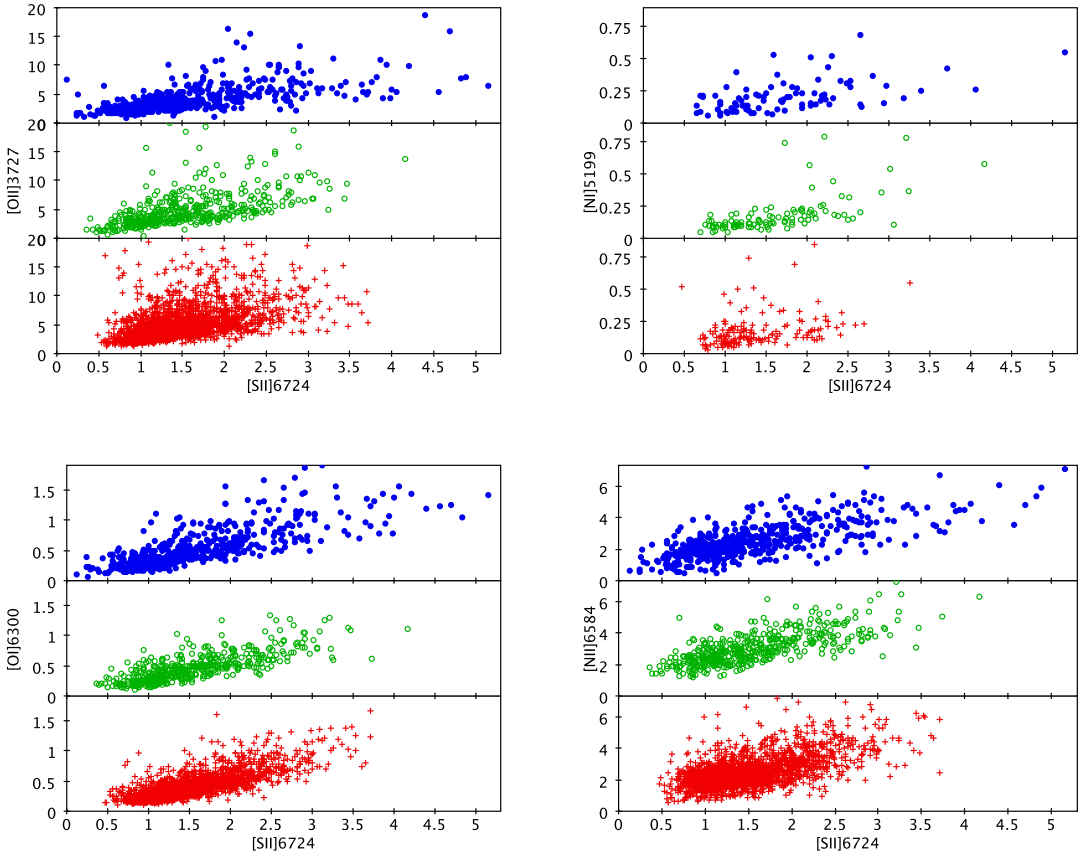

Figure 3.9: Koski diagrams, low ionization lines.

Table 3.5: Number of objects involved in the line analysis and the theoretical Kolmogorov-Smirnov values with 1% significance (KS) for the rejecting hypothesis H_0

line	№ S2	№ S2b	№ I-t	(S2 ↔ S2b)$_{KS}$	(S2 ↔ I-t)$_{KS}$	(S2b ↔ I-t)$_{KS}$
[OII]3727	2153	479	521	0.08	0.08	0.10
[NeIII]3869	1143	349	437	0.10	0.09	0.12
[SII]4074	73	87	94	0.26	0.25	0.24
[OIII]4363	86	79	190	0.25	0.21	0.22
HeII4686	362	165	201	0.15	0.14	0.17
[OIII]5007	2153	479	521	0.08	0.08	0.10
[NI]5199	169	105	90	0.20	0.21	0.23
[FeVII]5721	29	38	51	0.40	0.38	0.35
HeI5876	277	138	197	0.17	0.15	0.18
[FeVII]6087	96	68	97	0.26	0.23	0.26
[OI]6300	2153	479	521	0.08	0.08	0.10
[NII]6584	2153	479	521	0.08	0.08	0.10
[SII]6717	2153	479	521	0.08	0.08	0.10
[SII]6731	2153	479	521	0.08	0.08	0.10
[ArIII]7135	226	151	118	0.17	0.19	0.20

Table 3.6: Kolmogorov-Smirnov measured values with 1% of significance (D). The flag is equals 1 when the hypothesis is accepted, 0 when it is rejected

line	(S2↔S2b)$_D$	(S2↔I-t)$_D$	(S2b↔I-t)$_D$	S2↔S2b	S2↔I-t	S2b↔I-t
[OII]3727	0.05	0.19	0.14	1	0	0
[NeIII]3869	0.19	0.21	0.06	0	0	1
[SII]4074	0.24	0.32	0.22	1	0	1
[OIII]4363	0.08	0.74	0.66	1	0	0
HeII4686	0.03	0.17	0.15	1	0	1
[OIII]5007	0.27	0.29	0.10	0	0	1
[NI]5199	0.03	0.15	0.19	1	1	1
[FeVII]5721	0.09	0.26	0.34	1	1	1
HeI5876	0.06	0.57	0.57	1	0	0
[FeVII]6087	0.08	0.29	0.29	1	0	0
[OI]6300	0.18	0.20	0.10	0	0	1
[NII]6584	0.26	0.08	0.20	0	1	0
[SII]6717	0.07	0.10	0.06	1	0	1
[SII]6731	0.09	0.11	0.05	0	0	1
[ArIII]7135	0.16	0.14	0.08	1	1	1

Table 3.7: Number of spectra with $[FeVII]$ and $[OIII]4363$ lines and their percentage respect to the samples.

samples	[FeVII]5720	[FeVII]6086	[FeVII]5720,6086	[OIII]4363	[OIII]4363+[FeVII]6086
S2	29 (1%)	96 (4%)	26 (1%)	86 (4%)	38 (2%)
S2b	38 (8%)	68 (14%)	34 (7%)	79 (16%)	49 (10%)
I-t	51 (10%)	97 (19%)	48 (9%)	186 (36%)	73 (14%)

$[OIII]4363$: There is a good correspondence between S2 and S2b, the I-t ones show a totally different distribution with a much more intense line.

$HeII4686$: the numerical result is the same obtained with $[SII]4074$ although there is a better correspondence between S2 and S2b.

$[OIII]5007$: the hypothesis is accepted between S2b and I-t.

$[NI]5199$: The distributions are similar for all the samples.

$[FeVII]5721$ and $[FeVII]6087$: both these lines are consistent with a similar distribution, the intensity of these lines is greater in I-t sample. The hypothesis is accepted between S2 and S2b for $[FeVII]6087$, the more intense line. For $[FeVII]5721$ the test is positive for all the combinations but in this case the line is weak and visible only in few objects.

$HeI5876$: there is a perfect correspondence between S2 and S2b, while the hypothesis is rejected for I-t. In this case the line is very intense compared with the other samples.

$[OI]6300$: the hypothesis is accepted at the limit between I-t and S2b, rejected in the other cases.

$[NII]6584$: the S2b sample show a strange distribution, the intensity is higher compared to the other samples but this could be due to a systematic effect on the flux measure, since part of $[NII]6584$ flux could be affected by a possible H_α broad component.

$[SII]6717$ and $[SII]6731$: these lines have the same trend, even if numerically there are some little differences in the obtained values. The distributions are similar for all the samples. Formally the hypothesis is accepted for both the lines between S2b and I-t.

$[ArIII]7135$: the hypothesis is accepted for all the sample combinations.

From Table 3.6 it appears that the emission line distributions are coherent between S2 and S2b, and between S2b and I-t types or are common about all the samples. From this analysis it appears that S2b resemble to S2, with a little more ionization degree if we consider $[NeIII]3869$ and $[OIII]5007$ line distributions. Therefore, we speculate that the H_α broad component, if it is present, is not so large.

3.5 $[FeVII]5720, 6086$ coronal lines

$[FeVII]5720, 6086$ coronal lines were detected in few spectra over all the samples but the percentage as well as the relative intensity of the lines, increase from S2 to I-t (Table 3.5).

These coronal lines are formed in the coronal line region (CLR) and are very important in the analysis of the NLR structure. In the context of the Unified Model three kinds of CLR exist (Murayama & Taniguchi, 1998), those associated with the torus ($\sim 1\ pc$), with the NLR ($10 - 100\ pc$) and with the ENLR ($\sim 1\ kpc$, these values are the CLRs distances from the source). The luminosities of these lines are higher in I-t, thus suggesting that the emitting gas mass is greater compared to S2. Since the CLR is present in S2 and I-t, it should be associated with the NLR or ENLR. In order to achieve the conditions to form the coronal lines far away from the source we need a low density medium which is well described

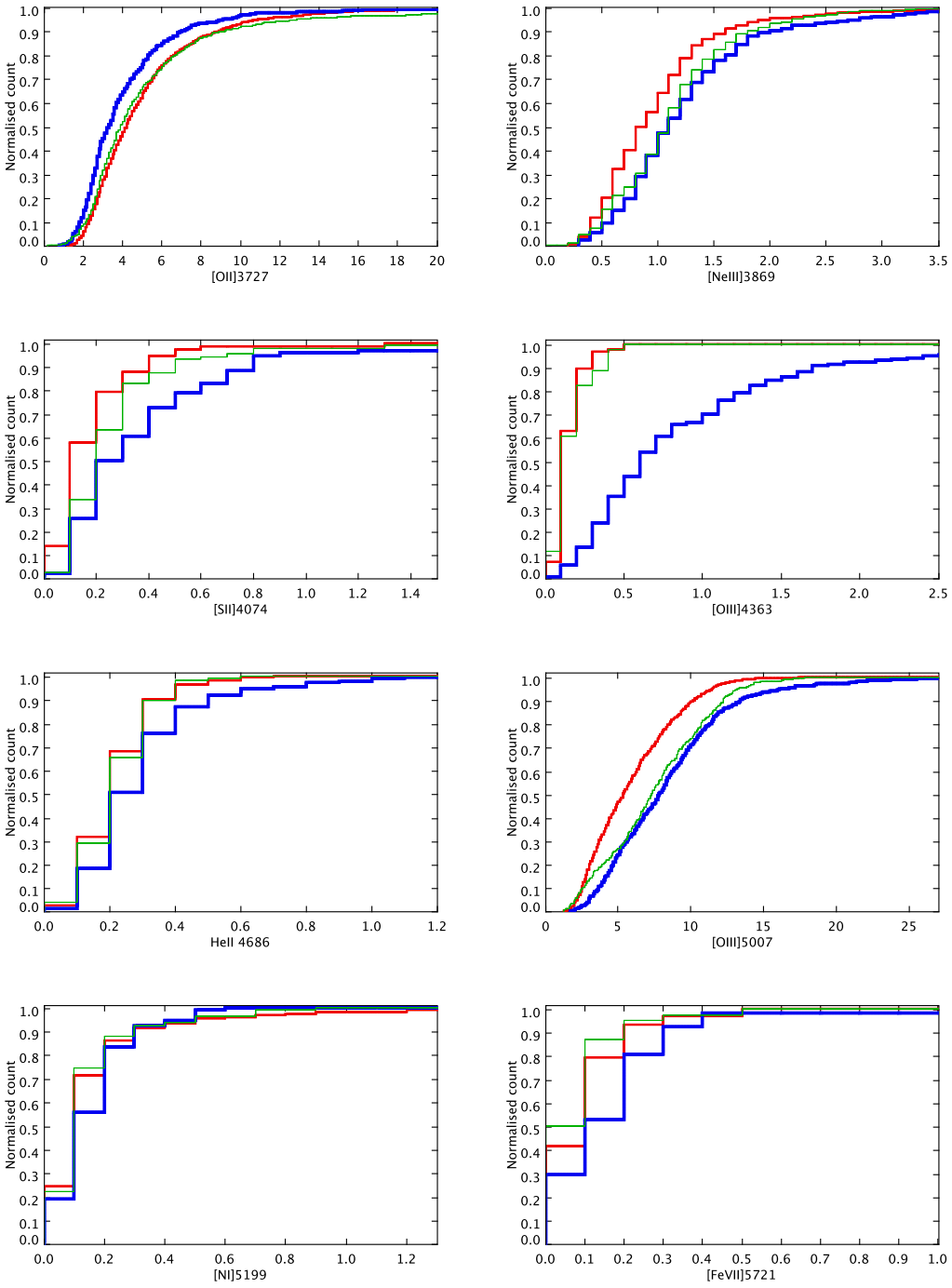

Figure 3.10: The cumulative distributions of emission line fluxes. The different colors and line styles represent the samples: S2 (*red line*), S2b (*thin green line*) and I-t (*thick blue line*).

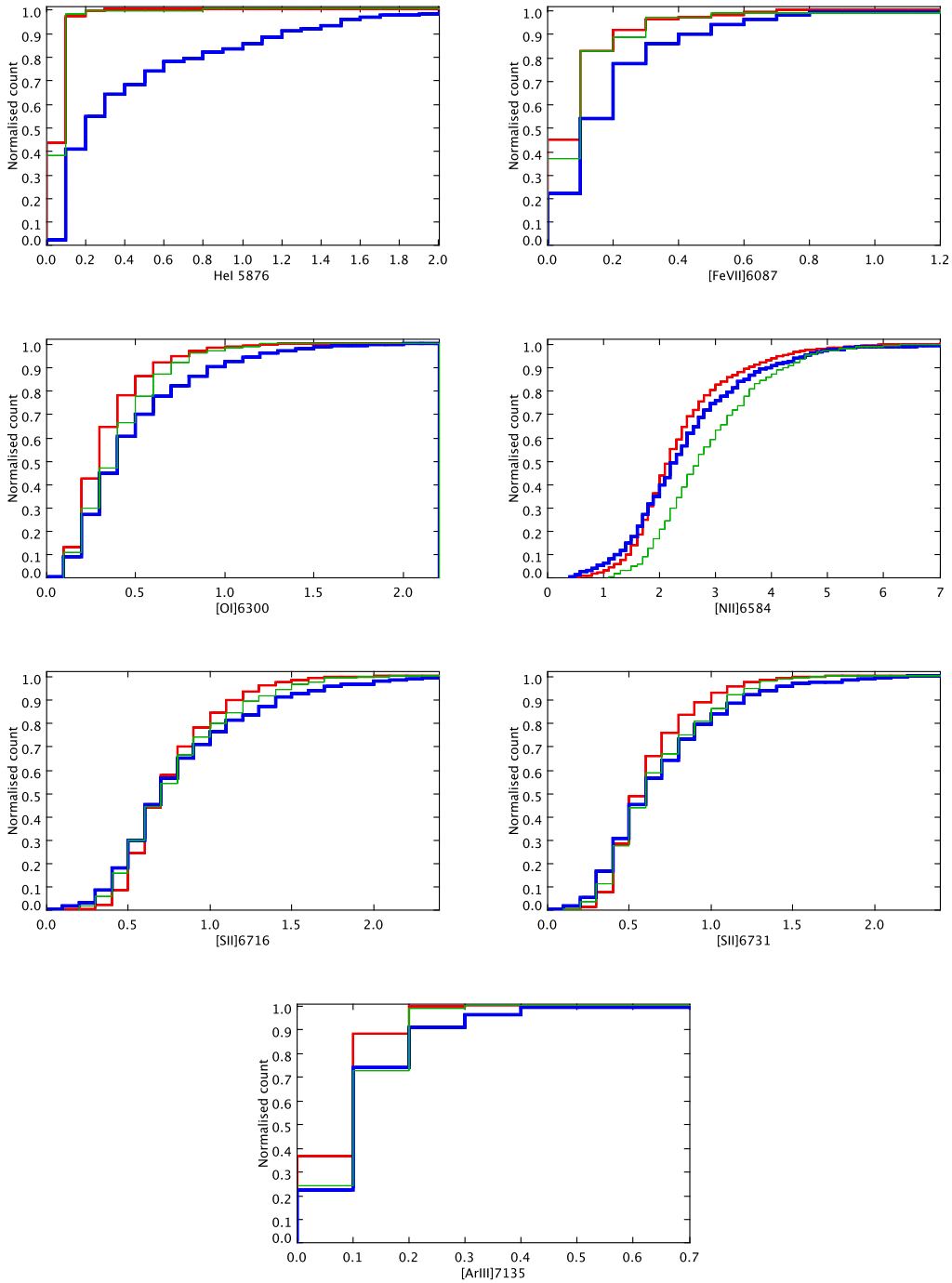

Figure 3.11: The cumulative distributions of emission line fluxes. Symbols and colors are as in Figure 3.10.

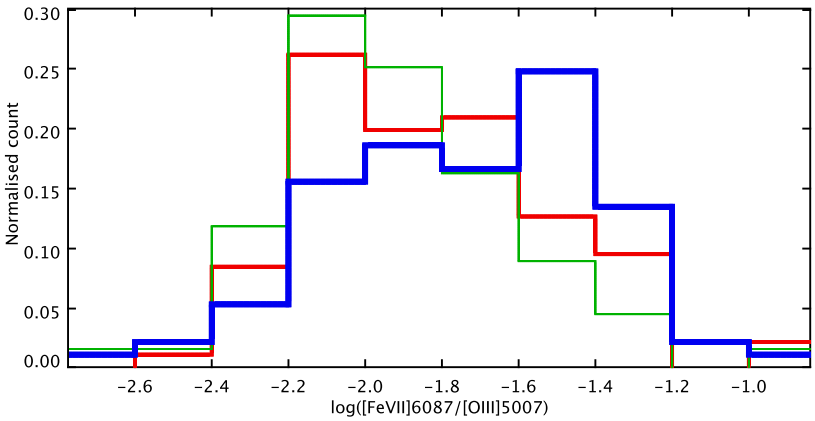

Figure 3.12: $log([FeVII]6087/[OIII]5007)$ distribution. Symbols and colors are as in Figure 3.10.

by matter bounded cloud models. We confirm the distribution of $[FeVIII]6087/[OIII]5007$ (Figure 3.12) obtained by Murayama & Taniguchi (1998) for S2 and S2b. In the I-t case the distribution shows greater values and the difference with the other samples is confirmed by the Kolmogorov-Smirnov test. This is consistent with the authors which showed a difference of this distribution between Seyfert 1 and 2 analysing 17 S2 and 18 Seyfert 1. The same is true for the $[FeVII]5720$ even if in this case there are really few objects over all for the S2 sample. These coronal lines are relatively rare in S2 sample but they are very weak therefore spectra with high S/N ratio are necessary before drawing a final conclusion.

Since the critical density of the $[FeVII]6087$ line is very similar to that of the $[OIII]4363$ line, following Nagao et al. (2001), we analyzed the correlation between these two lines (Figure 3.13): the correlation is good with a coefficient 0.55 and 0.56 respectively for S2 and S2b, while the correlation is weak for I-t, with coefficient 0.41, as a possible consequence of a more uncertain measure of the flux, because of the presence in some cases of a broad H_γ component. It is interesting to note that the S2 and S2b have about the same slope of the linear regression whereas the I-t has the same trend but with a greater dispersion and a more intense $[OIII]4363$ line. This is consistent with the assumption that in I-t Seyfert we are observing the inner regions of the NLR.

From Table 3.5 it appears that the detection of $[FeVII]6086$ line does not imply the detection of $[OIII]4363$ line, even if there is correlation when both lines are present. About 50% fifty percent of the cases where the $[OIII]4363$ line is detected shows the $[FeVII]6086$ line. The same critical density is not a sufficient condition to support the idea that these lines are formed in the same region. In fact the ionization potentials are very different. So it is reasonable to think that the emitting regions of these lines are partially overlapping.

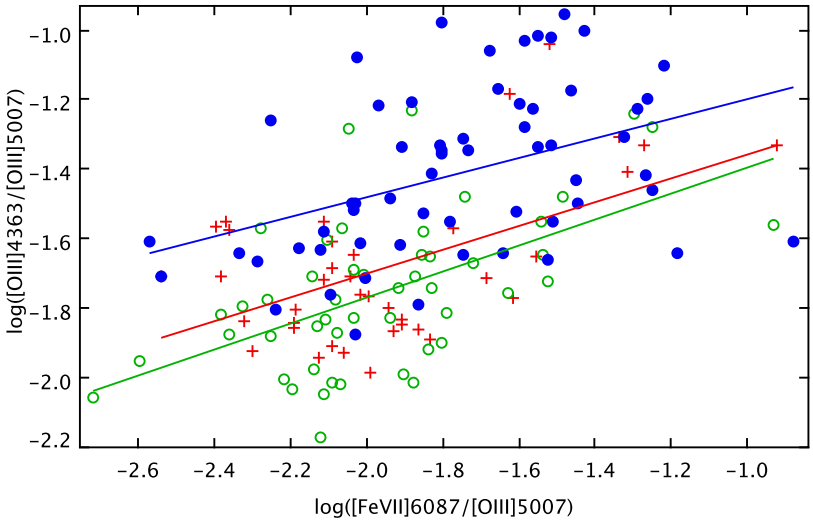

Figure 3.13: $log([OIII]4363/[OIII]5007)$ vs $log([FeVII]6087/[OIII]5007)$. The different colors and symbols represent the samples: S2 (*red plus*), S2b (*green open circles*) and I-t (*blue solid circles*). The lines show the linear regression with the usual meaning of the colors.

Chapter 4

Physical characteristics

4.1 Densities and Temperatures

The values of density and temperature were calculated using different line ratios in order to study regions having different physical properties. Calculations were performed by means of the IRAF task TEMDEM. The line ratios used to determine the densities were $[SII]6717/6731$ (hereafter RS2) and $[ArIV]4711/4740$ (hereafter RAr4) (Aller, 1984) for a few objects, while for the temperature the used ratios were $[OIII](4959+5007)/4363$ (hereafter RO3), $[SII](6717+6731)/(4068+4076)$ (hereafter RS2t), $[OII]3727/7325$ (hereafter RO2). A temperature of $10000K$ was assumed for the density determination. Figure 4.1 shows the distribution of the densities calculated by means of RS2. This ratio was measurable in all spectra, but reliable estimates of the density were possible in 2752 out of the 3153 objects (87% of the total sample), 1846 S2, 436 S2b and 469 I-t. The median value is $Ne \sim 250\,cm^{-3}$, and most objects show values lower than $500\,cm^{-3}$ (~ 2300 galaxies), while only in 97 cases we observe densities higher than $1000\,cm^{-3}$. RAr4 was available only in 30 objects, and in 26 it was possible to estimate the density, 7 S2, 15 S2b and 4 I-t. The obtained values are typically of the order of some $10^3\,cm^{-3}$ (Figure 4.2). This is not unexpected, since these [Ar IV] transitions are characterized by critical density values higher than those of the [S II] lines. Therefore they are probably emitted by gas in different physical conditions with respect to the one emitting sulphur lines. Interestingly, $[OIII]4363$ which shares the same ionization interval, has a even higher critical density, and this means that the gas emitting this line has also a larger electron density, likely around $10^4\,cm^{-3}$ or even more. Moreover, both lines $[ArIV]4711$ and $[ArIV]4740$ are generally weak, also after reddening correction, showing median intensities normalized to H_β of 0.07 and 0.09, respectively. We explored a possible correlation between the S/N ratio of the stellar continuum and the observed fluxes of the two $[ArIV]$ lines, finding that most of the spectra where they could be detected and measured have S/N ratio between 20 and 40. So, we can at least conclude that these lines are visible only in few objects, because spectra with high S/N ratio in the continuum are mandatory. Anyway, this could be only a necessary but not sufficient condition. Indeed, 66% of our sample has $S/N > 20$. Moreover, one can speculate for example that $[OIII]4363$ has a median intensity only twice higher than $[ArIV]4711$ and $[ArIV]4740$, and it was detected in 351 spectra having S/N ratio between 15 and 40, notwithstanding the fact that Oxygen is about 200 times more abundant than argon, assuming solar abundances. Therefore, it is also possible that the gas of the NLR is made essentially by a low and a high density medium, and that the second one has the electron density necessary to collisionally populate the Oxygen auroral line and simultaneously suppress the $[ArIV]$ lines.

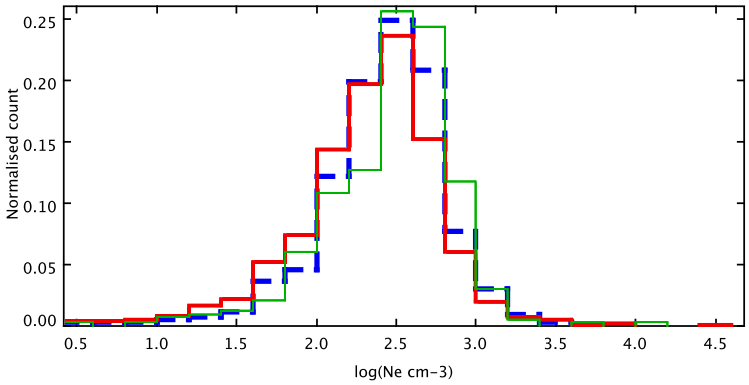

Figure 4.1: Density distributions calculated from RS2. The different colors and line styles represent the samples: S2 (*red line*), S2b (*green thin line*) and I-t (*blue dashed line*). Hereafter these colors will be used with the same meaning.

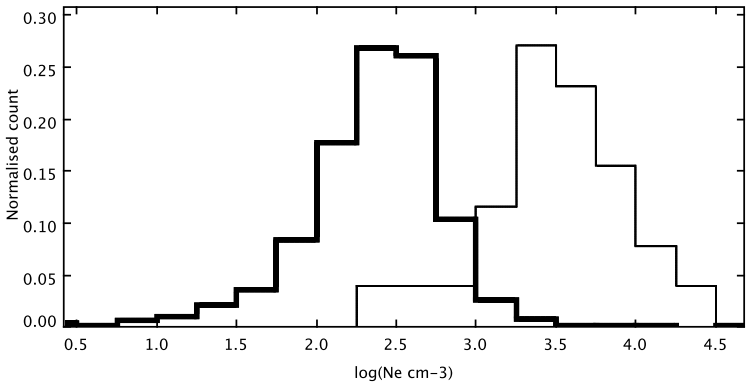

Figure 4.2: Density distributions calculated from RS2 (*thick line*) and RAr4 (*thin line*).

Table 4.1: T_e median values for the samples

Sample	$T_{e[OIII]}$	$T_{e[OII]}$	$T_{e[SII]}$
S2	17500	12000	11000
S2b	16000	13000	13000
I-t	25000	10000	15000

The temperature determinations are very difficult because the lines involved in the calculation are very weak and an intensity error of 30% is enough to get meaningless result. So the calculated values are only indicative and they must be seen as mean properties of the samples. RO3 reliable estimates were obtained in 333 spectra, 84 S2, 79 S2b and 170 I-t. RO2 is available for 98 spectra, 68 S2, 17 S2b, 13 I-t. Finally for RS2t there are 182 reliable measures, 63 S2, 66 S2b and 53 I-t. Figure 4.3 shows the distributions of the so determined temperatures for each sample while the median values are reported in Table 4.1. The electron density used as input in TEMDEN is the one obtained by RS2. Through a two-sample Kolmogorov-Smirnov test it appears that the distributions of the temperatures derived from [O II] and [S II] are very similar for the S2, with a significance of 1%. H_0 is accepted if $D < 0.3$ (§4.2). On the contrary, the temperatures obtained from [O III] have a completely different distribution ($D = 0.75$). In principle, this result could be indicative of the presence of ions stratification according to the ionization potentials. On the other hand, one can argue that it could be simply the effect of the use of $N_{e[SII]}$, which indicate electron density values too low to collisionally pump the [O III] λ4363, and that the use of $N_{e[ArIV]}$ is more correct. We made a simple exercise by introducing $N_e = 3 \cdot 10^4\, cm^{-3}$ in TEMDEN and re-calculating the temperatures. The resulting distribution is similar to the previous one, according to the Kolmogorov-Smirnov test ($D = 0.1$ where the null hypothesis is 0.3), while it is necessary to increase the density up to $N_e = 10^5\, cm^{-3}$ in order to observe a significant change. In particular, the median value of the temperature ($T_{e[OIII]}$) obtained with $N_e = 10^5$ is $13200K$ and this new distribution is quite similar to those obtained with $T_{e[OII]}$ and $T_{e[SII]}$. We can conclude that $[OIII]4959, 5007$ are likely emitted both by a low density medium at higher temperature reflecting ions stratification, and by high density clouds with high ionization, where the physical conditions are such as to allow the $[OIII]4363$ to form and become detectable and measurable.

In the I-t, the $[OIII]4363$ line was measured by hand because of the presence of the H_γ broad component which can affect the results. In any case high values of temperatures were obtained. This could be an effect of a residual broad component or an indication that we are actually observing the inner part of the NLR.

4.2 Kinematics

4.2.1 Velocity dispersion

The measured $FWHM$ ($FWHM_m$) was corrected for instrumental broadening to obtain the intrisic $FWHM$ ($FWHM_i$). As a value for the instrumental width we used the nominal value of the SDSS spectral resolution, $R = 1800$ (Burles et al., 1999) which corresponds to $167\, km/s$.

$$FWHM_i = \sqrt{(FWHM_m \cdot c/\lambda_i)^2 - 167^2} \quad km/s \tag{4.1}$$

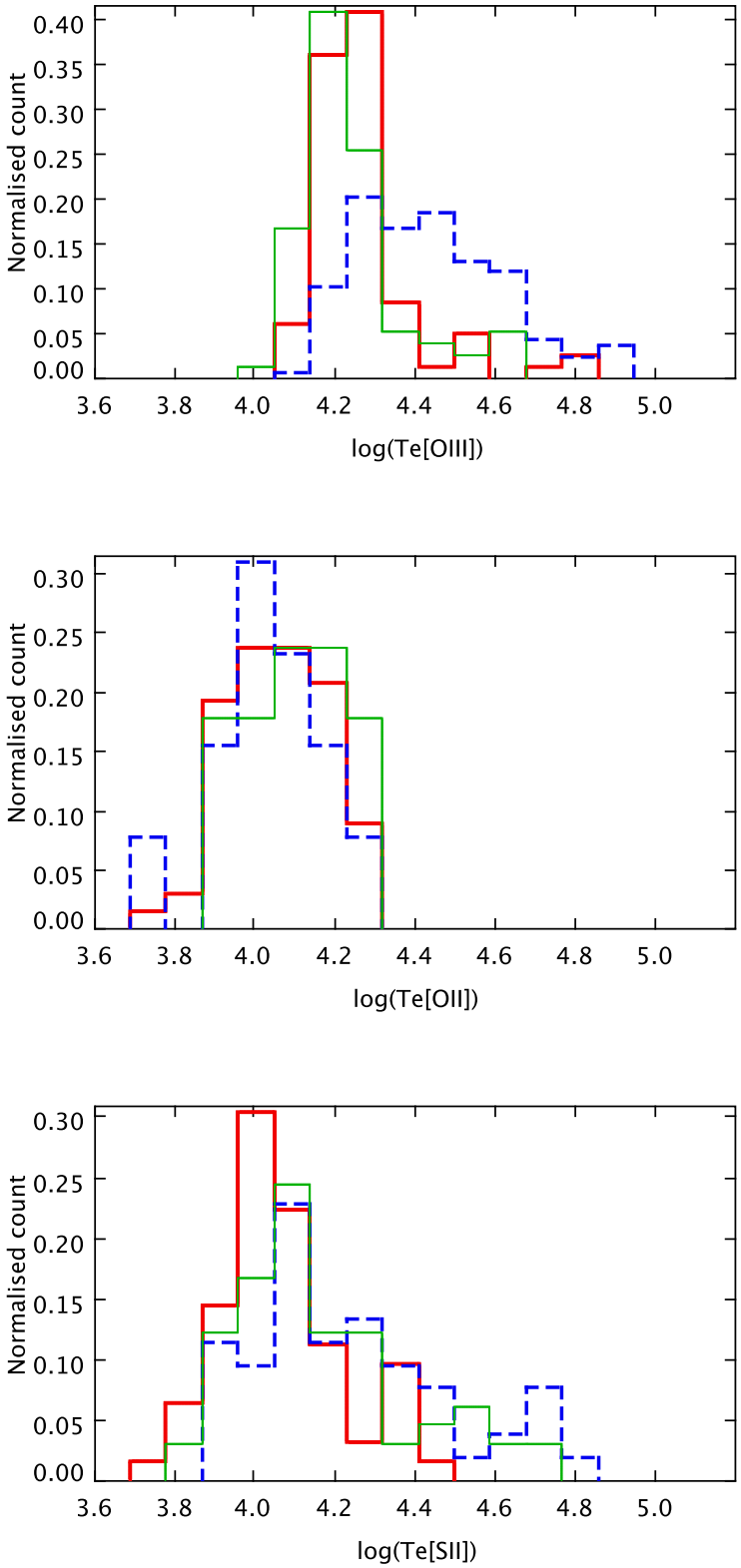

Figure 4.3: $log(T_e)$ distributions: $T_{e[OIII]}$ (*top*), $T_{e[OII]}$ (*middle*), $T_{e[SII]}$ (*bottom*). Each figure shows the three samples, colors and line styles are as in Figure 4.1.

Table 4.2: Correlation coefficients between $FWHM_{star}$ vs $FWHM_{gas}$

		S 2			S 2b			I-t	
	m	c	r	m	c	r	m	c	r
H_β	0.6	1.0	**0.6**	0.5	1.1	**0.5**	0.3	1.6	**0.5**
H_α	0.6	0.8	**0.7**	0.4	1.3	**0.5**	0.4	1.5	**0.5**
$[OI]6300$	0.5	1.2	**0.5**	0.4	1.4	0.4	0.3	1.8	0.3
$[NII]6584$	0.7	0.7	**0.7**	0.6	1.0	**0.5**	0.4	1.6	0.4
$[SII]6716$	0.6	0.9	**0.6**	0.5	1.0	**0.5**	0.3	1.8	0.3
$[SII]6731$	0.6	1.0	**0.6**	0.6	1.0	**0.5**	0.2	1.9	0.3
$HeII4686$	0.2	1.8	0.3	0.3	1.5	0.3	0.2	2.0	0.2
$[NeIII]3869$	0.4	1.5	0.4	0.2	1.9	0.2	0.2	2.0	0.2
$[OIII]5007$	0.5	1.0	**0.5**	0.3	1.5	0.3	0.2	1.9	0.2

We compared the $FWHM_i$ with the stellar velocity dispersion obtained with STARLIGHT. Since a low S/N ratio leads to a large scatter and often to an overestimate of the $FWHM$, we considered only the most intense lines, namely: H_β, H_α, $[OI]6300$, $[NII]6584$, $[SII]6716,6731$, $[NeIII]3869$, $[OIII]5007$ and $HeII4686$. All these lines shows about the same $FWHM$, $290 \pm 20\ km\ s^{-1}$, $340 \pm 40\ km\ s^{-1}$, $330 \pm 40\ km\ s^{-1}$, respectively for Seyfert2, S2b and Intermediate-type. There is no remarkable correlation between $FWHM$ and ionization potential or critical density: this could suggest the same kinematics for each ion. The linear and correlation coefficients between $FWHM_{star}$ and $FWHM_{gas}$ are listed in Table 4.2. The correlation coefficients greater than 0.5 are indicated in bold. It appears that in the S2 galaxies there is a correlation between these $FWHM$ with the exclusion of $[NeIII]3869$ and $HeII4686$. The correlations progressively weaken toward the I-t where only the Balmer lines show a weak correlation. We note that in the S2 sample, the low ionization lines show a better correlation, except for the $[OI]6300$ which is a rather weak line. The diagrams of $FWHM_{star}$ vs $FWHM_{gas}$ are shown in Figure 4.4 for the lines H_β, H_α, $[NII]6584$ and $[OIII]5007$. The difference between $[OIII]5007$ and the other lines is clear, only for S2 the Balmer lines and $[NII]6584$ show an acceptable correlation. It is interesting to point out that the same result (correlation index 0.48) for $[OIII]5007$ was found by Nelson & Whittle (1996). If only the narrowest $[OIII]5007$ component (§3.2.1) is used in the analysis the correlations are worse, 0.4 for the S2 and 0.2 for the other samples. In conclusion this analysis confirms the results of Botte et al. (2004) and Greene & Ho (2005), $[OIII]5007$ is not a good indicator of stellar velocity dispersion.

Following Koski (1978) we calculated the mean $FWHM$ ($km\ s^{-1}$) for each object and we compared the distribution in Figure 4.5 with his result (see his figure 4). We found a single distribution, where Koski found a double peaked distribution but he considered S2, narrow components of I-t and narrow-line radio galaxies. In his opinion the miminum at 500 $km\ s^{-1}$ has no physical significance and we confirm it. The cumulative distribution (Figure 4.5) shows that S2 have a significantly lower $FWHM$ compared to the other samples ($D > 0.08$), while S2b and I-t have the same distribution ($D < 0.3$).

In many cases $[OIII]5007$ is fitted by two components, a narrower (hereafter 1st component) and a broader component (hereafter 2nd component, see next section). Figure 4.6 shows the $FWHM_{[OIII]5007}$ distributions for both the components. $FWHM_{[OIII]5007}$ values are systematically lower in the S2 sample with respect to the other samples. The largest difference is in the 2nd component: the median value is $550\,km/s$ for S2 and $650 \div 700\,km/s$

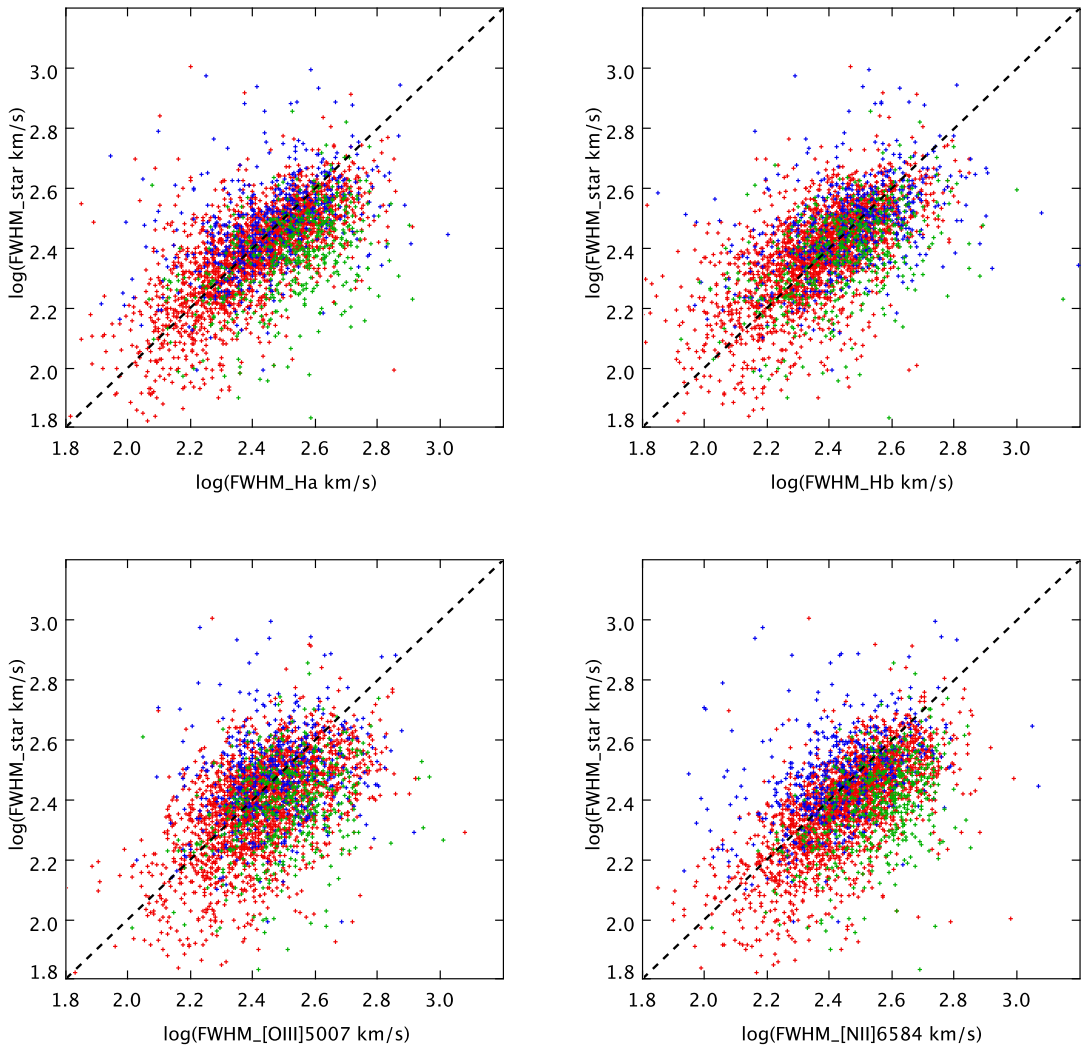

Figure 4.4: $FWHM_{star}$ vs $FWHM_{gas}$ for H_α (*top-left*), H_β (*top-right*), $[NII]6584$ (*bottom-right*), $[OIII]5007$ (*bottom-left*). The samples are indicated with the usual meaning of the colors.

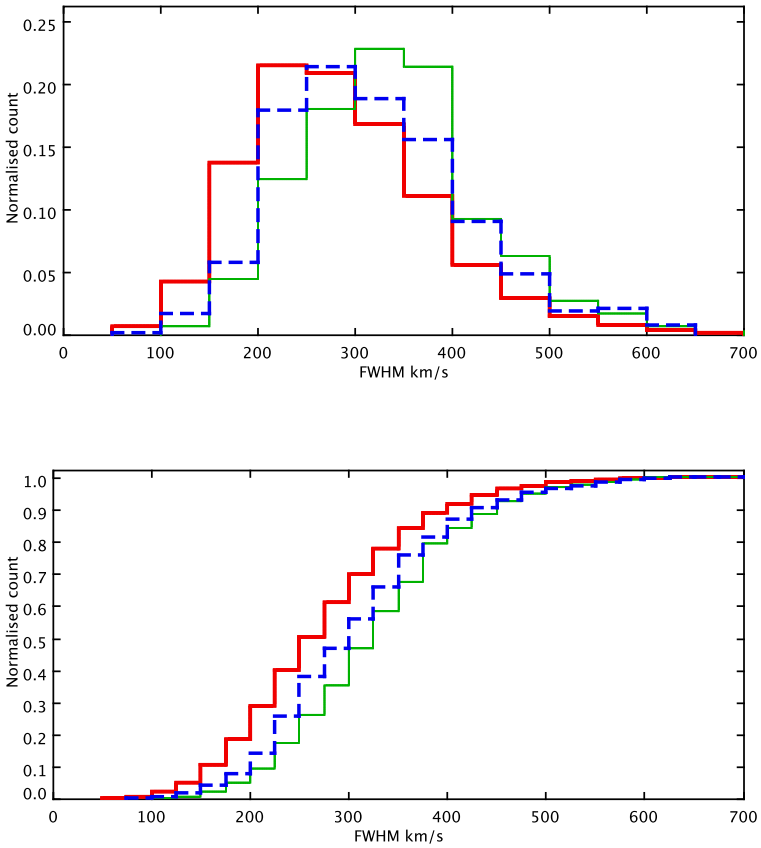

Figure 4.5: Mean $FWHM$ ($km\ s^{-1}$) distributions (*top*), and cumulative distributions (*bottom*). Lines and colors are as in Figure 4.1.

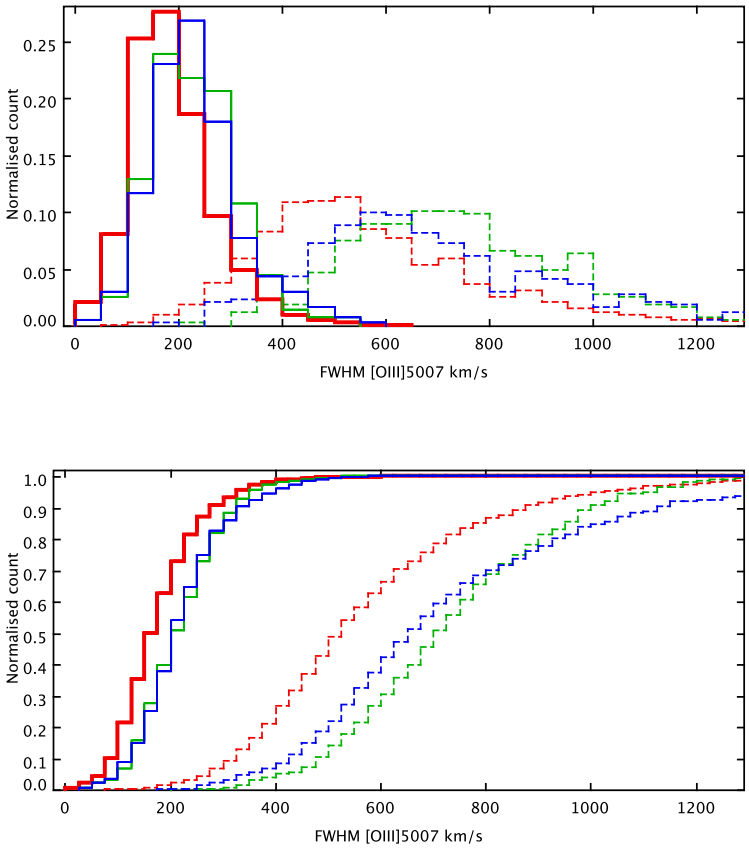

Figure 4.6: The $FWHM_{[OIII]5007}$ distributions (*top*) and $FWHM_{[OIII]5007}$ cumulative distributions (*bottom*) for the 1st component (*continuous line*) and 2nd component (*dashed line*).

for the other two samples. Between S2b and I-t the differences are not significant.

4.2.2 $[OIII]5007, 4959$ and H_β profile analysis

An accurate analysis of the line profiles, $[OIII]5007, 4959$ and H_β, was performed. We used the asymmetry parameter defined by Whittle (1985) and the line width at 10, 50 and 90 percent of the line height (Heckman et al., 1981), named respectively $FW10$, $FWHM$ and $FW90$. The asymmetry measure was obtained using the algorithm introduced by Whittle (1985) (the algorithm is explained in Appendix A of the same paper). Once the continuum level of the line is defined, the algorithm calculates the 10, 50 and 90 percent of the area and the corresponding wavelengths. Then two line widths named respectively $a = \lambda_{50} - \lambda_{10}$ and $b = \lambda_{90} - \lambda_{50}$ are defined, so the asymmetry is defined as $A = (a - b)/(a + b)$ (Figure 4.7). All these parameters are well described in Rice et al. (2006) and their figure 2.

These measures are based on the area, so they are less sensitive to the noise or effects of instrumental resolution. The major difficulty is the placement of the wing limits and the placement of the continuum; 9 different baselines were used and the obtained parameters come from the mean of these values. In order to define the line boundaries and the continuum we applied the same method described in §2.3. Once evaluated the line boundaries, we considered

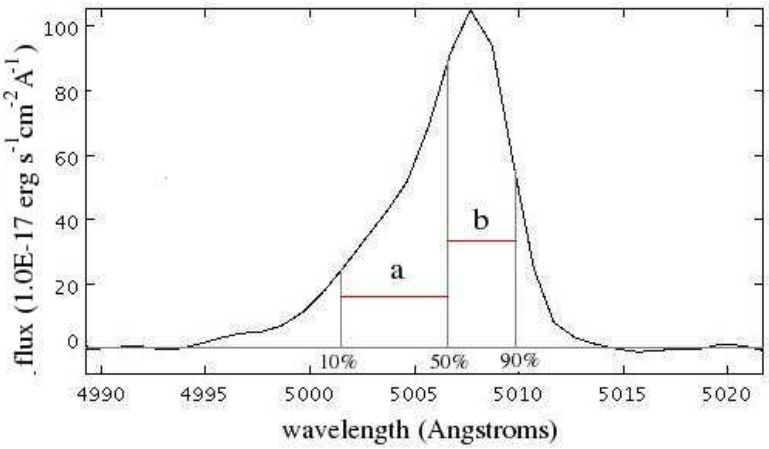

Figure 4.7: An example of $[OIII]5007$ line profile with indicated the Whittle's coefficients, the asymmetry A is defined by $A = (a-b)/(a+b)$. 10%, 50% and 90% markers indicate the percentage of the line area.

three pixels at each side of the line (the pixel corresponding to the line boundary and the adjacent ones) in order to define those 9 different baselines. A maximum limit of $\pm 1500\ km\ s^{-1}$ was imposed to prevent the non-convergence: in these cases the continuum value plus 2 or 3 times σ_c was taken into consideration, especially for $[OIII]4959$ and H_β, which have sometimes a lower S/N ratio.

The distributions of the measured asymmetries are presented in Figure 4.8. A clear indication of a positive asimmetry of the $[OIII]5007$ line with respect to H_β is found.

Of course the H_β distribution for the I-t sample is totally different because of the broad component, in any case all samples show the mean value around $A = 0$. In order to check the results the asymmetry analysis was done also for the $[OIII]4959$ line. There is agreement between $[OIII]4959$ and $[OIII]5007$ (Figure 4.9) although in this case the asymmetry measure is more difficult because $[OIII]4959$ is weaker. The correlation indices are 0.6 for the S2 and 0.7 for the other samples. On the contrary there is no correlation between $[OIII]\lambda 5007$ and H_β.

In order to measure $FW10$, $FWHM$ and $FW90$ we interpolated linearly the flux between the two pixels were the values were included. There is a good correspondence (the difference is $< 10\%$) with the measured $FWHM$ using a Gaussian fit. The central wavelength of $FW10$, $FWHM$ and $FW90$ were named respectively $pm3$, $pm2$ and $pm1$. An useful parameter is the difference between $pm1$ and $pm3$ (Figure 4.10): when this difference is positive the line profile shows a blue wing, otherwise a red wing. This alternative indicator of asymmetry gives results that are consistent with the parameter A defined above, except for the cases in which the wings are weak, below 20 percent of the hight of the line. The correlation index between the two parameters is ~ 0.85 for all three samples (Figure 4.11).

The asymmetry parameters were compared with the parameters coming from the multi-Gaussian fitting. To this purpose we defined the parameter pd as the difference between the peak wavelenght of the two components of $[OIII]5007$ (Figure 4.12). This parameter is in good agreement (Figure 4.13) with the Whittle's parameter. The correlation coefficient is about 0.75 for all the samples. A, $pm1 - pm3$ and pd are strongly connected.

In order to compare the amplitudes and the pd of the two components of $[OIII]5007$ with A, all the objects were plotted on to a 3D diagram, with pd on the x axis, the logarithm

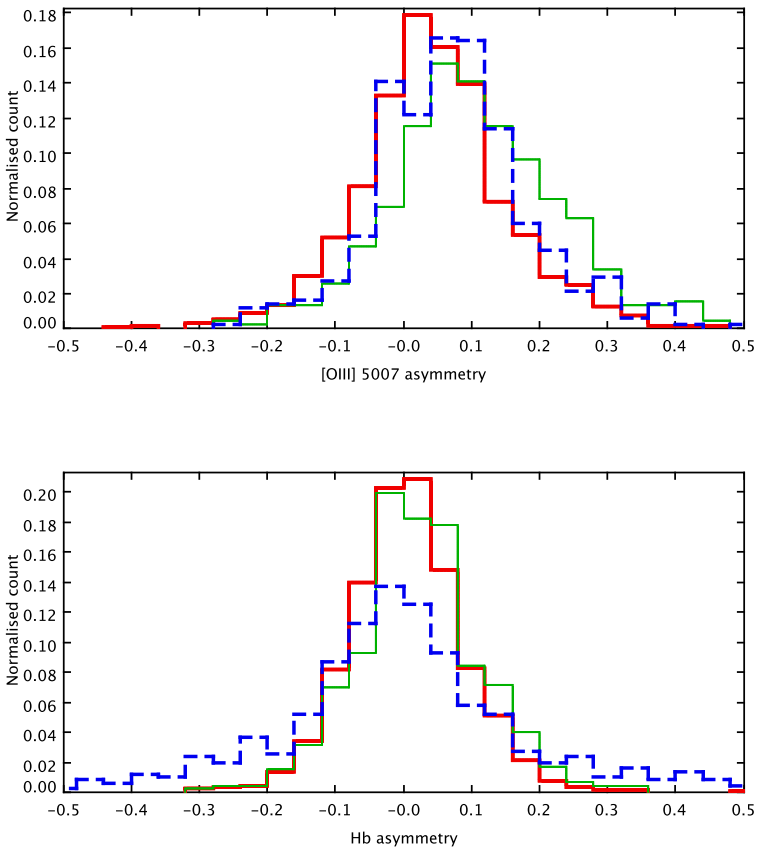

Figure 4.8: $[OIII]5007$ (*top*) and H_β (*bottom*) asymmetry distributions. Colors and line styles are as in Figure 4.1.

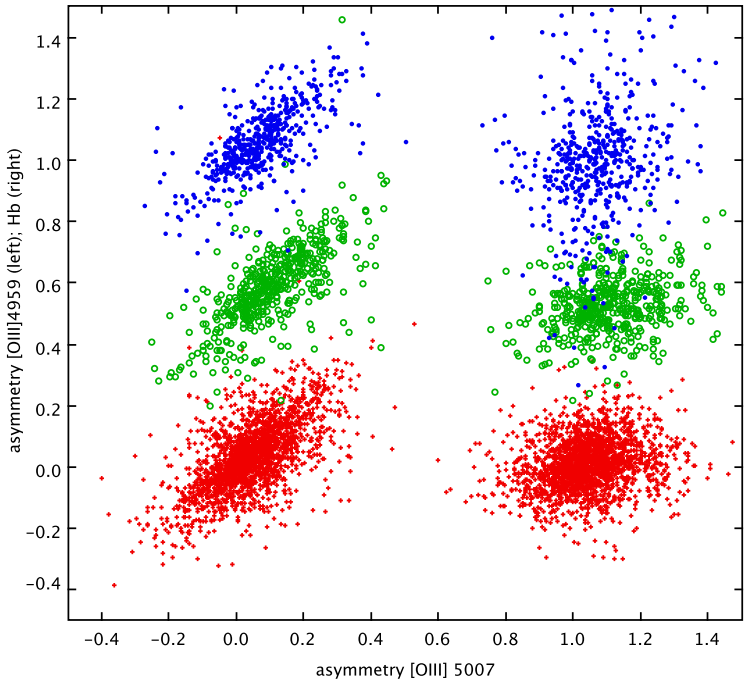

Figure 4.9: Asymmetry correlations, A_{4959} vs A_{5007} (*left*), A_{H_β} vs A_{5007} (*right, the shift is* 1 *unit*). the S2b and I-t are up shifted respectively of 0.5 and 1 units for visualization purposes.

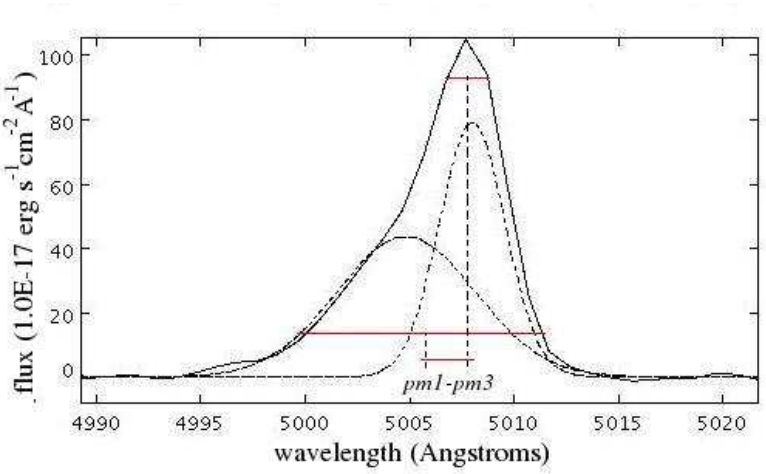

Figure 4.10: The asymmetry $pm1 - pm3$ parameter. $pm1$ is the $FW90$ mean value and $pm3$ is the $FW10$ mean value.

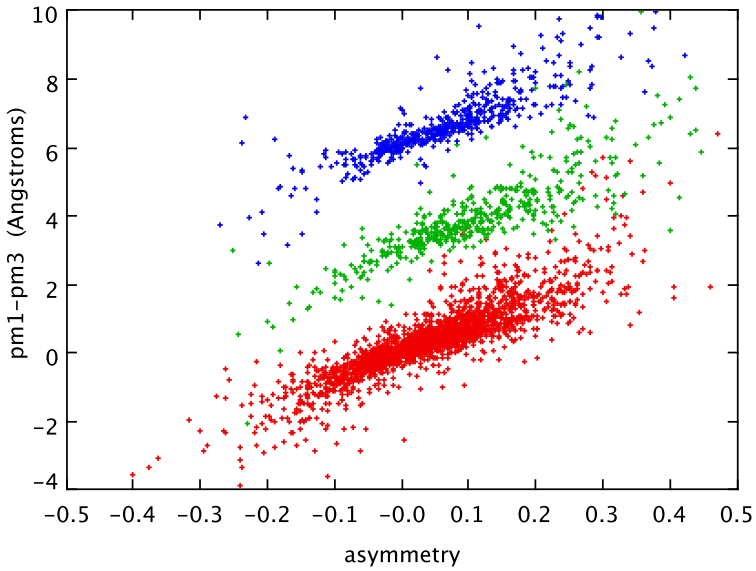

Figure 4.11: $[OIII]5007$ $pm1 - pm3$ index vs A. S2b and I-t are arbitrary shifted up respectively of 3 and 6 units.

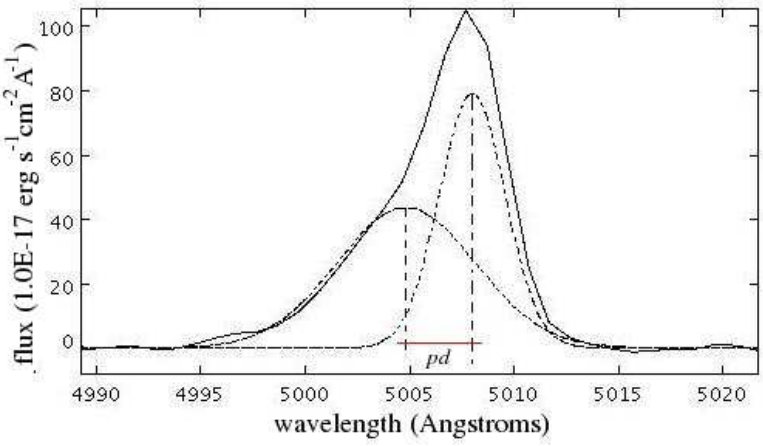

Figure 4.12: The asymmetry pd parameter. pd is the difference between the abscissa peaks of the 1st component (narrow component) and the 2nd component.

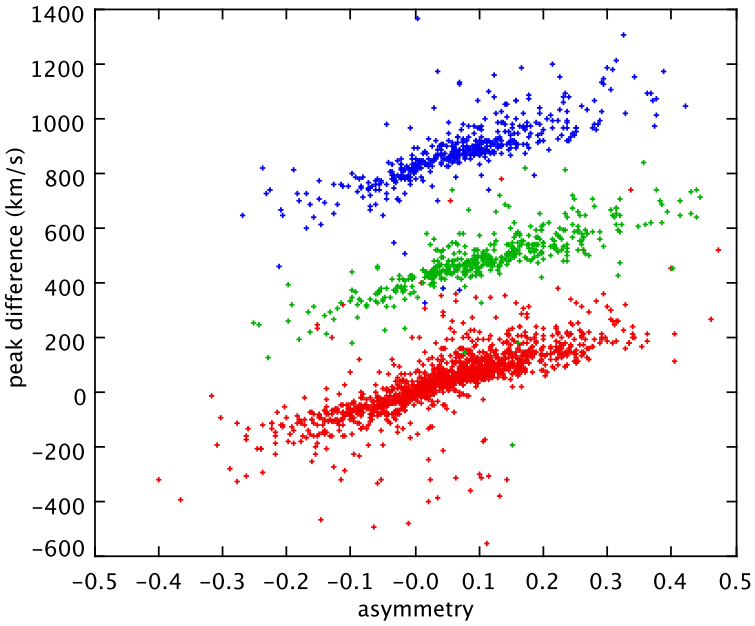

Figure 4.13: $[OIII]5007$ *pd* vs *A*. S2b and I-t are arbitrary shifted up respectively of 400 and 800 km/s.

of the amplitude ratio between the 1st and the 2nd component ($log\, h_1/h_2$) on the y axis, and Whittle's asymmetry parameter colour coded from blue to red for increasing asymmetry values (Figure 4.14). When the amplitudes ratio is higher than 10 or lower than 0.3, *A* is negligible, whereas the highest asymmetry values are found when the ratio is between 1 and 10.

The cumulative distributions of $A_{[OIII]5007}$, $pm1 - pm3$ difference and *pd* are shown in Figure 4.15. With a significance of 1% the S2b show a greater $A_{[OIII]5007}$ compared to the other samples, the difference from the I-t is smaller when the $pm1 - pm3$ and *pd* parameters are considered, whereas the S2 always show a lower asymmetry. All asymmetry parameters give high positive asymmetry (blue wings) for 68% of the S2, 84% of the S2b and about 73% of the I-t. This result supports the idea that when the asymmetries are present we are looking in the inner regions of the NLR where the kinematics is more complicated and chaotic, and presumably the gas is not simply moving in the gravitational potential but it is driven by winds and decelerating outflows (Wagner, 1997; Komossa et al., 2008). Finally it is important to note that there is no correlation between these asymmetry parameters and the luminosity, the FWHM of both components, and A_V.

In many cases we were able to determine the degree of ionization of the gas by measuring the ratio $[OIII]5007/H_\beta$ along the line profile. This measure allows us to investigate the different degree of ionization at different velocities. The wavelength scale of each line was transformed into velocity (km/s) then the lines were aligned and the ratio calculated pixel by pixel only if the H_β S/N ratio was greater than 10. Three different examples of this procedure are shown in the Figure 4.16. In agreement with Ozaki (2009) we found that the ratio $[OIII]5007/H_\beta$ increases with the velocity, i.e. that there is a correspondence between high ionization and high velocity. This result is reasonable and consistent with the previous

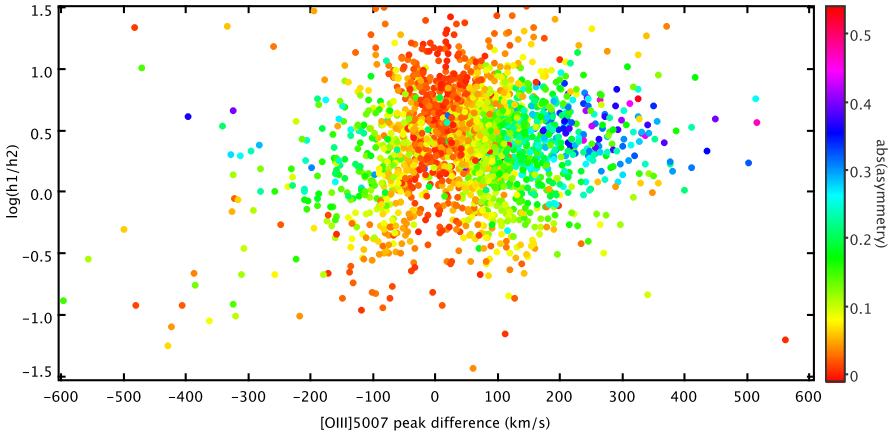

Figure 4.14: Logarithm of the amplitudes ratio ($h1/h2$) vs pd of $[OIII]5007$ components. The absolute Asymmetry values are indicated with a colour scale.

results about the asymmetry. Of course the I-t sample was excluded from this analysis because of the H_β broad component, that would imply a comparison between different regions. Maybe this problem could be present in S2b too, but if we assume that the broader component of $[OIII]5007$ belongs to the NLR like H_β, then the conclusion is correct. We show in Figure 4.17 all the calculated $[OIII]5007/H_\beta$ ratios along the profile for the S2 and S2b with an asymmetry coefficient greater than 0.2. We considered only spectra with high asymmetry because in these cases it is easier to detect a trend in the ratio. From figure 4.17 it appears clearly that the greater the velocity the greater the ionization level. Of course only a specific analysis of a individual spectra, such as the examples in figure 4.16, can show the trend and the peculiarities in the lines ratio.

4.3 Ionized gas mass, energy and accretion rate

Following the formalism reported in Osterbrock & Ferland (2006) it is possible to determine the ionized gas mass. The mass of the ionized emitting gas is given by

$$M = m_H \frac{\Omega}{4\pi} \int \varepsilon n_p dV \quad g \tag{4.2}$$

where m_H is the mean atomic mass (1 if the nebula is totally formed by hydrogen), $\frac{\Omega}{4\pi}$ is the covering factor, ε the filling factor and n_p the proton density. Assuming a uniform and spherical distribution of pure hydrogen emitting gas, the total gas mass is given by

$$M = \frac{4\pi}{3} r^3 n_p m_p \quad g \tag{4.3}$$

where m_p is the proton mass. Of course this is an over simplification but it provides us with the order of magnitude of the mass without requiring sophisticated models and high resolution observations. The H_β luminosity is given by

$$L(H_\beta) = h\nu_{H_\beta} \int n_p n_e \alpha^{eff}_{H_\beta}(H^0, T) dV \quad erg/s \tag{4.4}$$

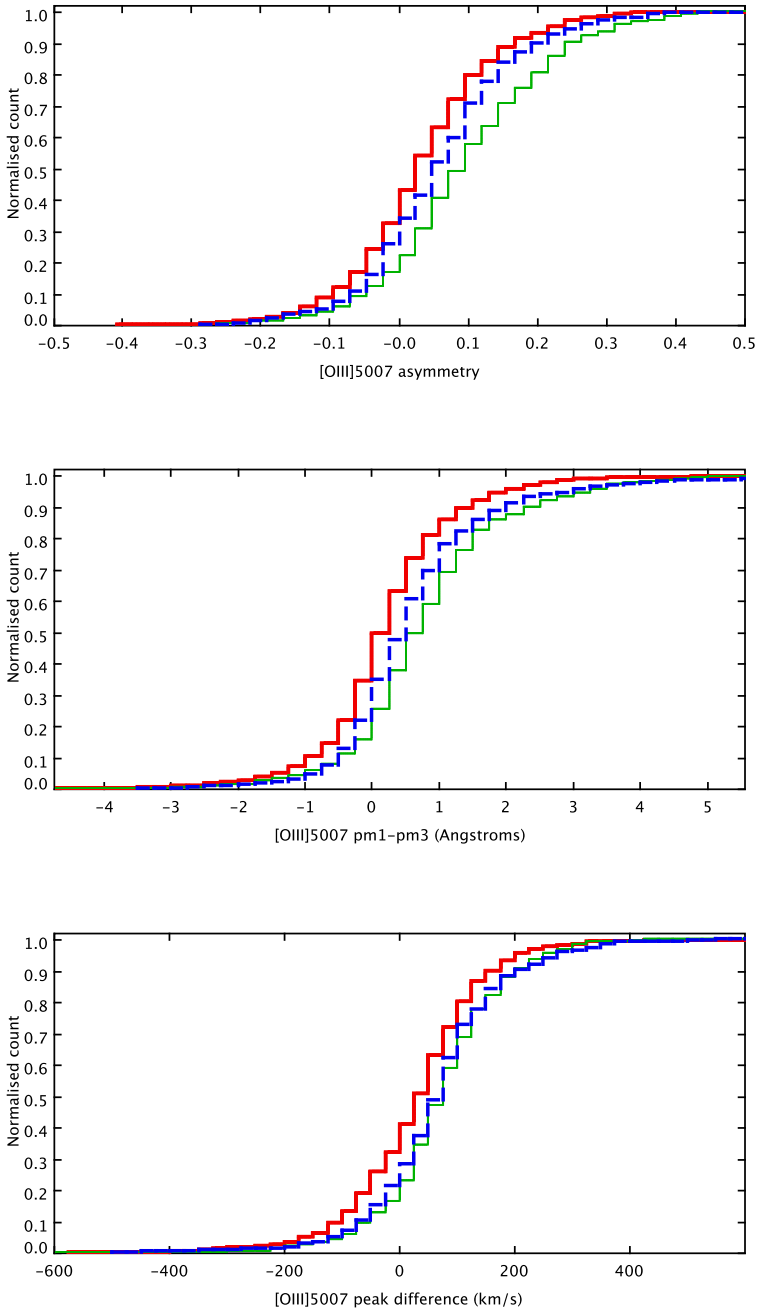

Figure 4.15: $[OIII]5007$ cumulative distributions of A, $pm1 - pm3$ and pd parameters. Only the S2 (*red line*) show a little significative difference with respect to the other samples. Colors and line styles are as in Figure 4.1.

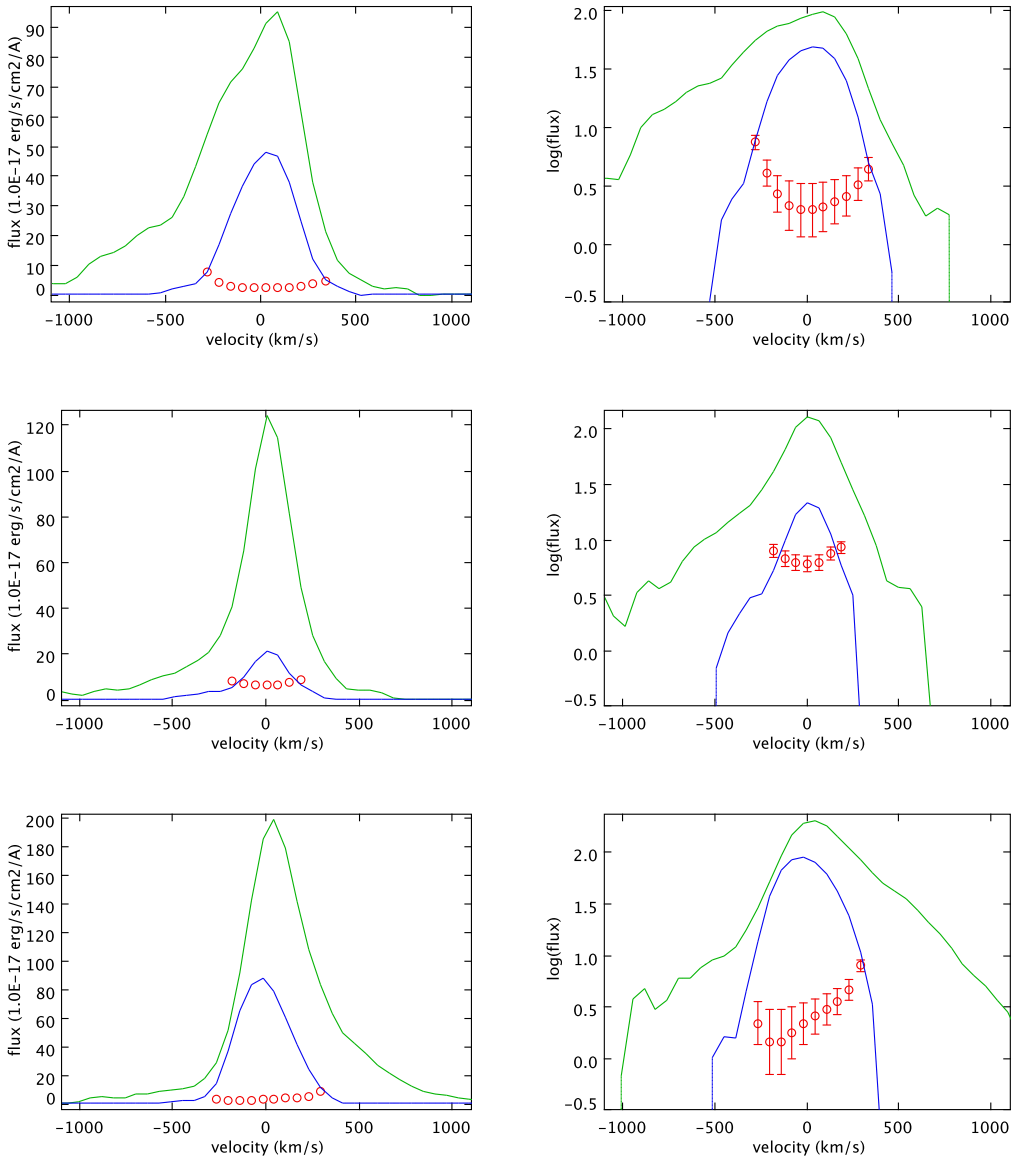

Figure 4.16: Three examples of $[OIII]5007/H_\beta$ ratio. *Left*, $[OIII]5007$ (*green*) and H_β (*blue*) line profiles and their ratio (*red circles*). *Right*, the same in logarithmic scale in order to show clearly the trend.

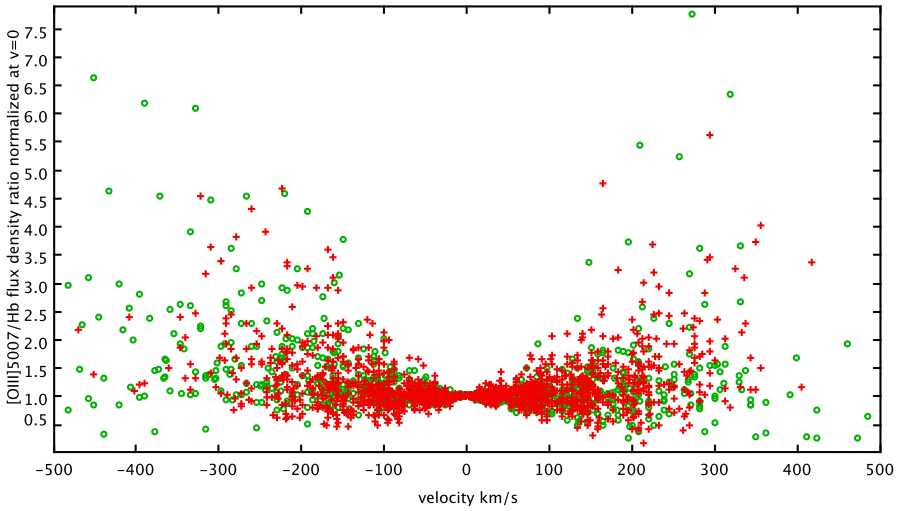

Figure 4.17: $[OIII]5007/H_\beta$ flux density ratios along the profile for the spectra with asymmetry coefficient larger than 0.2. S2 are indicated with *red crosses*, while S2b with *green circles*. The ratios are normalized to the value at $v = 0$.

where the n_p, n_e are the proton and electron densities, $\alpha^{eff}_{H_\beta}$ (H^0,T) the effective recombination coefficient and the integral is calculated over the entire ionized volume.

Applying the same hypothesis as above, we obtain

$$L(H_\beta) = \frac{4\pi}{3} r^3 h\nu_{H_\beta} n_p n_e \alpha^{eff}_{H_\beta}(H^0, T) \quad erg/s \tag{4.5}$$

then with the Equation 4.3

$$M = \frac{L(H_\beta) m_p}{h\nu_{H_\beta} n_e \alpha^{eff}_{H_\beta}(H^0, T)} \quad g \tag{4.6}$$

The effective recombination coefficient is given by

$$\alpha^{eff}_{H_\beta}(H^0, T) = 10^{-25} (h\nu_{H_\beta})^{-1} 1.387 t^{-0.983} 10^{-0.0424/t} \tag{4.7}$$

where $t = T_e/10000$ (Aller, 1984)

By assuming a temperature of 10000K and transforming in Solar masses, we obtain the final expression for the mass of ionized gas as a function of H_β luminosity:

$$M = 6.67 \cdot 10^{-33} \cdot \frac{L_{H_\beta}}{n_e} \quad M_\odot \tag{4.8}$$

By applying this formula to the S2 sample and assuming the densities obtained from the RS2 ratio we obtained a mass distribution having a median value of 10^6 $M_\odot$ and with 80% of the sample having a mass lower than 3.4×10^6 $M_\odot$. Deriving the NLR radius under the assumption of uniform distribution, we found a median value of $20\,pc$, with 80% of the sample under 40 pc. Of course these values are too low compared with the NLR radii. Even if a filling factor of 10^{-3} is assumed, the median radius is $200\,pc$ (the 80% of the sample has a radius lower than $400\,pc$), a more reasonable value but still rather low compared with

estimated values typically found in the literature (e.g. Bennert et al., 2006; Kraemer et al., 2009; Yonehara, 2006). From these results it appears that the RS2 densities are not really representative of the NLR density so its masses are probably underestimated. If a density of $10\,cm^{-3}$ is assumed, the mass median value is about $2.5 \times 10^7\,M_\odot$ while with a density of $1\,cm^{-3}$ the mass median value is one order of magnitude higher, $2.5 \times 10^8\,M_\odot$. In these two cases the radii median values are respectively 200 and 900 *pc*. Therefore, based on the implied size of the NLR, the most reasonable density value appears to be $\sim 1\,cm^{-3}$. Assuming that the clouds are self-gravitating and that the measured line widths are entirely due to motions governed by the gravitational potential, starting from a radius of 200pc, the virial mass ($M_{virial} = 5R\sigma^2/G$) is about three order of magnitude higher than that previously derived by Equation 4.8 with RS2 density, and one order of magnitude lower than the mass calculated with the lowest density ($1\,cm^{-3}$) (Table 4.3). Of course we do not expect that the whole gas could be virialized but this value, which is an upper limit, suggests the possibility of a large neutral fraction of gas. Alternatively it is possible to determine the gas mass from the measure of the reddening and from a given dust-to-gas ratio (Fu & Stockton, 2007). Assuming the Galactic dust-to-gas ratio we obtain

$$M = 5.28 \cdot 10^{21} cm^{-2} mag^{-1} E_{B-V} m_p \Omega d_A^2 \tag{4.9}$$

Where Ω is the solid angle subtended by the NLR, d_A the angular distance. Unfortunately it is not straightforward to apply this formula in our case. The fiber diameter is not useful and it is not possible to get Ω from observational measures. In principle one can assume fixed dimensions of the NLR, but this is not a good idea because the typical NLR radius varies in a wide range (100 to 1000 *pc* or more). Nevertheless if we determine the NLR mass from Equation 4.8, Equation 4.9 is useful to estimate the NLR dimensions. In fact by combining these equations we can express Ωd_A^2 as a function of measurable quantities. This gives us the projected NLR surface and then the NLR radius

$$R = \sqrt{\frac{M}{8.6 \cdot 10^{-3} A_V}} \quad pc \tag{4.10}$$

Table 4.3 contains the radius distributions obtained with the three calculated mass median values. In order to obtain the same radius distribution with both the approaches (equation 4.8 and 4.10) and with $10^6\,M_\odot$ we have to impose a filling factor of $\sim 0.01 \div 0.001$ when the classical approach is used. If low densities are adopted the radii obtained with the equation 4.10 are consistent with the values measured in the NLR and EELR.

As already pointed out by Fu & Stockton (2006), and in agreement with what we said above, we can reasonably assume that most of the emitting volume of the NLR is dominated by a massive and highly ionized diffuse medium at very low density ($\sim 10\,cm^{-3}$), containing clouds and filaments at lower ionization and density of $\sim 100 - 500\,cm^{-3}$ distributed in the external regions, and likely clouds at higher density ($\sim 10^3 - 10^5\,cm^{-3}$) located in the inner part of the NLR, where the ionization is expected to be stronger. This hypothesis is supported by the missing $[ArIV]$ doublet too: these lines are rare and probably are switched off by high densities in the inner regions where the $[OIII]$4363 is visible. Otherwise the low ionization lines with high critical density are weaker because in the external regions, where the ionization is low and these lines would be favoured, the density is very low.

Our aim is to compare masses, energies and accretion rates between the three different samples, in order to do that we assume a density of $10\,cm^{-3}$. Of course this choice is

Table 4.3: NLR mass and radius distributions for three different N_e.

$N_e\, cm^{-3}$	M ($M_\odot$)	mean (pc)	mode (pc)	median (pc)	$< 80\%$ (pc)
$RS2$	10^6	170	100	140	240
10	$2.5 \cdot 10^7$	750	580	680	950
1	$2.5 \cdot 10^8$	2400	1900	2200	3000

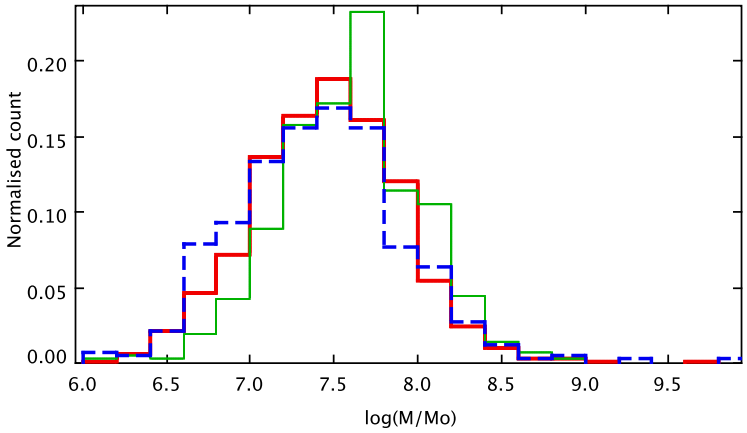

Figure 4.18: Ionized gas mass obtained by Equation 4.8 with $N_e = 10\, cm^{-3}$. The different colors and line styles represent the samples: S2 (*red line*), S2b (*green thin line*) and I-t (*blue dashed line*).

absolutely arbitrary, even if reasonable, and useful to give the order of magnitudes of these physical parameters.

The distribution of the ionized gas masses for the three classes of objects is shown in Figure 4.18. The median value is about $3 \times 10^7\, M_\odot$, and the 90% of the sample has a mass lower than $10^8\, M_\odot$. The S2b show a significative difference with higher values compared to the other samples, but this could be due to an overestimation of the H_β luminosity if a broad component was present (see §2.4).

It is interesting to note that the ionized gas mass is one order of magnitude lower than that of the EELR of the quasar 4C 37.43 (Fu & Stockton, 2007), using the same density, and this conclusion is extended to a large sample of NLR. In any case the quantity of involved mass is lower compared to the quasars.

With the ionized gas mass it is possible to determine the kinetic energy due to the turbulence, thermal and bulk motion. The determination of the third one would require detailed velocity fields that are not available at the spectral resolution of our sample. We could only use the asymmetric components (broader components) found in the $[OIII]5007$ line to derive the order of magnitude of the kinetic energy due to bulk motion. These energies are determined using the formalism introduced by Fu & Stockton (2007). The turbulent energy can be estimated from the measured velocity dispersion σ_{H_β},

$$E_{tur} = M\sigma^2 = 5.0 \cdot 10^{56} M_{10} \sigma_{50}^2 \quad erg \tag{4.11}$$

where $\sigma_{50} = \sigma_{H_\beta}/50\, km/s$ and M_{10} the mass expressed in 10^{10} solar masses.

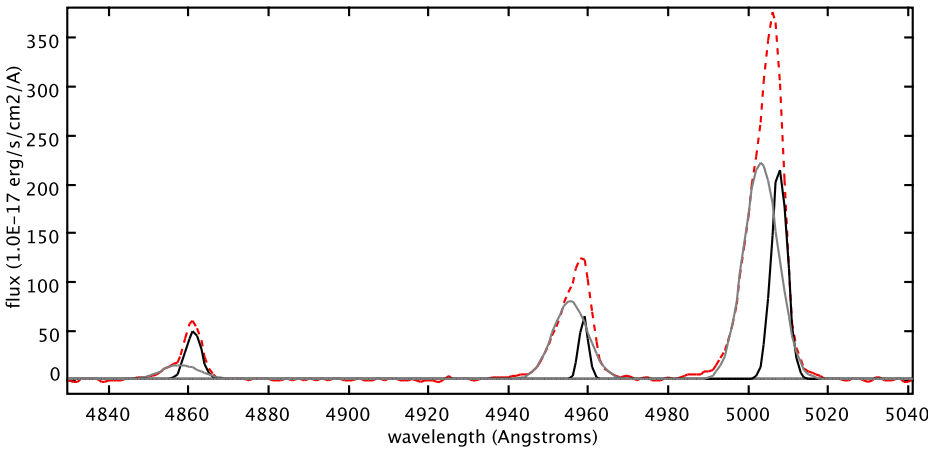

Figure 4.19: An example of double components system, the original spectrum (*red*), the narrow component (*black*) and the 2nd component (*grey*).

The thermal energy is

$$E_{th} = \frac{3}{2} MkT/m_p = 2.5 \cdot 10^{55} M_{10} T_4 \quad erg \tag{4.12}$$

where $T_4 = T/10000K$
The bulk kinetic energy is given by

$$E_{bulk} = \frac{1}{2} MV^2 = 6.2 \cdot 10^{57} M_{10} V_{250}^2 \quad erg \tag{4.13}$$

where V_{250} is the bulk velocity in $V/250 kms^{-1}$ units. The bulk velocity is estimated from the difference in the peak velocities of the $[OIII]5007$ components, the narrow component is assumed to have the systemic velocity (Figure 4.19).

Thermal and turbulent energy distributions are plotted in Figure 4.20. The values are calculated using the masses derived from a fixed density of $10\,cm^{-3}$. The distributions are similar for S2 and I-t with a logarithmic median value around 52.7 and 54.7 respectively for the thermal and turbulent energy. S2b show higher values (53 and 55) which are a direct consequence of the mass distribution.

The thermal energy is negligible compared to the turbulent energy.

In order to derive the bulk kinetic energy it is fundamental to obtain the $[OIII]5007/H_\beta$ ratio of the 2nd component if we want to apply Equation 4.8 to derive the involved mass. Unfortunately, the S/N_{H_β} and the spectral resolution do not permit to achieve this result but if we consider all the objects, S2 and S2b, which show two components in $[OIII]5007$ and H_β (89 spectra) and plot the H_β *pd* vs $[OIII]5007$ *pd*, it appears that the spectra with a similar *pd* parameter (45 spectra) have a flux ratio of the 2nd component around 10 (Figure 4.21), the median is 8, the mode 10 and the mean 7, which is consistent with the assumption of Fu & Stockton (2006) and with the measures of Cid Fernandes et al. (2001). The correlation coefficient of all 89 spectra is 0.8 but it becomes 0.9 when the 45 objects are considered. 31 and 33 spectra show respectively $[OIII]4363$ and $[FeVII]6087$ lines. Then, assuming 10 as indicative value of the $[OIII]5007/H_\beta$ ratio, from the luminosity

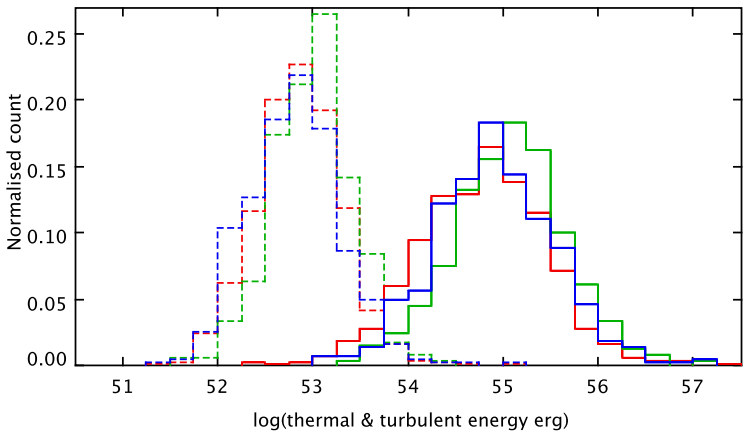

Figure 4.20: Thermal (*thin dashed lines*) and turbulent (*thick lines*) energy distributions. Colors are as in Figure 4.18.

of $[OIII]5007$ broader component and from the velocity peak difference, we derive the bulk kinetic energy by applying Equation 4.13. The mass was calculated under the low density assumption $N_e = 10\,cm^{-3}$. The median logarithmic values are respectively around 6.8 for S2 and I-t, and 7.1 for S2b. Hence the masses involved in the bulk motions are about 1/3 of the total mass. If the bulk motions are connected to outflows and we assume a typical dynamical time scale of $10^7\,yr$ (see below), the resulting rate of mass outflow $\sim 1 M_\odot\,yr^{-1}$

With the masses is now possible to find the bulk kinetic energy. The logarithm of median bulk kinetic energy values is around $53.5 - 54$. The distributions (Figure 4.23) show that the 80% of the samples have a bulk energy lower than 54.5. The bulk kinetic energy is approximately lower than one order of magnitude compared with the turbulent energy.

Now we consider the possibility that the outflow is directly driven by the black hole (BH). Radiation from the accretion disk can couple to the surrounding gas via various processes, such as electric scattering and photo-ionization. The input momentum rate from radiation pressure is given by (Fu & Stockton, 2006)

$$\dot{p} = 1.3 \cdot 10^{35} (\eta/0.1) \dot{M}_{acc} \quad dyn \tag{4.14}$$

where η is the radiative efficiency and $\dot{M}_{acc}$ is the mass accretion rate of the BH in units of $M_\odot\,yr^{-1}$. An estimate of the momentum rate is given by

$$\dot{p} \sim M \cdot V_{bulk}/t_{dyn} \quad dyn \tag{4.15}$$

where M is the moving bulk mass and t_{dyn} the dynamical time scale.
From the NLR radius it is possible to estimate the t_{dyn}

$$t_{dyn} \sim R_{NLR}/V_{bulk} \quad s \tag{4.16}$$

The NLR radius distributions for the three samples is shown in Figure 4.24. It is interesting to note that the K-S test gives the same distribution for S2b and the I-t samples, with a median value of 850 pc. The S2 have a median of 680 pc, within 1% of significance the NLR radii are lower.

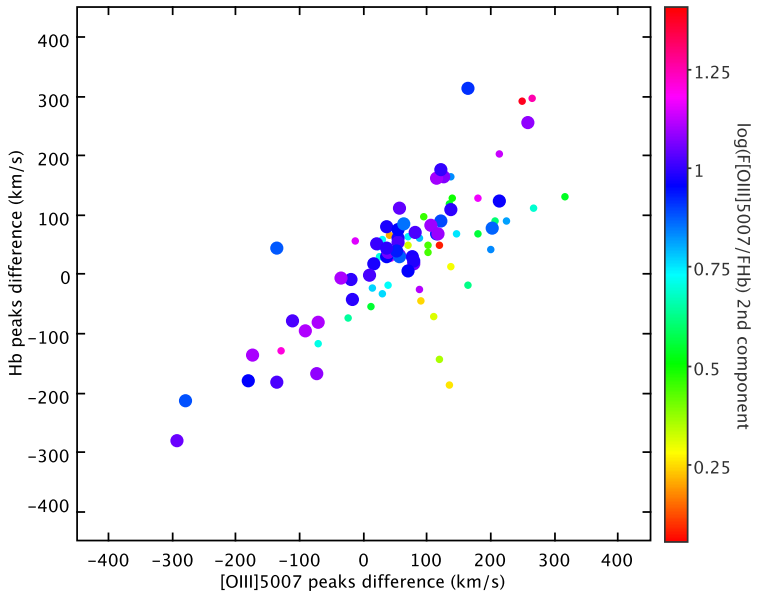

Figure 4.21: H_β vs $[OIII]5007$ *pd* for the spectra with 2 components in both the lines. The big circles have a $F_{[OIII]5007}/F_{H_\beta}$ of the 2nd component between 7 and 13.

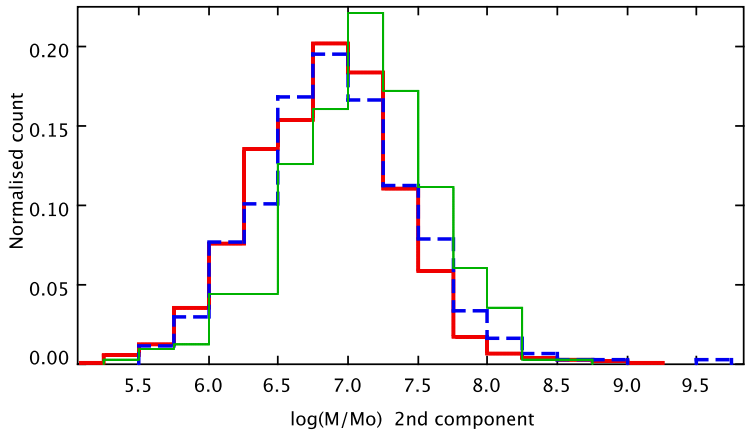

Figure 4.22: Ionized gas mass obtained by 2nd $[OIII]5007$ component assuming a $F_{[OIII]5007}/F_{H_\beta} = 10$. Lines and colors are as in Figure 4.18.

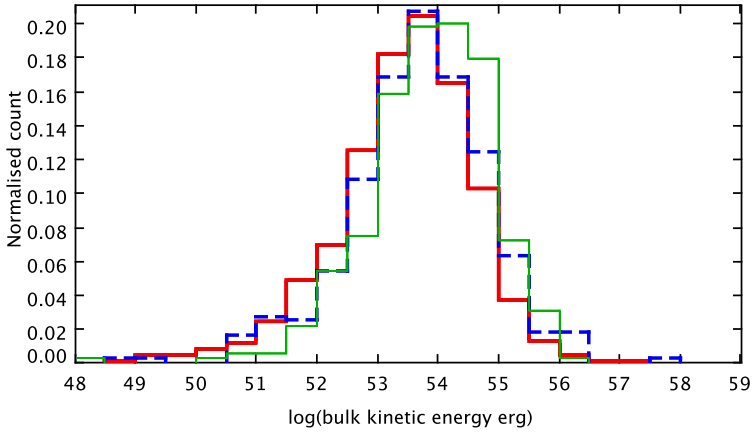

Figure 4.23: Kinetic bulk energy distributions. Lines and colors are as in Figure 4.18.

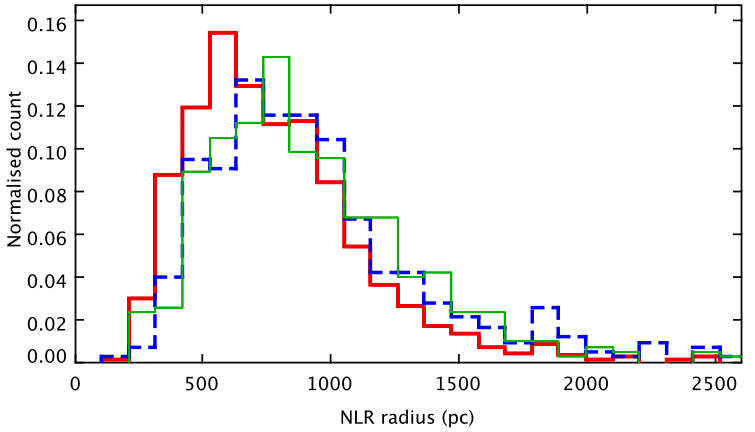

Figure 4.24: NLRs radius distributions. Lines and colors are as in Figure 4.18.

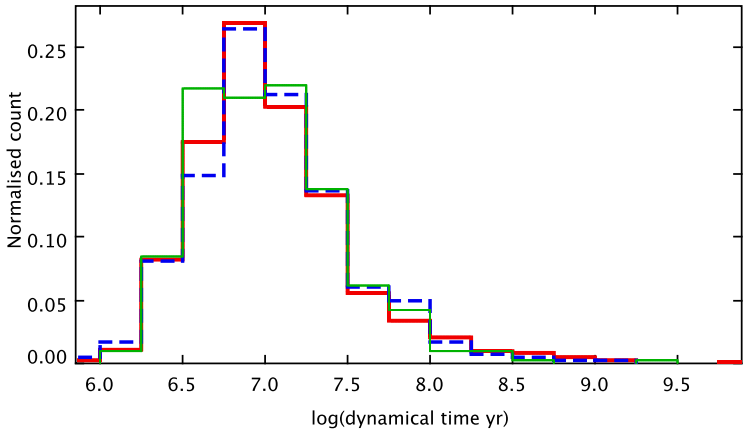

Figure 4.25: Dynamical time scale distributions. Lines and colors are as in Figure 4.18.

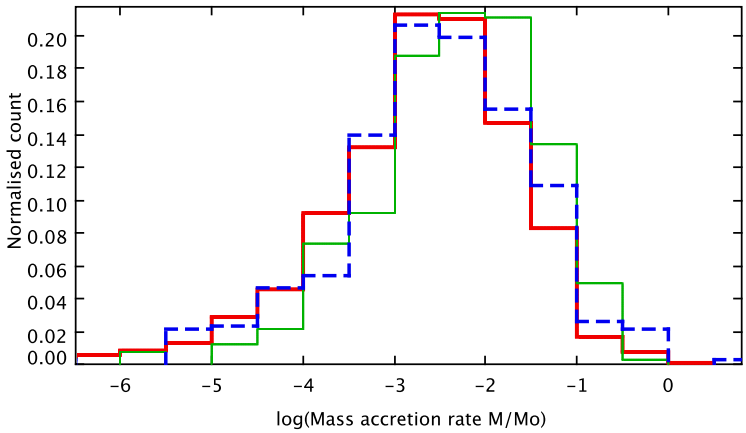

Figure 4.26: Mass accretion rate distributions. Lines and colors are as in Figure 4.18.

All the samples have the same t_{dyn} distributions (Figure 4.25), the median value is $10^7\,yr$, 80% of the samples have $t_{dyn} < 3 \times 10^7\,yr$ (the mean AGN lifetime is $\sim 10^7 \div 10^8\,yr$).

Then assuming $\eta \sim 0.1$, from equations 4.14 and 4.15 we obtain an estimate of the $\dot{M}_{acc}$ distribution. The median value is around $0.003\,M_\odot\,yr^{-1}$, 80% of the samples have $\dot{M}_{acc} < 0.03\,M_\odot\,yr^{-1}$. These are lower limits because most of the mass responsible for the bulk motion may not be detectable in the optical and a substantial amount of this may be shielded from the ionizing flux (Veilleux et al., 2005).

Chapter 5

Photo-ionization models

5.1 Overview

Many processes are involved in the ionized gas emitting region and building a model able to reproduce the observed spectrum is a big challenge. Following Netzer (2008), there are five fundamental issues in the ionized gas physical processes: photo-ionization and radiative recombination, thermal balance, ionizing spectrum, gas chemical composition and clouds and/or filaments distribution. Of course each argument involves many other processes and aspects. In particular the first one involves dielectronic recombination, Auger ionization, heating and ionization by secondary electrons, charge exchange, collisional ionization and three body recombination and Compton ionization (heating and cooling). In the thermal balance an important role is played by the mechanical heating and the dust, which is always present in the NLR. In addition the gas kinematics, winds and gas confinement must be taken into account. Photoionization codes are generally used to solve numerically the ionization and thermal structure of single gas clouds. In this work we use the code CLOUDY (version 06.02, Ferland et al., 1998) as a subroutine in order to explore different parameter values and to build more sophisticated models such as composite multiple cloud models. CLOUDY works with two default geometries: open and close geometry. The first one considers a simple photo-ionization field through a plane parallel slab with a defined ionized column density; in the second case the gas is spherically distributed all around the source. In this work we assume an open geometry for all models. The ionizing spectrum was assumed to have a power-law slope with the following characteristics: $F_\nu \sim \nu^\alpha$ in the range 10 $\mu\,m$ - 50 keV, with a cut-off at low energies, $F_\nu \sim \nu^{5/2}$, and a cut-off at high energies, $F_\nu \sim \nu^{-2}$. This choice is in agreement with Komossa & Schulz (1997), Groves et al. (2004), and supported by X-rays observations (Mainieri et al., 2007). The input parameters are the spectral index α, the electron density Ne (cm^{-3}), the ionized column density $Nc(H^+)$ (cm^{-2}), the ionization parameter U, and the chemical abundances $Z/Z_\odot$. The ionization parameter gives the level of ionization of photo-ionized gas and is proportional to the ratio of the ionizing photon density to the gas density:

$$U = \frac{Q_{ion}}{4\pi r^2 c N_H} \tag{5.1}$$

where c, the speed of light, is introduced to make U dimensionless.

We built two kinds of photo-ionization models: single cloud models and composite models. The second one is based on a combination of two different models. In literature we found two fundamental approaches about composite models: a dense cloud inside a medium with

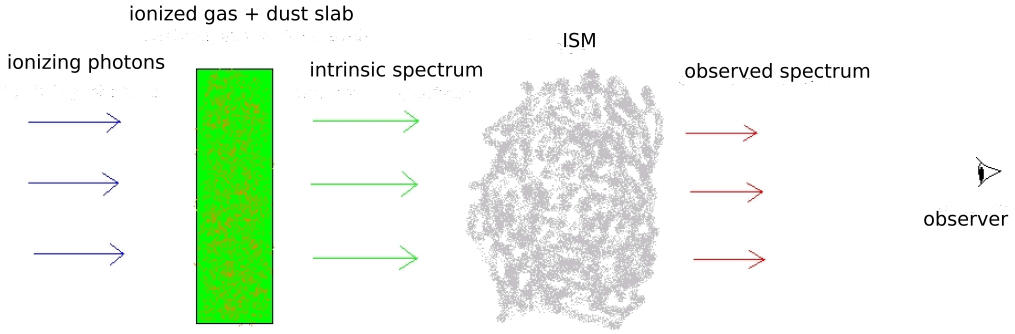

Figure 5.1: The basic model.

lower density, as made by Binette et al. (1996), or a combination of two individual clouds, as made by Komossa & Schulz (1997). More specific and sophisticated models would require additional information about the objects, for example radio, IR and UV observations, high resolution images, etc. This is not our case and building grids of models seems the only realistic way to compare a great number of observed spectra to the models.

5.2 Single cloud models

In order to explore the 5 parameters we built a set of single cloud models with the parameter values reported in Table 5.1.

The base model is summarized in Figure 5.1, the ionizing photons are intercepted by a slab of gas and dust with fixed density, column density and dust to gas ratio, independently from the source distance, because the ionization parameter is also fixed. The slab density is assumed to be constant and the temperature values are calculated by CLOUDY for each layer, so these models are not isobaric. The calculation is stopped either when the transmitted fraction of ionizing photons is lower than 1% or when a temperature of $4000K$ is reached. The cloud dynamical stability is not controlled but the hydrogen recombination and thermal time-scales (T_H, T_{th}) are consistent with the cloud survival time (τ), $\tau \ll T_{H/th}$. These assumptions are made with the aim to combine different clouds with different densities and ionization parameters. The intrinsic spectrum is calculated by CLOUDY after the fixed column density is reached or the temperature has gone below 4000K (default mode). Then we assumed the intrinsic spectrum is reddened by the ISM. So when the models will be compared to the observed spectra they must be reddened.

5.2.1 Chemical abundances set

The metallicity in HII regions and in star-forming galaxies may be determined through direct methods (Aller, 1984), measuring the line flux ratios once the temperature is known, or through empirical, but well calibrated, metallicity indicators (Pilyugin & Thuan, 2005) when it is not possible to measure directly the abundances like in high metallicity or low excitation cases. Anyway in the stellar photo-ionization case the ionization structure is known and it is possible to obtain the total abundances once the ionic abundances are measured by applying ionization correction factors (Mathis & Rosa, 1991, and references therein). In the AGN case the situation is more complicated because when the ionizing spectrum is a non-thermal power-

Table 5.1: Input parameter values

$Z(Z\odot)$	α	$log(U)$	$log(N_e\ cm^{-3})$	$log(N_c(H+)\ cm^{-2})$
0.5	-2.2	-3.6	1	19
1	-1.9	-3.2	1.5	19.4
1.5	-1.6	-2.8	2	19.8
2	-1.3	-2.4	2.5	20.2
2.5	-1	-2	3	20.6
3		-1.6	3.5	21
3.5			4	21.4
				21.8
				22.2

law the ionization structure is very complex. The partially ionized zone is very extended, therefore different ionization states are mixed together making it difficult to account for all ionic abundances in order to determine the total abundances. Direct methods do not exist and the only way to determine the chemical abundances is to use photo-ionization models.

Once a reference abundances set is assumed, usually the solar set, we need a prescription to change the chemical composition in order to explore different metallicities while taking into account the interdependence of the abundances of individual elements in chemical evolution. The analysis of the ionized gas chemical abundances in HII and star-burst galaxies shows that the element abundances maintain the same proportions except for Nitrogen and helium. Since Oxygen is the most abundant element after hydrogen and helium and three different ionization states of Oxygen are observable in the optical spectrum, the metallicity is usually expressed in terms of Oxygen abundance. We can assume that all elements scale directly with the Oxygen abundance ($log(X/O) = constant$), but Nitrogen and helium must be treated separately. The Nitrogen abundance must be corrected for secondary production (Vila Costas & Edmunds, 1993) and for helium the yield must be added to the primordial abundance. In this work we use the relations introduced by Groves et al. (2004, 2006) with the requirement of matching the adopted solar abundance patterns:

$$\frac{N}{H} = \frac{O}{H}[10^{-1.6} + 10^{2.37+log(O/H)}]. \tag{5.2}$$

$$\frac{He}{H} = 0.0737 + 0.0293\frac{Z}{Z_\odot} \tag{5.3}$$

The abundances set has to keep into account both gas and dust composition in order to conserve the total assumed element abundances:

$$(X/H)_{tot} = (X/H)_{gas} + (X/H)_{dust} \tag{5.4}$$

where (X/H) is the abundances ratio between element X and hydrogen.

The quantity of the element X depleted into dust ($(X/H)_{dust}$) is expressed by the *depletion factor* (hereafter $depl(X)$) defined as

$$depl(X) = log(X/H)_{gas} - log(X/H)_{tot} \tag{5.5}$$

An increase in the metallicity implies an increment of refractory elements and hence, supposedly, also an increase in dust amount.

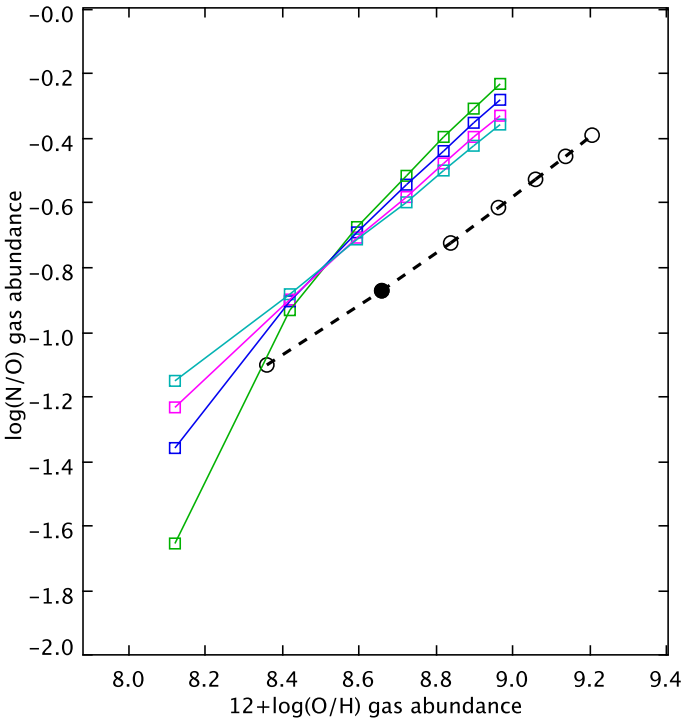

Figure 5.2: log(N/O) vs 12+log(O/H). The *coloured lines* show $log(N/O)$ vs $12 + log(O/H)$ for the gas phase for different D/G values: 1.00 (*pale blue*), 0.75 (*cyan*), 0.50 (*blue*), 0.25 (*green*). The squares in each sequence are the seven $Z/Z_{\odot}$ adopted values, increasing from left. *Black dashed line* shows the trend obtained with the total abundances, *black circles* show the adopted metallicity values $Z/Z_{\odot}$, respectively 0.5, 1 (*filled circle*), 1.5, 2, 2.5, 3, 3.5.

The dust treatment is made difficult by the uncertainties in $(X/H)_{dust}$ (dust-to-gas ratio for the element X) and the grains composition. The depletion into grains appears to be constant in many directions of the Galaxy (Vladilo, 2002) therefore the dust composition of the Galactic ISM should be a good reference.

If the $depl(X)$ is constant the $(X/H)_{dust}$ increases linearly with the metallicity, otherwise if the $(X/H)_{dust}$ changes with the metallicity the $depl(X)$ is subject to a variation (Binette et al., 1993).

As reference we adopted the solar abundances by Asplund et al. (2005) and the depletion factors reported in Groves et al. (2006). Combining Equations 5.4 and 5.5 we can find the $(X/H)_{dust}$ and $(X/H)_{gas}$ sets for the solar abundances (Table 5.2). Therefore, assuming the depletion factors constant, the dust abundance scales linearly with the metallicity with the exception of Nitrogen.

We built 4 different sets of models multiplying the previously calculated $(X/H)_{dust}$ abundances set for 0.25, 0.50, 0.75 and 1.00 respectively, the corresponding sets of depletion factors were recalculated to insure the conservation of the total abundances (Table 5.2). Since the $(X/H)_{dust}$ is the dust-to-gas ratio for the element X, the model sets are indicated with: $D/G = 0.25$, $D/G = 0.50$, $D/G = 0.75$, $D/G = 1.00$.

For each D/G value we defined seven sets of chemical abundances, using the solar Oxygen abundance as reference: $Z = 0.5$; 1; 1.5; 2; 2.5; 3; 3.5 $Z_{\odot}$.

We concentrated our attention on the high metallicity regime because we are working with the nuclear gas and Seyfert galaxies, where sub-solar metallicities are very rare (Groves et al., 2006). The depletion factors set is constant for each D/G assumed with the exception of Nitrogen because of the secondary production. The Nitrogen depletion factor must change with the metallicity because, coherently with our assumptions, if the dust increases with the metallicity there must be an excess of Nitrogen in gas form due to the relation 5.2. In fact Nitrogen may be depleted in the carbonaceous grains, the involved functional groups are Amines (N-H, C-N), Amides (N-H), Nitriles (C,N triple bond stretch), Isocyanates (-N=C=O), Isothiocyanates (-N=C=S), Imines (R2C=N-R) and Nitro groups (-NO2 aliphatic, aromatic) (Kwok, 2007). Excluding the ammonia (NH_3), which cannot survive in presence of an intense ionizing field such as in AGN, all the mentioned compounds need partner elements which increase linearly with the metallicity. The depletion factors for D/G=1 are given in Table 5.3. If the assumption about the dependence of Nitrogen depletion on metallicity is correct we have a large increment of Nitrogen gas abundance above 1.5 $Z_{\odot}$, hence it is not necessary to invoke an excess of Nitrogen in order to reach the observed $[NII]\lambda6584$ line intensity. Figure 5.2 shows the relations between $log(N/O)_{gas}$ and $12+log(O/H)_{gas}$ for each D/G and for each $Z/Z_{\odot}$ adopted value. For the other elements the trend is constant once the D/G value is assumed. It is important to note that the depletion of the elements must be taken into account even if the nebula is without dust, such as in radiation-pressure dominated models of Groves et al. (2004) where the dust is pushed up by the wind. In our models we assumed only two types of dust, graphite and silicates, the reference abundances when D/G= 1 are $[C/H] = 1.22E-04$ in graphite and $[O/H] = 1.94E-04$, $[Mg/H] = 3.15E-05$, $[Si/H] = 2.82E-05$, $[Fe/H] = 2.70E-05$ in silicate; the size distribution of the grains is in the range $[0.005, 0.25]$ μm. The grains are the default interstellar medium grains (Martin & Rouleau, 1991).

We analysed the abundances found in many HII regions with direct methods in order to check the trend between Oxygen abundance and the other elements, overall Nitrogen. In van Zee et al. (1998), van Zee & Haynes (2006), Izotov & Thuan (1999), Izotov et al. (2006), Contini et al. (2002) we can find a large collection of chemical abundances determinations respectively in 186 HII regions spanning a range of radii in 13 spiral galaxies, 54 super-giant H II regions in 50 low-metallicity blue compact galaxies, 67 HII regions in 21 dwarf irregular galaxies, 310 emission-line galaxies from SDSS Data Release 3 and a sample of 68 UV-selected intermediate-redshift ($0 \leq z \leq 0.4$) galaxies. The Oxygen and Nitrogen total abundances from this literature collection are reported in Figure 5.3 toghether with the N/O function adopted in our models for the seven metallicity values. Our values do not match very well the trend in Figure 5.3, while they are better in agreement with the samples used by Groves et al. (2004) (their figure 2). Anyway $log(N/O)$ is always overestimated when the abundances are above $Z_{\odot}$. It appears that UV-galaxies have a large spread in $log(N/O)$ values so it could be possible that HII and star-burst galaxies have a different chemical abundances sets and it could be interesting to have a sample of gas abundances in nuclei of spiral galaxies in order to check if the adopted function is actually an upper limit or not. To conclude the number of obtained models are 10390, 9782, 9022 and 8207, respectively for D/G=0.25, 0.50, 0.75, 1.00. The models will be accepted if they are classified as S2 in the Veilleux & Osterbrock (1987) diagnostic diagrams, following the Kewley's conditions (Kewley et al., 2006), and the fluxes are in the observed ranges, following Koski's diagrams (Koski, 1978).

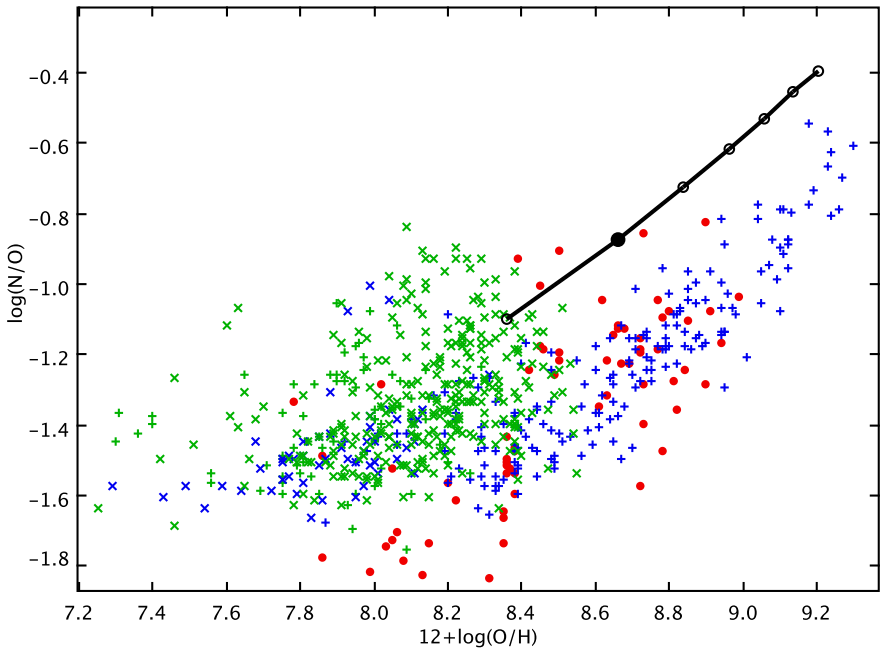

Figure 5.3: log(N/O) vs 12+log(O/H): *filled red circles* are UV galaxies (Contini et al., 2002), *blue plus* are HII regions in spiral galaxies (van Zee et al., 1998), *green plus* are HII regions in blue compact galaxies (van Zee & Haynes, 2006), *blue crosses* are HII regions in dwarf irregular galaxies (Izotov & Thuan, 1999) and *green crosses* are emission line galaxies (Izotov et al., 2006). *Black line* is the adopted N/O function. *Black circles* show the adopted metallicity values $Z/Z_{\odot}$, respectively 0.5, 1 (*filled circle*), 1.5, 2, 2.5, 3, 3.5.

Table 5.2: adopted abundances and depletion factors

element	$[X/H]_{\odot}$	$[X/H]_d$	$[X/H]_g$	$depl(X)_{1.00}$	$[X/H \cdot 0.75]_d$	$[X/H]_g$	$depl(X)_{0.75}$	$[X/H \cdot 0.50]_d$	$[X/H]_g$	$depl(X)_{0.50}$	$[X/H \cdot 0.25]_d$	$[X/H]_g$	$depl(X)_{0.25}$
He	-1.07		-1.07	0.0		-1.07	0.0		-1.07	0.0		-1.07	0.0
Li	-10.95		-10.95	0.0		-10.95	0.0		-10.95	0.0		-10.95	0.0
Be	-10.62		-10.62	0.0		-10.62	0.0		-10.62	0.0		-10.62	0.0
B	-9.3		-9.3	0.0		-9.3	0.0		-9.3	0.0		-9.3	0.0
C	-3.61	-3.91	-3.91	-0.3	-4.04	-3.81	-0.2	-4.21	-3.74	-0.12	-4.51	-3.67	-0.06
N	-4.22	-4.52	-4.52	-0.3	-4.65	-4.42	-0.2	-4.82	-4.34	-0.12	-5.12	-4.28	-0.06
O	-3.34	-3.71	-3.58	-0.24	-3.84	-3.51	-0.17	-4.01	-3.44	-0.1	-4.31	-3.39	-0.05
F	-7.44		-7.44	0.0		-7.44	0.0		-7.44	0.0		-7.44	0.0
Ne	-4.16		-4.16	0.0		-4.16	0.0		-4.16	0.0		-4.16	0.0
Na	-5.83	-5.96	-6.43	-0.6	-6.08	-6.19	-0.36	-6.26	-6.03	-0.2	-6.56	-5.92	-0.09
Mg	-4.47	-4.5	-5.62	-1.15	-4.63	-4.99	-0.52	-4.8	-4.74	-0.27	-5.1	-4.59	-0.11
Al	-5.63	-5.65	-7.07	-1.44	-5.77	-6.19	-0.56	-5.95	-5.92	-0.29	-6.25	-5.75	-0.12
Si	-4.49	-4.55	-5.38	-0.89	-4.68	-4.95	-0.46	-4.85	-4.74	-0.25	-5.15	-4.6	-0.11
P	-6.64		-6.64	0.0		-6.64	0.0		-6.64	0.0		-6.64	0.0
S	-4.86	-5.13	-5.2	-0.34	-5.25	-5.09	-0.23	-5.43	-5.0	-0.14	-5.73	-4.92	-0.06
Cl	-6.5	-6.8	-6.8	-0.3	-6.93	-6.7	-0.2	-7.1	-6.63	-0.12	-7.4	-6.56	-0.06
Ar	-5.82		-5.82	0.0		-5.82	0.0		-5.82	0.0		-5.82	0.0
K	-6.92		-6.92	0.0		-6.92	0.0		-6.92	0.0		-6.92	0.0
Ca	-5.68	-5.68	-8.2	-2.52	-5.81	-6.28	-0.6	-5.98	-5.98	-0.3	-6.28	-5.8	-0.12
Sc	-8.95		-8.95	0.0		-8.95	0.0		-8.95	0.0		-8.95	0.0
Ti	-7.1		-7.1	0.0		-7.1	0.0		-7.1	0.0		-7.1	0.0
V	-8.0		-8.0	0.0		-8.0	0.0		-8.0	0.0		-8.0	0.0
Cr	-6.36		-6.36	0.0		-6.36	0.0		-6.36	0.0		-6.36	0.0
Mn	-6.61		-6.61	0.0		-6.61	0.0		-6.61	0.0		-6.61	0.0
Fe	-4.55	-4.57	-5.92	-1.37	-4.69	-5.1	-0.55	-4.87	-4.83	-0.28	-5.17	-4.67	-0.12
Co	-7.08		-7.08	0.0		-7.08	0.0		-7.08	0.0		-7.08	0.0
Ni	-5.77	-5.79	-7.17	-1.4	-5.91	-6.32	-0.55	-6.09	-6.05	-0.28	-6.39	-5.89	-0.12
Cu	-7.79		-7.79	0.0		-7.79	0.0		-7.79	0.0		-7.79	0.0
Zn	-7.4		-7.4	0.0		-7.4	0.0		-7.4	0.0		-7.4	0.0

Notes. [X/H]=log(X/H), $d = dust$, $g = gas$.

Table 5.3: Nitrogen depletion factors, D/G=1.00

$Z/Z_\odot$	$log(O/H)$	$log(N/H)$	$log(N/H)_{gas}$	$depl$
0.5	-3.64	-4.75	-5.54	-0.79
1	-3.34	-4.22	-4.52	-0.3
1.5	-3.16	-3.89	-4.09	-0.19
2	-3.04	-3.66	-3.8	-0.14
2.5	-2.94	-3.48	-3.59	-0.11
3	-2.86	-3.32	-3.41	-0.09
3.5	-2.8	-3.19	-3.27	-0.08

5.3 Composite models

As discussed in the previous chapters, the Seyfert spectra show two gas components, responsible for high and low ionization lines, respectively. Hence, single cloud models are an oversemplification that does not allow us to reproduce all the observed spectral properties. A double component model with high and low ionization clouds is necessary. We explored two kinds of composite models: Binette's models and 2 clouds models. The first type extends the parameter exploration of the work of Binette et al. (1996). The second one is based on a combination of two models (Komossa & Schulz, 1997) obtained from the single cloud model described in Sect. 7.2.

We calculated all the possible combinations between two clouds for a fixed power-law index and metallicity. The spectral lines from the two clouds are combined with a weighted mean, where the weight is given by the product of the ratio of H_β luminosities and the geometrical factor (GF), intended as the ratio ω_1/ω_2 of the solid angles subtended by the clouds with respect to the source. The formula applied to combine the fluxes was derived according to the following steps. The luminosity of an emission line is given by

$$L = 4\pi r^2 S\omega/4\pi \tag{5.6}$$

where r is the inner radius of the nebula, $\omega/4\pi$ is the covering factor, S the emission line intensity ($erg\ s^{-1}\ cm^{-2}$); then

$$L = 4\pi d^2 F = 4\pi r^2 S\omega/4\pi \tag{5.7}$$

where F is the observed flux ($erg\ s^{-1}\ cm^{-2}$) and d is the distance to the source. Defining the density of ionizing photons ($s^{-1}\ cm^{-2}$) as

$$\phi(H^0) = Q(H^0)/4\pi r^2, \tag{5.8}$$

where $Q(H^0)$ is the number of ionizing photons emitted from the source in a second, and the ionization parameter as

$$U = \phi(H^0)/n_H c, \tag{5.9}$$

if there are two clouds then

$$U_1/U_2 = r_2^2 n_2/r_1^2 n_1 \Rightarrow r_2^2/r_1^2 = U_1 n_1/U_2 n_2 \tag{5.10}$$

and

$$L_2/L_1 = 4\pi d^2 F_2/4\pi d^2 F_1 = F_2/F_1 = r_2^2 S_2 \omega_2 / r_1^2 S_1 \omega_1, \tag{5.11}$$

then

$$F_2/F_1 = U_1 n_1 S_2 \omega_2 / U_2 n_2 S_1 \omega_1. \tag{5.12}$$

In terms of H_β this ratio becomes

$$F_2(H\beta)/F_1(H\beta) = GF \cdot L_2^{'}(H\beta)/L_1^{'}(H\beta) \tag{5.13}$$

$L_2^{'}(H_\beta)/L_1^{'}(H_\beta)$ is the H_β luminosity ratio if $\omega_1 = \omega_2$, these values are given by CLOUDY for each model.

If we want to find the emission line intensity I_λ relative to H_β then

$$I_\lambda = \frac{(F_\lambda)_2 + (F_\lambda)_1}{F_{tot}(H_\beta)} \tag{5.14}$$

where $F_{tot}(H_\beta)$ is the total observed flux. Rearranging the terms we obtain

$$I_\lambda = \frac{(I_\lambda)_2 + \frac{F_1(H_\beta)}{F_2(H_\beta)}(I_\lambda)_1}{1 + \frac{F_1(H_\beta)}{F_2(H_\beta)}} \tag{5.15}$$

and finally

$$I_\lambda = \frac{(I_\lambda)_2 + \frac{L_2^{'}(H_\beta)}{L_1^{'}(H_\beta)} \cdot GF \cdot (I_\lambda)_1}{1 + \frac{L_2^{'}(H_\beta)}{L_1^{'}(H_\beta)} \cdot GF} \tag{5.16}$$

If GF goes to zero only the 2nd cloud is seen, otherwise if it goes to infinity, only the 1st cloud is seen. The values adopted for GF are five: 0.25, 0.5, 1, 2 and 4. Thus each pair of models gives five synthetic spectra. The total number of models obtained with the constrain of keeping fixed D/G, α, $Z/Z_\odot$ for each pair of clouds and after imposing the Kewley and Koski conditions are about 9000000.

Binette et al. (1996) and more recently Whittle et al. (2005) proposed a model with a double cloud where the first one is a low density nebula which filters the radiation coming from the source thus casting a shadow on the second cloud with higher density (Fig.5.5). A more realistic situation could be represented by a low-density cloud that contains higher density clouds or filaments (figure 4 of Binette et al., 1996). The low-density cloud has a higher ionization parameter, while the high-density cloud has a lower ionization parameter. The high ionization cloud is matter bounded (MB), the ionizing photons are not totally absorbed, this could explain the temperature problem (Villar-Martín et al., 2008) and the low ionization cloud is ionization bounded (IB). We extended Binette's models exploring the parameters α, U, $Z/Z_\odot$ and $N_c(H+)$ with a D/G=1.00. The first cloud filters the radiation and, depending on the column density, there are more or less ionizing photons reaching the second cloud. The transition between MB and IB is very sensitive to the column density. If the optical depth is high we fall back to the single cloud model. The spectral lines from the matter bounded and the ionization bounded cloud are combined according to Equation 5.16 but the adopted GF values cover a wider range, $0.1 - 10$, with a logarithmic step of 0.1. The GF is indicated by the authors as $A_{M/I}$, where M is for the matter bounded cloud and I for the ionization bounded cloud. In this picture only $A_{M/I} > 1$ has a physical meaning but if

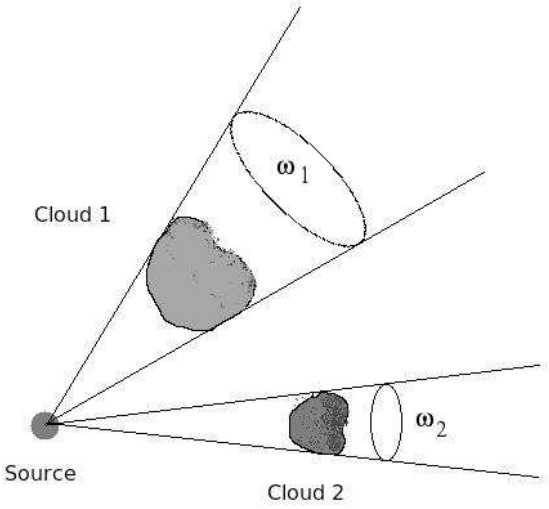

Figure 5.4: 2 clouds model, ω_1 and ω_2 are the solid angles subtended by the clouds.

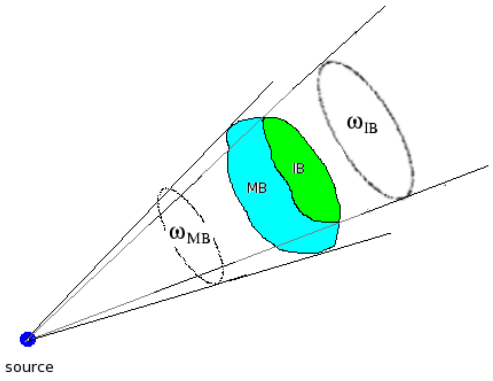

Figure 5.5: Binette model, ω_{MB} and ω_{IB} are the solid angles subtended by the clouds, matter bounded and ionization bounded.

the MB cloud is not seen or partially seen, because of the presence of dust clouds, then the $A_{M/I} < 1$ values may be taken as a weight of MB/IB visibility clouds.

The input parameters used in our models are shown in Table 5.4. The ionization parameter and the column density are defined only for the matter bounded cloud; $log(U)$ varies in the range $-2.4 \div -1.4$ with step 0.2, the logarithm column density values are in the range $19 \div 21$ with step 0.2. The ionization parameter for the ionization bounded cloud is calculated by CLOUDY and the iteration proceeds to reach a temperature of $4000K$. The densities are 50 cm^{-3} and 2500 cm^{-3} respectively for the matter bounded cloud and for the ionization bounded cloud. The power-law values are the same adopted in the previous models instead two metallicity values are added, 1.25 and 1.75 $Z\odot$. The choice of these new metallicities is suggested by the models distribution on the VO diagrams that shows a big gap between 1 and 1.5 $Z\odot$ and between 1.5 and 2 $Z\odot$. With these additional metallicity values the AGN area on VO diagrams is filled up. The total number of obtained models is 2970. Once the grid was completed the models were accepted only if they satisfied the above mentioned conditions.

Table 5.4: Input parameter values

$Z/Z\odot$	α	$log(U_{MB})$	$log(N_{c(H+)_{MB}}\ cm^{-2})$
0.5	-2.2	-2.4	19
1	-1.9	-2.2	19.2
1.25	-1.6	-2.0	19.4
1.5	-1.3	-1.8	19.6
1.75	-1	-1.6	19.8
2		-1.4	20
2.5			20.2
3			20.4
3.5			20.6
			20.8
			21

After the combination the number of total synthetic spectra is 6796.

5.4 Comparison of the models with the observed spectra

Our aim is to define the mean physical parameters which characterize the NLR using spectra in the visible range. The novelty in our approach is the method adopted for comparing the observed spectra with models. We attempted a fit of all observed spectral lines instead of limiting ourselves to reproduce the classical diagnostic line ratios. Of course there is no a unique solution and many models can satisfy an observed spectrum. For this reason the parameters values are obtained from a mean of the different models. We paid a particular attention to the metallicity level because this parameter is important in the investigation of the nature of the gas and its origin.

Oliva et al. (1999) proposed a new method for deriving abundances in the AGN NLR. It consists in selecting from a large sample (27000 models in their case) a set of "good" models that roughly reproduce the observed line spectra, and in slightly modifying the abundances to find the correct input parameters for various elements and thus the global metallicity. Our approach is somewhat different: we do not modify the input parameters but we use the χ^2 test, on the emission-line fluxes, to identify the nearest set of models to each observed spectrum out of millions of synthetic spectra.

The χ^2 is given by

$$\chi^2 = \sum_i (F_{\lambda_{obs}} - F_{\lambda_C})_i^2/(\sigma_i)^2 \tag{5.17}$$

where $F_{\lambda_{obs}} - F_{\lambda_C}$ is the difference between the observed flux and the model flux given by CLOUDY, σ_i the error associated to the line i. The comparison between observed and modelled spectra is based on those synthetic lines that would have $S/N > 3$ in the observed spectra and therefore are expected to be detectable. If some lines are below the S/N value of the observed spectrum, or are not present in the observed spectra, they are excluded from the χ^2 calculation. Two further parameters that must be taken into account are the reddening, A_V, and the scale factor $F(H_\beta)$. The χ^2 test is performed using the measured fluxes not corrected by reddening. The model fluxes are reddened in order to achieve the observed $F(H_\alpha)/F(H_\beta)$ ratio. This way we avoid of correcting the observed fluxes by assuming a

fixed $F(H_\alpha)/F(H_\beta)$ intrinsic ratio. In fact, although this ratio is close to 3.1 many models differ from this value by a small but significant amount. A_V is calculated by applying the extinction law of Cardelli et al. (1989)

$$A_V = 7.22 \cdot \left[log\left(\frac{F(H_\alpha)}{F(H_\beta)}\right)_{observed} - log\left(\frac{F(H_\alpha)}{F(H_\beta)}\right)_{CLOUDY} \right] \tag{5.18}$$

We adopted nine different values of the $F(H_\alpha)/F(H_\beta)$ obtained combining $F(H_\alpha) \pm \Delta F(H_\alpha)$ with $F(H_\beta) \pm \Delta F(H_\beta)$[1]. Then the mean ($\langle F_\alpha/F_\beta \rangle$) and the root mean square (σ) of the ratios are calculated. All the values within the range $-\sigma < \langle F_\alpha/F_\beta \rangle < \sigma$ which give a positive A_V are taken into account. Thus for each model up to 9 different synthetic spectra are calculated. The scale factor permits us to compare directly the reddened model with the observed spectrum. In fact CLOUDY fluxes are relative to $F(H_\beta)$. We choose to use the absolute fluxes to avoid too large errors that are involved when relative fluxes are used. The disadvantage of this choice is the need to introduce the 2 mentioned parameters, A_V and $F(H_\beta)$. The accepted model must satisfy the prefixed significance level, which is suggested by the analysis of the reduced χ^2 distribution:

$$\chi^2/dof = \chi^2/(nr - np) \tag{5.19}$$

where dof are the degrees of freedom (dof hereafter), nr is the number of measured lines and np the number of parameters used in the models. The χ^2/dof distribution must be similar to a Gaussian peaked on 1. This is the clue that the accepted models are good. If the peak is $<< 1$ there is an "overestimate" in the fitting, presumably the errors are too large thus making it find an acceptable fit although with poorly defined parameters. If the peak is $>> 1$ the models are not good or the errors are too small. After many tests, we found that in order to obtain a correct χ^2/dof distribution, the significance level must be between 5% and 10% (we adopt 10%) and the assumed flux errors 2σ. If 1σ is used the χ^2/dof distribution has the peak with a value $>> 1$, on the other hand with 3σ, the peak is lower than 0.2. The best fit model is characterized by the minimum χ^2 (χ^2_{min}); if this model is accepted all the models within the assumed significance level which fall within an assumed confidence region are accepted. This condition is expressed by the following formula

$$\chi^2 - \chi^2_{min} < K \tag{5.20}$$

where K is the selected value for a given probability (Mollá & Hardy, 2002). We adopted 25% of confidence. Thus for each fitted spectrum there is a group of accepted models and the best parameter values are obtained as the mean over all these models.

In this analysis there are 7 parameters for the single cloud models (1C hereafter), therefore we need a number of measured lines higher than 7, 11 parameters for 2 clouds models (2C hereafter), requiring 12 or more measured lines and finally 7 parameters for Binette's models (B hereafter). The parameters for the three types of models are listed in Table 5.5.

About 50% of the spectra have less than 12 measured lines, therefore the 2C models can be applied to one half of the sample but this contains the best quality spectra with higher S/N ratio and with a higher number of measured lines.

In order to compare the different kinds of models the spectra are subdivided into two groups, those with $nr \geq 12$ and those with $nr < 12$. The D/G is not considered a parameter

[1] writing in compact form the fluxes $F_\alpha = F(H_\alpha)$, the ratios are F_α/F_β, $(F_\alpha + \Delta F_\alpha)/F_\beta)$, $(F_\alpha - \Delta F_\alpha)/F_\beta)$, $F_\alpha/(F_\beta - \Delta F_\beta)$ and so on.

Table 5.5: The input parameters

Parameter	1C	2C	B
power-law index, α	yes	yes	yes
metallicity, $Z/Z_{\odot}$	yes	yes	yes
density, Ne	yes	yes	fixed
column density, Nc(H+)	yes	yes	yes
ionization parameter, U	yes	yes	yes
density 2nd cloud, Ne_2	no	yes	fixed
column density 2nd cloud, $Nc(H+)_2$	no	yes	calculated
ionization parameter 2nd cloud, U_2	no	yes	calculated
geometrical factor, GF	no	yes	yes
Reddening, A_V	yes	yes	yes
Scale factor, $F(H_{\beta})$	yes	yes	yes
number of parameters	7	11	7

Table 5.6: S2. Number of fitted spectra.

D/G	1C	1C $nr < 12$	1C $nr \geq 12$	2C
0.25	1249/2153	853/1141	396/1012	404/1012
0.50	1375/2153	912/1141	463/1012	486/1012
0.75	1445/2153	930/1141	515/1012	554/1012
1.00	1426/2153	939/1141	487/1012	561/1012
	B	B $nr < 12$	B $nr \geq 12$	
1.00	1274/2153	815/1141	459/1012	

because it is a mere assumption that cannot be verified, therefore the models with different D/G values are treated separately. This implies four families of models, one for each D/G value.

In the S2 sample, out of 2153 spectra, 1141 have $nr < 12$ and 1012 have $nr \geq 12$. Thus the comparison between 1C and 2C models is based on 1012 spectra. The numbers of fitted spectra for each D/G value are given in Table 5.6 depending on the number of measured emission lines. Column 1 contains the D/G values, colums 2, 3 and 4 give the number of fitted spectra with 1C models, and column 5 those fitted with 2C models. Then the last row contains Binette models with the same sub-division of 1C models. The total percentage of spectra which were successfully fitted are about 65%, 50% and 60% respectively for the 1C, 2C and B models. So, apparently, the 1C models are able to reproduce the highest percentage of spectra, but the number of fitted spectra is not the only parameter to be considered. The spectra well fitted with $nr < 12$ are 80%, while about 45% are the fitted spectra with $nr \geq 12$. A similar result is obtained with B models. With the 2C models the result is similar, 50% are the fitted spectra. Our aim is not to fit the vast majority of the observed spectra but to obtain a good quality fit.

Figure 5.6 shows the χ^2/dof distributions. The 1C models distribution shows a little skewness toward the low values especially for D/G=1 and 0.75, the same is true for B models. Instead, the 2C models show a small tail at high values, but a more regular distribution. However, all these distributions are acceptable and it is very difficult to obtain a better result

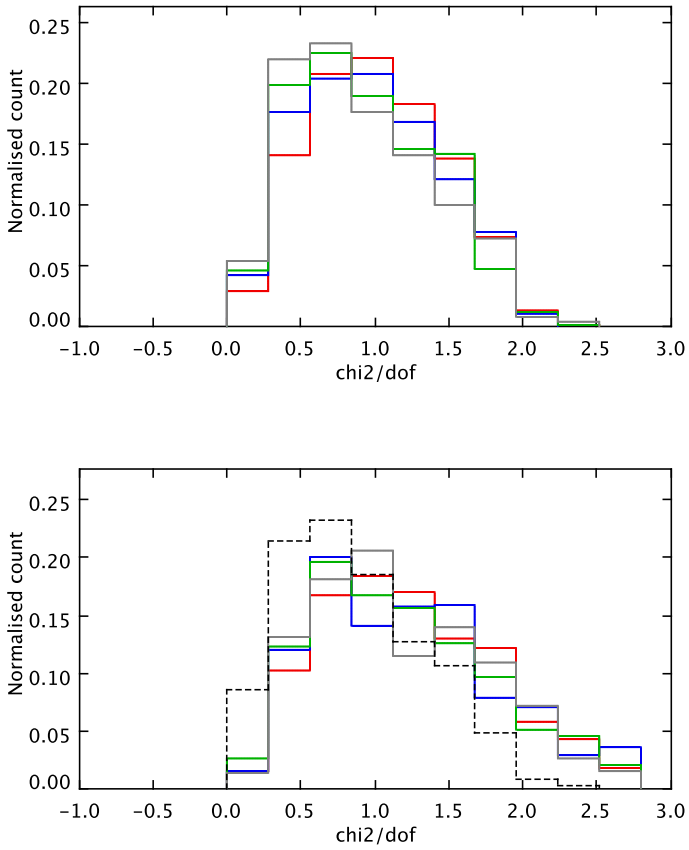

Figure 5.6: S2 sample χ^2/dof distribution for 1C models (*top*) and 2C and B models (*bottom*) and the different D/G values: 0.25 (*red*), 0.50 (*blue*), 0.75 (*green*) and 1.00 (*grey*). B models are represented by the *black dashed line*.

using grids of models with low resolution (i.e. large steps in the parameter values). The major difference between the models appears when the absolute χ^2 are compared. In fact, while χ^2/dof tells us the goodness of the adopted procedure (the input model parameters, the choice of the significance level and errors), the choice between two models which are able to fit the same spectrum is determined by the χ^2 value, the lowest value corresponding to the best model.

Comparing the χ^2 distributions it appears that the lowest χ^2 values are obtained with 2C models. The cumulative distributions (Figure 5.7) show clearly this great difference in the fitting between these two kinds of models. For a given type of models, there is not a large difference in the goodness of models with different D/G values, however, the largest number of fitted spectra is obtained for D/G= $0.75 \div 1$, with the minimum χ^2 for D/G=1. More interesting is the comparison of the χ^2 distributions between the spectra which are fitted by both 1C and 2C models, and by both B and 2C models (shared spectra). For each D/G value (starting from 0.25) there are respectively 289, 356, 410 and 396 shared spectra, the χ^2 distribution is dramatically different. As before the difference is better evaluated on the cumulative distribution (Figure 5.8). The natural result is that when the spectra have a good S/N the best fit is obtained using 2C models. Of course we need many measured lines and

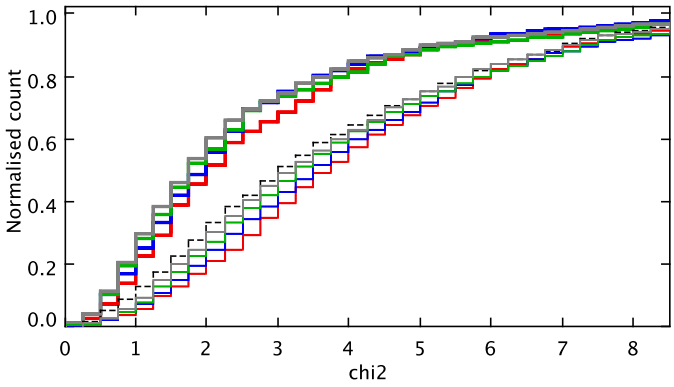

Figure 5.7: S2 sample χ^2 cumulative distribution for 1C models (*thin lines*), 2C models (*thick lines*) and B models (*black dashed line*), colors are as in figure 5.6.

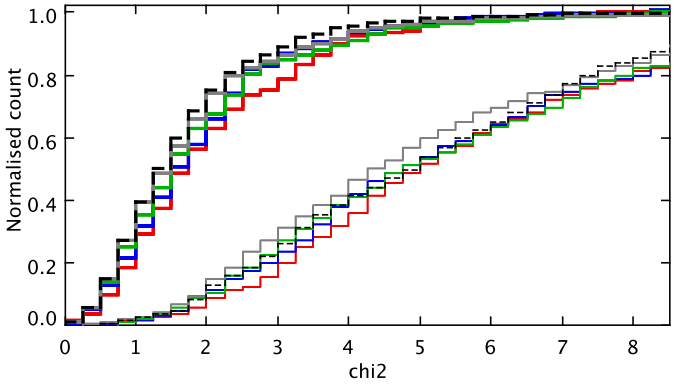

Figure 5.8: S2 sample χ^2 cumulative distribution as in Figure 5.7, for shared fitted spectra between 2C and 1C models, and between 2C and B models (*black dashed lines*).

if we want to fit a greater number of spectra the parameter resolution should be increased, especially for the power-law index and the ionization parameter but this would require either long computational times or powerful computers. The same figure shows the shared spectra (398) between 2C and B models. The difference is similar to the previous one with the best fit obtained with 2C models.

Concerning the line fit Table 5.7 gives the percentage of failures for each measured line and for the 4 D/G values. The data show again that the 2C models fit better all the lines: this is reasonable because with two clouds it is possible to combine an high and a low ionization cloud. In any case we have to be careful with these data because sometimes the percentages are calculated over a few spectra so a single measure can modify drastically the result. This is true especially for $[ArIV]$ and $[FeVII]$ lines. The lines which show a greater failure are $[NI]5200$, $[FeVII]5721, 6087$, $HeI5876$ and $[ArIII]7135$. About $[NI]5200$ we stress that this line is generally weak (median value ~ 0.14) and very close to the MgI absorption triplet, which could not be always perfectly removed by the template subtraction procedure, with consequent large errors in its measurements. HeI emission line is partially overlapped with

Table 5.7: S2. Percentage of line failures

Model	1C				2C				B
D/G	0.25	0.50	0.75	1.00	0.25	0.50	0.75	1.00	1.00
$[OII]3727$	6	6	7	5	3	2	2	1	5
$[NeIII]3869$	2	2	1	1	2	0	0	3	2
$[NeIII]3968$	1	1	2	3	5	2	1	1	1
$[SII]4074$	8	18	18	25	0	0	0	0	17
$H_\gamma 4340$	0	1	1	1	0	0	0	0	1
$[OIII]4363$	10	0	7	8	3	6	6	8	0
HeII4686	2	1	1	3	0	1	0	0	1
$[ArIV]4711$	0	0	0	0	0	0	0	0	0
$[ArIV]4740$	33	25	25	20	0	0	0	0	25
$H_\beta 4861$	0	0	0	0	0	0	0	0	0
$[OIII]4959$	0	0	0	0	0	0	0	0	0
$[OIII]5007$	2	3	3	3	0	0	0	0	2
$[NI]5200$	67	62	59	57	34	29	32	34	59
$[FeVII]5721$	50	60	67	67	14	10	30	33	5
HeI5876	19	17	16	15	8	10	9	11	16
$[FeVII]6087$	62	61	66	63	9	15	15	65	28
$[OI]6300$	7	6	7	6	2	3	5	5	1
$[OI]6363$	2	1	1	1	0	0	1	0	1
$[NII]6548$	0	0	0	0	0	0	0	0	0
$H_\alpha 6563$	0	0	0	0	0	0	0	0	0
$[NII]6584$	2	3	4	5	0	0	0	0	1
$[SII]6716$	2	3	3	4	0	0	1	1	6
$[SII]6731$	4	4	4	4	8	6	4	1	11
$[ArIII]7135$	7	11	16	22	3	8	26	27	1
$[OII]7325$	0	0	0	0	0	0	0	10	0

the Na absorption line, so it is always underestimated. $[FeVII]5720, 6086$ are coronal lines and presumably they form in other regions or with other mechanisms. $[ArIII]7135$ has a high percentage of failure in most models, but an explanation is still missing. The high number of failures for $[SII]$ lines in B models depends on the fixed density values adopted.

An example of fit is shown in Figure 5.9. We stress that the χ^2 test was performed on the measured fluxes therefore if the emission-lines show asymmetries or double peaks, they are not taken into account reproducing the spectrum. The lines are reproduced using the measured FWHM and the flux obtained by the best fit model.

The S2b sample contains a lower number of fitted spectra, between 33% to 40% with the 1C and 2C models and 32% with B models. If the spectra with a number of measured lines greater than 12 is taken into account the number of fitted spectra goes down to $21\% - 25\%$ with the 1C and B models (Table 5.8).

The χ^2/dof distributions are similar to those of S2, with a reduced skewness for the 1C models and a very good distribution for B models (Figure 5.10). Figure 5.11 shows similar cumulative distributions for all type of models, with the 2C models providing a slightly better fit. If the number of fitted spectra is taken into account, it appears that the models are not very efficient, in any case when the shared spectra are considered 2C models are definitely better (Figure 5.12). The percentage of the involved lines in the failures has a similar trend when compared with the S2 results (Tab. 5.9).

Compared with the previous sample, the I-t shows a better fitting with 1C and B models, the number of fitted spectra is between $41\% - 47\%$ while for 2C models the percentage of

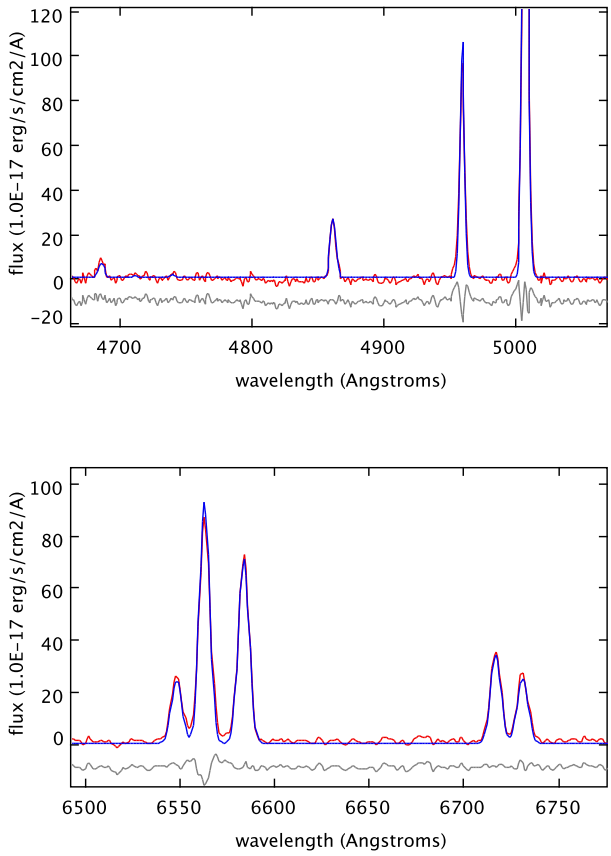

Figure 5.9: An example of fit with 2C model in H_β (*top*) and H_α (*bottom*) range respectively. The original spectrum is indicated in *red*, the model in *blue* and the residuals in *grey*.

Table 5.8: S2b. Number of fitted spectra.

D/G	1C	1C $nr < 12$	1C $nr \geq 12$	2C
0.25	160/479	93/149	67/330	103/330
0.50	171/479	96/149	75/330	128/330
0.75	199/479	105/149	94/330	131/330
1.00	188/479	106/149	82/330	136/330
	B	B $nr < 12$	B $nr \geq 12$	
1.00	158/479	86/149	72/330	

Table 5.9: S2b. Percentage of line failures

Model	1C				2C				B
D/G	0.25	0.50	0.75	1.00	0.25	0.50	0.75	1.00	1.00
$[OII]$3727	11	7	12	8	3	6	6	4	16
$[NeIII]$3869	6	1	2	2	5	4	1	9	4
$[NeIII]$3968	13	4	0	0	6	12	4	0	0
$[SII]$4074	0	0	0	0	0	3	3	9	0
H_γ4340	0	0	0	0	0	0	0	0	0
$[OIII]$4363	0	0	0	0	14	7	4	5	0
HeII4686	0	5	4	6	2	0	0	1	5
$[ArIV]$4711	0	5	4	0	0	0	0	0	0
$[ArIV]$4740	0	5	4	0	0	0	0	0	0
H_β4861	0	0	0	0	0	0	0	0	0
$[OIII]$4959	1	1	1	2	0	0	0	0	0
$[OIII]$5007	6	5	5	6	0	0	0	0	3
$[NI]$5200	0	7	0	0	0	6	3	16	0
$[FeVII]$5721	100	50	67	25	16	14	0	40	50
HeI5876	11	11	0	8	0	12	0	0	0
$[FeVII]$6087	80	67	83	100	7	14	0	81	67
$[OI]$6300	9	8	8	9	1	6	3	9	4
$[OI]$6363	0	5	0	5	0	1	1	0	0
$[NII]$6548	1	1	1	1	0	0	0	0	0
H_α6563	0	0	0	0	0	0	0	0	0
$[NII]$6584	5	6	9	5	2	0	0	0	1
$[SII]$6716	7	7	7	4	2	3	0	1	12
$[SII]$6731	7	5	6	6	7	9	6	3	19
$[ArIII]$7135	14	14	41	40	4	9	20	25	0
$[OII]$7325	0	0	20	20	0	0	0	0	0

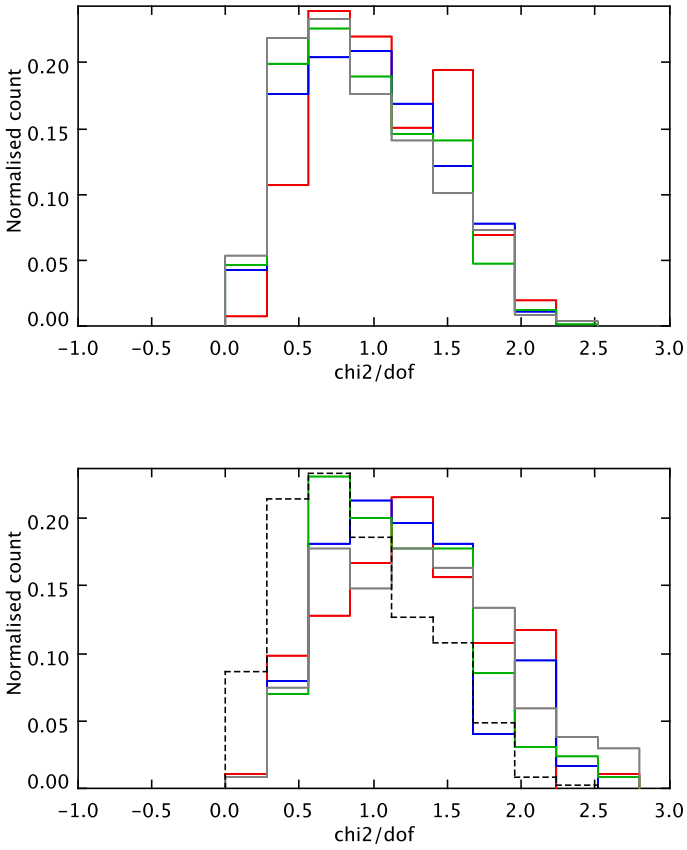

Figure 5.10: S2b sample χ^2/dof distribution for 1C models (*top*) and 2C and B models (*bottom*) and the different D/G values. Colors and line styles are as in Figure 5.6.

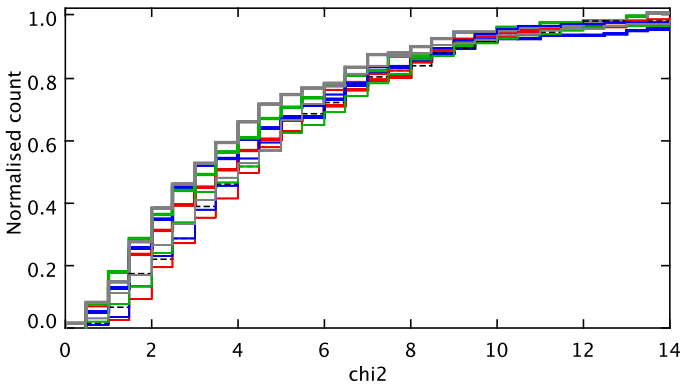

Figure 5.11: S2b sample χ^2 cumulative distribution for 1C models (*thin lines*), 2C models (*thick lines*) and B models (*black dashed line*), colors are as in figure 5.6.

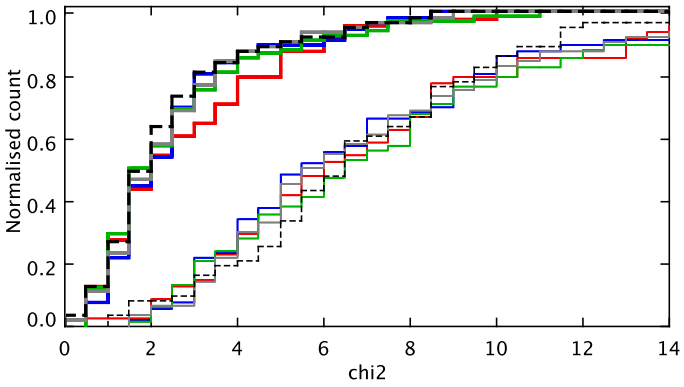

Figure 5.12: S2b sample χ^2 cumulative distribution as in Figure 5.11, for shared fitted spectra between 2C and 1C models, and between 2C and B models (*black dashed lines*).

Table 5.10: I-t. Number of fitted spectra.

D/G	1C	1C $nr < 12$	1C $nr \geq 12$	2C
0.25	215/521	126/164	89/357	97/357
0.50	229/521	128/164	101/357	119/357
0.75	235/521	131/164	104/357	124/357
1.00	246/521	133/164	113/357	115/357
	B	B $nr < 12$	B $nr \geq 12$	
1.00	233/521	124/164	109/357	

success is $27\% - 35\%$ (Tab. 5.10). When the spectra with a number of measured lines is greater than 11, the number of success decreases to 28% for 1C and B models.

The χ^2/dof distributions are very similar to the S2 case for all the models. It seems that S2 and I-t had the same correspondence with the models (Figure 5.13). On the contrary the χ^2 cumulative distribution (Figure 5.14) resembles to the S2b, even in this case the shared spectra are better fitted with 2C models (Figure 5.15). The percentage of line failures are still the same as in the previous samples apart from $[OIII]4363$, which shows a great percentage of failure. Presumably this could be due to the H_γ broad component which affects the $[OIII]4363$ flux. H_γ was excluded by the analysis because it was fitted with a single Gaussian.

5.5 Parameter determinations

The parameter determination is obtained by taking into account the mean value of the best fit models for each fitted spectrum. Sometimes the result consist of a single model, while in most of the cases the best fit contains some tens of models. The resolution of the power-law index α is actually too low, only five values are explored, then it is quite frequent to find the same common value for all the best fit models. In any case this parameter cannot be determined with high precision, observations in other spectral ranges would be necessary and dedicated models should be made. The description of the obtained input parameter values is done following the list in Table 5.5. The scale and geometrical factors are excluded by

Table 5.11: I-t. Percentage of line failures

Model	1C				2C				B
D/G	0.25	0.50	0.75	1.00	0.25	0.50	0.75	1.00	1.00
$[OII]3727$	10	9	8	9	4	0	0	0	10
$[NeIII]3869$	5	1	4	4	6	3	2	4	3
$[NeIII]3968$	26	28	13	10	10	5	4	4	4
$[SII]4074$	60	33	14	10	6	5	7	7	9
$H_\gamma 4340$									
$[OIII]4363$	70	67	70	71	38	46	41	44	47
HeII4686	0	3	0	3	0	3	1	0	7
$[ArIV]4711$	0	3	0	3	0	0	0	0	7
$[ArIV]4740$	0	3	0	3	0	0	0	0	7
$H_\beta 4861$	0	0	0	0	0	0	0	0	0
$[OIII]4959$	0	1	0	1	0	0	0	0	1
$[OIII]5007$	5	3	4	6	0	0	0	0	1
$[NI]5200$	0	10	11	18	0	0	4	20	0
$[FeVII]5721$	60	75	33	50	0	0	0	50	62
HeI5876	21	25	16	25	11	10	12	8	26
$[FeVII]6087$	58	50	67	79	0	5	14	56	50
$[OI]6300$	20	18	16	20	2	0	5	3	3
$[OI]6363$	0	0	0	0	0	0	0	0	0
$[NII]6548$	0	0	0	0	0	0	0	0	0
$H_\alpha 6563$	0	0	0	0	0	0	0	0	0
$[NII]6584$	2	4	4	4	0	0	0	0	2
$[SII]6716$	9	6	5	3	0	0	0	0	6
$[SII]6731$	5	4	3	6	2	3	1	1	16
$[ArIII]7135$	0	11	10	14	0	6	9	15	0
$[OII]7325$	0	0	0	0	0	0	0	0	0

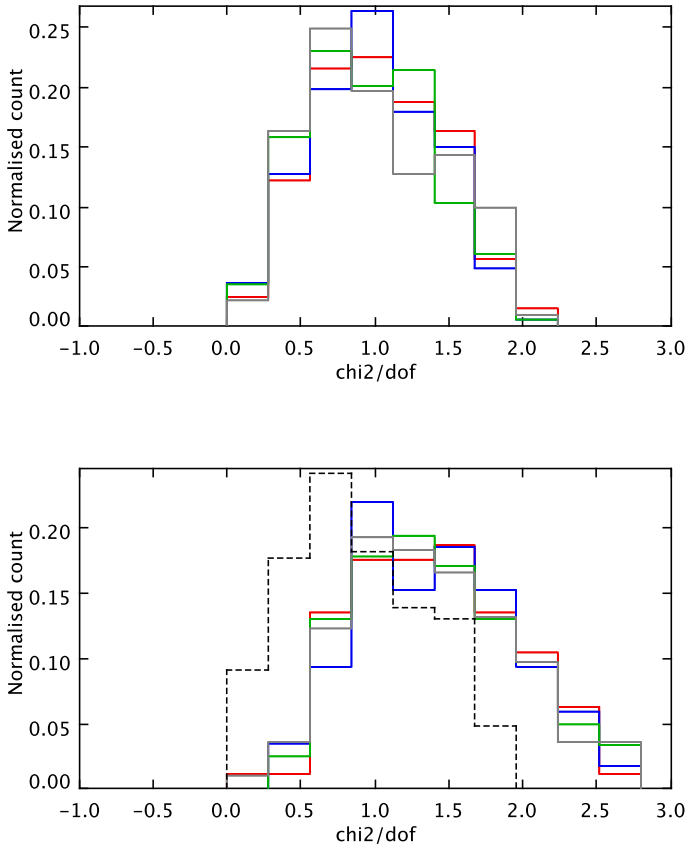

Figure 5.13: I-t sample χ^2/dof distribution for 1C models (*top*) and 2C and B models (*bottom*) and the different D/G values. Colors and line styles are as in Figure 5.6.

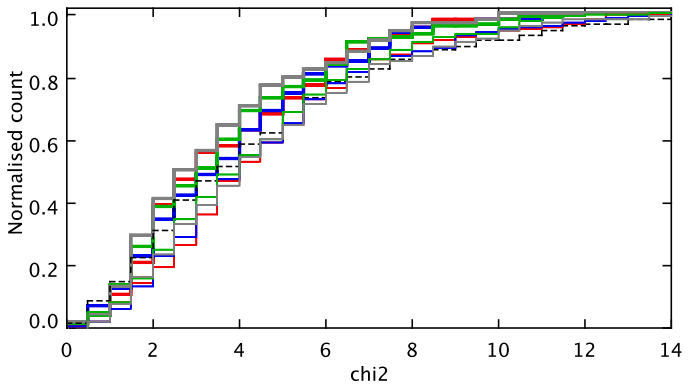

Figure 5.14: I-t sample χ^2 cumulative distribution for 1C models (*thin lines*), 2C models (*thick lines*) and B models (*black dashed line*), colors are as in figure 5.6.

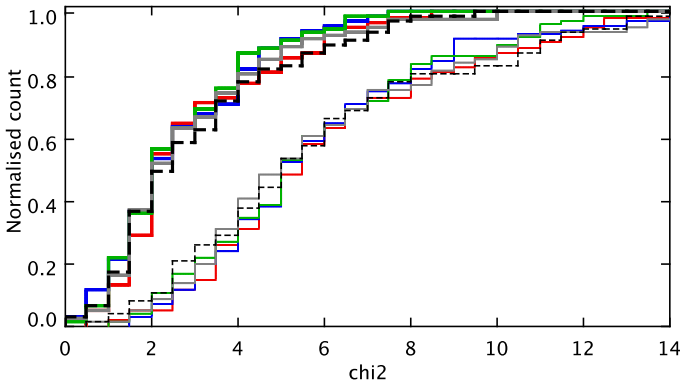

Figure 5.15: I-t sample χ^2 cumulative distribution as in Figure 5.14, for shared fitted spectra between 2C and 1C models, and between 2C and B models (*black dashed lines*).

the analysis because the first one depends on the single spectrum (the measured H_β flux), the second one shows an equidistribution in the adopted range, no preferential value is found with the exception of B models. Moreover the geometrical factor does not affect the input parameter models but it is only adopted to weight the different contribution of the clouds in composite models.

The mean value parameters for S2 sample, with their root mean square, σ, respectively for 1C, 2C and B models are summarized in Table 5.12. The power-law index, α, decreases down to -1.8 with increasing D/G value, this could be due to the decreasing gas metallicity content (a large quantity of metals are depleted into grains). In fact, lower gas metallicity implies less cooling and in order to obtain the same degree of ionization, a weaker ionizing spectrum is necessary. The total metallicity is well defined in all the models with a low scatter: $Z = 1.5 \div 2.5\, Z_\odot$ for 1C models and $Z = 1.0 \div 2.0\, Z_\odot$ for 2C and B models. These results confirm the high metallicity level of the gas, suggesting that the AGN fuel is evolved material, and support the idea that the gas has a local origin in the vast majority of cases. The model densities are in accord with those measured; 1C models and the 1st cloud of the 2C models have the same density, very similar to the measured sulphur density, whereas the 2nd cloud has a higher density similar to that obtained with the argon lines ratio.

The column density is similar for 1C models and the 1st cloud of 2C and B models. In 2C models the 2nd cloud has a lower column density but a lower ionization parameter too: this cloud is ionization bounded. The ionization parameter in 1C models does not change with D/G: $log(U) = -3$. In 2C models $log(U)$ varies slightly with D/G in the high ionization cloud, with a mean value $log(U) = -2.6$, while it maintains a value of -3.3 in the low ionization cloud. This indicates that 1C models have an intermediate ionization level with respect to the two clouds in the 2C models. Finally, A_V increases with D/G, as expected for an increasing dust content. There is a mean difference of 0.2 mag in A_V between the 1C and 2C models. Figure 5.16 shows the A_V derived from the models (all the fitted spectra obtained with all the models) vs the A_V estimated from the Balmer decrement. Modelled A_V tend to be larger than calculated A_V for both 1C and 2C models. The reason is that, as already mentioned, in most cases the intrinsic H_α/H_β ratio obtained by CLOUDY is lower than the assumed canonical value 3.1.

B models show a mean value of GF= 4: this means that the low density cloud (matter

Table 5.12: S2. Parameters output

D/G	0.25		0.50		0.75		1.00	
1C models								
Parameter	mean	σ	mean	σ	mean	σ	mean	σ
α	-1.5	0.3	-1.6	0.3	-1.7	0.3	-1.8	0.3
$Z/Z_{\odot}$	2.0	0.6	1.9	0.6	1.9	0.5	1.8	0.5
$log(Ne)$	2.3	0.7	2.3	0.7	2.2	0.6	2.1	0.7
$log(Nc(H+))$	20.5	0.7	20.3	0.6	20.0	0.5	19.9	0.4
U	-3.1	0.2	-3.1	0.2	-3.0	0.2	-3.0	0.3
A_V	1.4	0.6	1.5	0.6	1.5	0.6	1.6	0.6
2C models								
α	-1.3	0.3	-1.4	0.3	-1.6	0.3	-1.8	0.3
$Z/Z_{\odot}$	1.6	0.5	1.7	0.4	1.7	0.4	1.7	0.4
$log(Ne)$	2.2	0.8	2.2	0.8	2.1	0.7	2.2	0.8
$log(Nc(H+))$	20.2	0.4	20.2	0.4	20.2	0.4	20.2	0.4
$log(U)$	-2.7	0.4	-2.6	0.4	-2.6	0.4	-2.5	0.4
$log(Ne)_2$	3.0	0.9	2.8	0.9	2.7	0.9	2.5	0.8
$log(Nc(H+))_2$	19.7	0.4	19.7	0.3	19.7	0.3	19.7	0.3
$log(U_2)$	-3.3	0.2	-3.3	0.2	-3.3	0.2	-3.3	0.3
A_V	1.2	0.4	1.2	0.4	1.3	0.4	1.4	0.4

B models		
Parameter	mean	σ
α	-2.0	0.2
$Z/Z_{\odot}$	1.5	0.4
$log(Nc(H+))$	20.0	0.4
$log(U)$	-1.6	0.2
$log(U_{IB})$	-3.5	0.3
A_{MI}	4.1	2.1
A_V	1.6	0.6

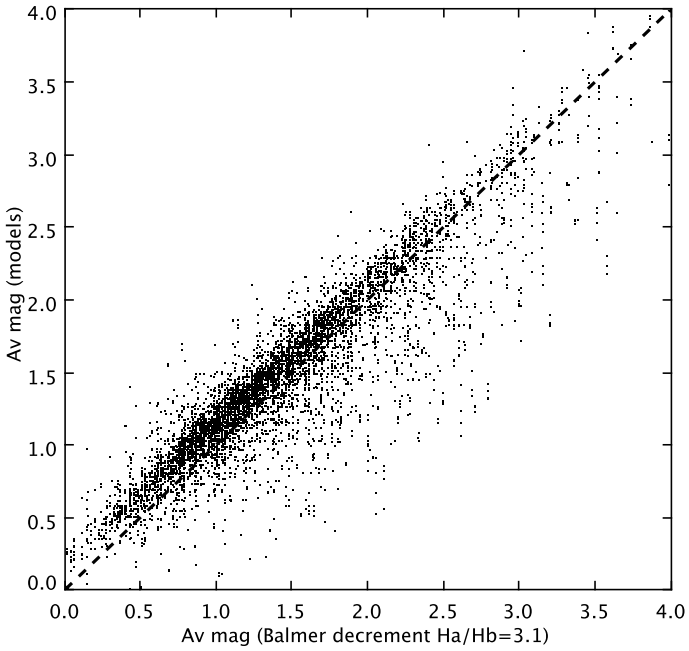

Figure 5.16: A_V (mag) obtained from the models vs A_V measured from the Balmer decrement.

bounded cloud) weights more than the ionization bounded cloud, perfectly in agreement with the assumptions.

The temperatures obtained through model fitting are listed in Table 5.13. The $[OII]$ and $[SII]$ values are consistent with those derived from the RO2 and RS2t ratios, whereas the $[OIII]$ temperature is lower than the measured one but still consistent with the photo-ionization case. The matter bounded cloud of B models shows a temperature in agreement with the measured ones.

In 1C and 2C models, the range of power-law index for the S2b and I-t samples is slightly different from that of the S2 sample. In particular, $\alpha = -1.7 \div -1.3$ for 1C models and $\alpha = -1.5 \div -1.1$ for 2C models. With B models the best value of α is similar in all three samples (Tables 5.14 and 5.16). As a consequence, in 1C and 2C models, the input spectrum for S2b and I-t is harder than for S2. S2b and I-t samples show a higher metallicity in both 1C and 2C models ($Z = 1.6 \div 2.7\, Z_\odot$ and $Z = 1.4 \div 2.3\, Z_\odot$ respectively). B models give $Z = 1.5 \div 2.1\, Z_\odot$. Temperatures do not differ remarkably from those of S2 (Tables 5.15 and 5.17).

5.6 Line ratio diagrams

In this section we will compare emission line ratios with ionization models. The aim is to find new diagnostic diagrams using NIR and UV lines too. In these diagrams instead of showing grids of models we use the line ratios derived from the 2C best-fit models. The idea is to assume the predicted emission line intensities (modelled spectra) in NIR and UV as a realistic estimate when a spectrum is well fitted in all the visible lines. To verify that we can rely in UV and NIR emission-line ratios derived from the best-fit models, we will compare them with

Table 5.13: S2. Model Temperatures

D/G	0.25		0.50		0.75		1.00	
1C	T_e	$\Delta(T_e)$	T_e	$\Delta(T_e)$	T_e	$\Delta(T_e)$	T_e	$\Delta(T_e)$
$[OIII]$	8274	1421	8522	1437	8879	1387	9374	1379
$[OII]$	7813	1145	8142	1184	8568	1130	9136	1192
$[SII]$	7026	1038	7282	1163	7608	1220	8021	1527
2C								
$[OIII]$	10923	3257	11172	3189	11225	2937	11535	2853
$[OII]$	10020	3353	10390	3169	10361	2806	10736	2658
$[SII]$	9219	3715	9560	3567	9334	3294	9759	3170
$[OIII]_2$	9282	1118	9298	1085	9516	1103	9679	1140
$[OII]_2$	8788	1078	8906	1016	9222	1020	9464	1006
$[SII]_2$	7995	1418	8049	1353	8307	1450	8450	1480

B	T_e	$\Delta(T_e)$
$[OIII]_{MB}$	16134	2951
$[OII]_{MB}$	15994	3079
$[SII]_{MB}$	16127	2996
$[OIII]_{IB}$	9749	798
$[OII]_{IB}$	9198	543
$[SII]_{IB}$	6753	311

published emission-line measurements of Seyfert galaxies in the relevant wavelength regimes.

In the UV range, the models are compared with the data provided by Kuraszkiewicz et al. (2004) catalogue which contains 28 Seyfert 2 or Intermediate-type Seyfert galaxies, observed fluxes are not corrected for reddening and therefore suitable to be compared with reddened models. The spectra were obtained from the Faint Object Spectrograph (FOS) of the Hubble Space Telescope (HST) prior to the installation of COSTAR.

In NIR the observed line fluxes were exctracted from: i) Riffel et al. (2006), a spectral atlas of 47 active galactic nuclei with 15 Seyfert 2 galaxies, whose NIR spectra were obtained at the NASA 3m Infrared Telescope Facility in the range $0.8 - 2.4\,\mu m$; ii) Osterbrock et al. (1992), NIR ($7000 - 10000\,\mathring{A}$) emission-line ratios of 12 Seyfert 2 and 13 Seyfert 1.5, obtained with the Lick Observatory 3 m Shane telescope; iii) Veilleux et al. (1997), J and K-band spectra of a sample of 33 Seyfert 2 galaxies obtained with CGS4 on UKIRT.

In order to investigate the emission-line ratios dependence on model parameters we used 11 emission-line diagrams in UV, optical, and NIR wavelength ranges:

$CIV1549/Ly_\alpha$ vs $HeII1640/Ly_\alpha$ (Whittle et al., 2005),
$[NV]1240/Ly_\alpha$ vs $HeII1640/Ly_\alpha$,
$MgII2798/Ly_\alpha$ vs $HeII1640/Ly_\alpha$,
$MgII2798/Ly_\alpha$ vs $[NeV]3426/[NeIII]3869$,
$[NeV]3426/[NeIII]3869$ vs $[OIII]5007/[OII]3727$,
$[SIII]9069, 9531/H_\alpha$ vs $[OII]7325/H_\alpha$ (Komossa & Schulz, 1997; Osterbrock et al., 1992),
$[SIII]9069, 9531/H_\alpha$ vs $[SII]6724/H_\alpha$ (Osterbrock et al., 1992),
$[FeII]12570/Pa_\beta$ vs $[OI]6300/H_\alpha$,
$[FeII]12570/Pa_\beta$ vs $[SIII]9069, 9531/Pa_\beta$,
$[NII]6584/[OII]7325$ vs $[NII]6584/[SII]6724$,
$[NII]6584/[OII]3727$ vs $[NII]6584/[SII]6724$.

Table 5.14: S2b. Parameters output

D/G	0.25		0.50		0.75		1.00	
1C models								
Parameter	mean	σ	mean	σ	mean	σ	mean	σ
α	-1.3	0.3	-1.4	0.3	-1.6	0.3	-1.7	0.3
$Z/Z_{\odot}$	2.2	0.6	2.2	0.6	2.1	0.5	2.1	0.5
$log(Ne)$	2.4	0.8	2.3	0.7	2.2	0.7	2.1	0.7
$log(Nc(H+))$	20.7	0.6	20.6	0.6	20.2	0.5	20.0	0.4
$log(U)$	-3.0	0.2	-3.0	0.2	-3.0	0.2	-2.9	0.3
A_V	1.5	0.7	1.5	0.7	1.6	0.7	1.6	0.7
2C models								
α	-1.1	0.2	-1.2	0.2	-1.4	0.3	-1.5	0.3
$Z/Z_{\odot}$	1.8	0.4	1.9	0.4	1.9	0.4	1.9	0.4
$log(Ne)$	2.4	0.7	2.4	0.7	2.3	0.7	2.3	0.7
$log(Nc(H+))$	20.3	0.4	20.3	0.4	20.2	0.4	20.3	0.5
$log(U)$	-2.5	0.4	-2.5	0.4	-2.5	0.4	-2.3	0.4
$log(Ne)_2$	2.9	0.8	2.8	0.8	2.7	0.8	2.5	0.8
$log(Nc(H+))_2$	19.7	0.4	19.7	0.3	19.7	0.3	19.7	0.3
$log(U_2)$	-3.3	0.2	-3.3	0.2	-3.2	0.2	-3.3	0.3
A_V	1.2	0.5	1.3	0.4	1.3	0.5	1.4	0.5

B models		
Parameter	mean	σ
α	-1.9	0.2
$Z/Z_{\odot}$	1.8	0.3
$log(Nc(H+))$	20.1	0.4
$log(U)$	-1.7	0.2
$log(U_{IB})$	-3.6	0.3
A_{MI}	4.7	2.1
A_V	1.5	0.7

Table 5.15: S2b. Model Temperatures

D/G	0.25		0.50		0.75		1.00	
1C	T_e	$\Delta(T_e)$	T_e	$\Delta(T_e)$	T_e	$\Delta(T_e)$	T_e	$\Delta(T_e)$
$[OIII]$	8472	1369	8615	1443	8943	1441	9306	1410
$[OII]$	7732	1092	7980	1152	8393	1116	8894	1191
$[SII]$	6831	1007	7019	1174	7327	1233	7723	1493
2C								
$[OIII]$	11614	2923	11868	2847	11984	2666	12448	2859
$[OII]$	10176	3229	10432	3207	10759	2615	11132	2910
$[SII]$	9306	3647	9534	3678	9989	3019	10305	3399
$[OIII]_2$	9267	927	9345	914	9648	963	9780	1050
$[OII]_2$	8656	852	8840	902	9149	909	9478	1000
$[SII]_2$	7894	1132	8039	1260	8279	1335	8585	1524

B	T_e	$\Delta(T_e)$
$[OIII]_{MB}$	15305	3236
$[OII]_{MB}$	15097	3372
$[SII]_{MB}$	15273	3284
$[OIII]_{IB}$	9296	770
$[OII]_{IB}$	8787	492
$[SII]_{IB}$	6608	393

We combined the emission-line ratios in order to obtain diagrams able to show a strong dependence on a specific parameter.

The five diagrams in the UV range are presented in Figures 5.17, 5.18, 5.19: in these diagrams the observed fluxes are used and then will be taken into account the emission-line ratios obtained from the reddened models. The $CIV1549/Ly_\alpha$ vs $HeII/Ly_\alpha$ diagram (Figure 5.17, *top*) shows a good correspondence with the data only when $log(U)$ of the first cloud is higher than -2.5. In the diagram D/G=1 models are shown. The Seyfert 2 ratios are not well reproduced in the $HeII/Ly_\alpha$ ratio, which is overestimated by the models. Only reducing the D/G value to 0.25 and using the first cloud fluxes the trend is a little better. The second diagram (Figure 5.17, *bottom*), $[NV]1240/Ly_\alpha$ vs $HeII/Ly_\alpha$, shows a total disagreement with the observed data. It is possible to increase the $[NV]1240/Ly_\alpha$ values only using the fluxes from the first cloud with high metallicity, between 2 and 3. The third and fourth diagrams (Figure 5.18) involve $MgII2798$. This line is very important in the analysis of the dust content because the Magnesium depletion factor is very high (-1.15), comparable with that of Iron, then the intensity is directly connected to the D/G ratio. In the $MgII2798/Ly_\alpha$ vs $HeII/Ly_\alpha$ we plotted only Seyfert 1.5 galaxies, no Seyfert 2 galaxies in the catalogue show this combination of measured lines. The models able to show a consistent distribution are those with low D/G (0.25) and a power-law index higher than -1.6. The $MgII2798/H_\beta$ vs $[NeV]3426/[NeIII]3869$ diagram shows the best fit models obtained respectively with D/G=1 (filled circles) and D/G=0.25 (open circles). Unfortunately there are few objects showing these lines but they are indicative of ionization state and D/G content. As in the previous diagram the comparison between models and data suggest a low D/G value. These diagrams support the idea that the regions where the UV lines are formed are poor of dust (Nagao et al., 2003).

The diagram in Figure 5.19 shows that the observed line ratios fill the upper region with

Table 5.16: I-t. Parameters output

D/G	0.25		0.50		0.75		1.00	
1C models								
Parameter	mean	σ	mean	σ	mean	σ	mean	σ
α	-1.4	0.3	-1.5	0.3	-1.6	0.3	-1.8	0.3
$Z/Z_{\odot}$	1.9	0.6	2.0	0.5	2.0	0.5	2.1	0.5
$log(Ne)$	2.5	0.8	2.4	0.7	2.3	0.7	2.1	0.7
$log(Nc(H+))$	20.8	0.6	20.5	0.6	20.3	0.5	20.1	0.4
$log(U)$	-3.0	0.2	-3.0	0.2	-2.9	0.2	-2.9	0.3
A_V	1.0	0.5	1.1	0.5	1.1	0.5	1.1	0.5
2C models								
α	-1.2	0.3	-1.3	0.3	-1.5	0.4	-1.7	0.3
$Z/Z_{\odot}$	1.6	0.5	1.6	0.5	1.7	0.4	1.8	0.4
$log(Ne)$	2.5	0.8	2.5	0.8	2.4	0.7	2.4	0.7
$log(Nc(H+))$	20.4	0.5	20.4	0.5	20.4	0.4	20.3	0.4
$log(U)$	-2.4	0.4	-2.4	0.4	-2.3	0.4	-2.3	0.3
$log(Ne)_2$	2.9	0.9	2.9	0.8	2.5	0.8	2.5	0.7
$log(Nc(H+))_2$	19.7	0.4	19.8	0.3	19.8	0.3	19.9	0.3
$log(U_2)$	-3.3	0.3	-3.3	0.2	-3.2	0.3	-3.1	0.3
A_V	1.0	0.4	1.1	0.4	1.1	0.4	1.1	0.4

B models		
Parameter	mean	σ
α	-1.9	0.3
$Z/Z_{\odot}$	1.6	0.4
$log(Nc(H+))$	20.1	0.3
$log(U)$	-1.8	0.3
$log(U_{IB})$	-3.7	0.4
A_{MI}	4.8	2.0
A_V	1.0	0.5

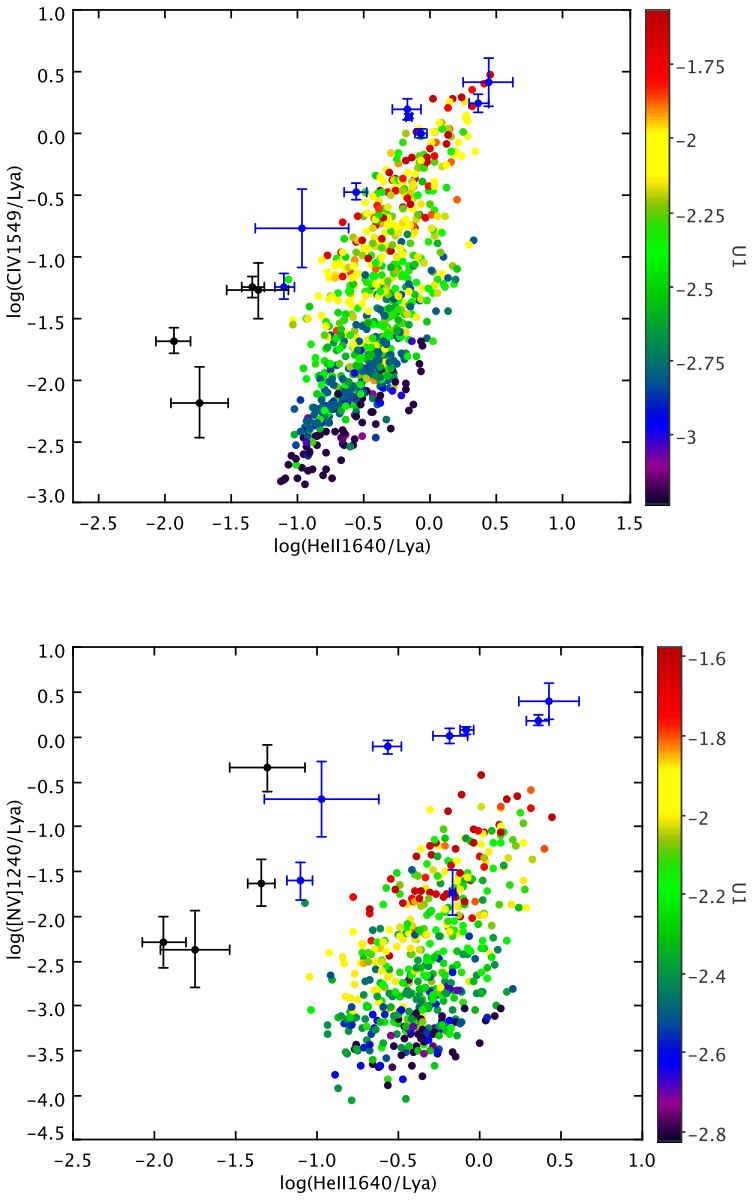

Figure 5.17: UV line ratio diagrams. $CIV1549/Ly_\alpha$ vs $HeII/Ly_\alpha$ (*top*), $[NV]1240/Ly_\alpha$ vs $HeII/Ly_\alpha$ (*bottom*). The circles are the best fit models for all the samples with D/G=1 (see the text) and the circles with the error bars are observed spectra by Kuraszkiewicz et al. (2004): Seyfert 2 are in *black* and Intermediate-type Seyfert in *blue*. Ionization paramenter value of the high ionization cloud (U1) is colour coded.

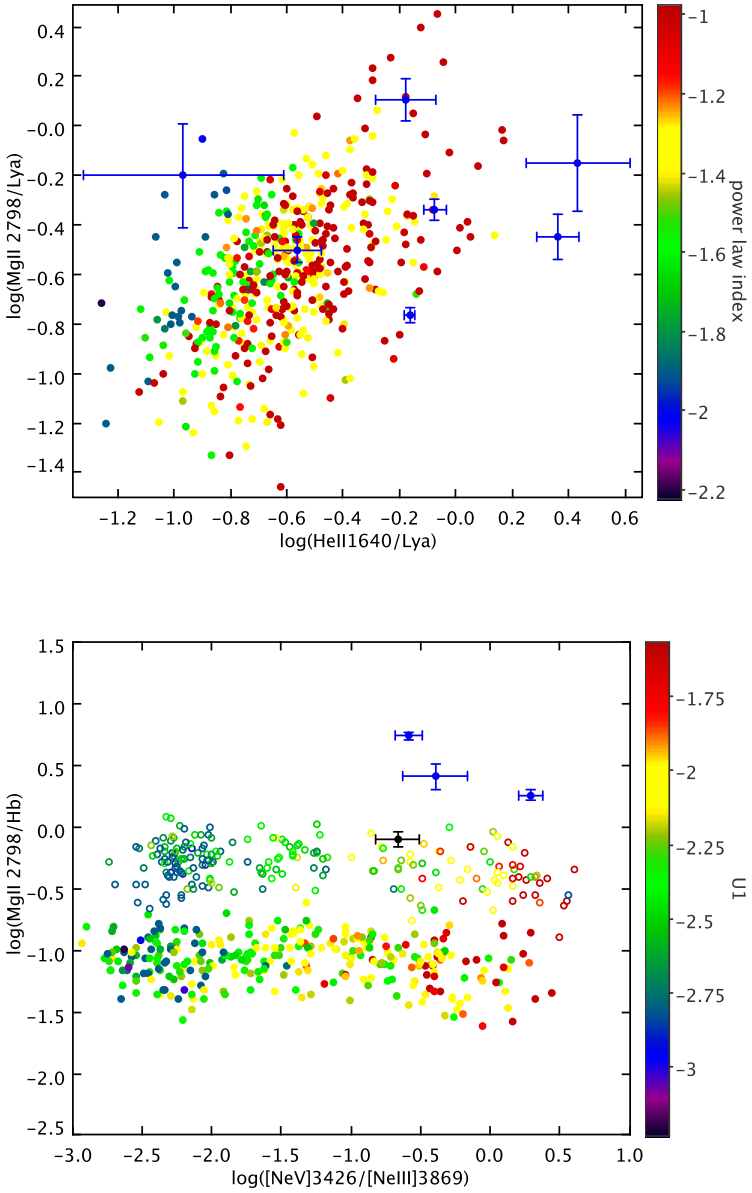

Figure 5.18: UV line ratio diagrams. *Top*: $MgII2798/Ly_\alpha$ vs $HeII/Ly_\alpha$, S2 best fit models with D/G=0.25. *Bottom*: $MgII2798/H_\beta$ vs $[NeV]3426/[NeIII]3869$, S2 best fit models with D/G=1 (*solid circles*) and D/G=0.25 (*open circles*). The circles with the error bars are observed spectra by Kuraszkiewicz et al. (2004): Seyfert 2 are in *black* and Intermediate-type Seyfert in *blue*. The values of power-law index (α) and ionization paramenter of the high ionization cloud (U1) are colour coded.

Table 5.17: I-t. Model Temperatures

D/G	0.25		0.50		0.75		1.00	
1C	T_e	$\Delta(T_e)$	T_e	$\Delta(T_e)$	T_e	$\Delta(T_e)$	T_e	$\Delta(T_e)$
$[OIII]$	8890	1441	8974	1431	9134	1472	9426	1448
$[OII]$	7940	887	8150	893	8424	902	8809	992
$[SII]$	6848	849	7020	924	7191	974	7468	1289
2C								
$[OIII]$	12285	2897	12347	2926	13038	3494	12110	2561
$[OII]$	10302	3111	10668	2954	11956	3645	10928	2224
$[SII]$	9422	3578	9878	3381	11156	4239	9909	2764
$[OIII]_2$	9578	1324	9783	1251	9803	1251	10038	1733
$[OII]_2$	8974	1210	9163	1099	9156	961	9496	1225
$[SII]_2$	8259	1533	8209	1528	8036	1404	8210	1631

B	T_e	$\Delta(T_e)$
$[OIII]_{MB}$	15356	3463
$[OII]_{MB}$	15141	3602
$[SII]_{MB}$	15312	3520
$[OIII]_{IB}$	9570	839
$[OII]_{IB}$	8917	587
$[SII]_{IB}$	6718	497

a reasonable constant $[NeV]3426/[NeIII]3869$ value. These ratios are connected with the gas excitation degree but in different emitting regions. In fact from this diagram it appears that these ratios are not correlated.

Onwards observed line ratios and those obtained by the models used in the diagrams are corrected from reddening because in visible and NIR it is easier to determine A_V through the hydrogen recombination lines. The following two diagrams (Figure 5.20) were proposed by Osterbrock et al. (1992) in order to classify the AGN and star-burst galaxies using the NIR $[SIII]9069, 9531$ lines. The observed line ratios used by these authors (and references therein) are overlapped to the models. The $[SIII]9069, 9531/H_\alpha$ vs $[OII]7325/H_\alpha$ diagram shows a good correspondence between models and the observations. The models indicate that these lines depend on the 2nd cloud with a $log(U)$ lower than -3. The second diagram has a larger dispersion of the observed ratios compared to the models. The line ratio values obtained by the models are more concentrated with no clear trend even if it is possible to distinguish different regions with different power-law index values.

Analogously to the Magnesium, Iron is a refractory element so it could be very sensitive to the dust content. If $[FeII]$ NIR lines are weak, this means that the Iron is condensed in grains. The $[FeII]$ ionization potential is 16.6 eV, then the emission is therefore produced predominantly in regions in which hydrogen is only partially ionized. The origin of the strong $[FeII]$ NIR emission lines in AGN is ambiguous. According to Veilleux et al. (1997), there are three principal processes which can contribute to the emission in these galaxies: X-rays from the central source may produce extensive partially ionized regions in NLR clouds of high optical depths, star-burst activity may be taking place in or near the nucleus of these galaxies and the interaction of radio jets with the surrounding medium may induce shocks and produce partially ionized cooling tails. Only a spatial information of the $[FeII]$ NIR emission will be able to solve the problem (Nisini et al., 2005). In the star-burst scenario the

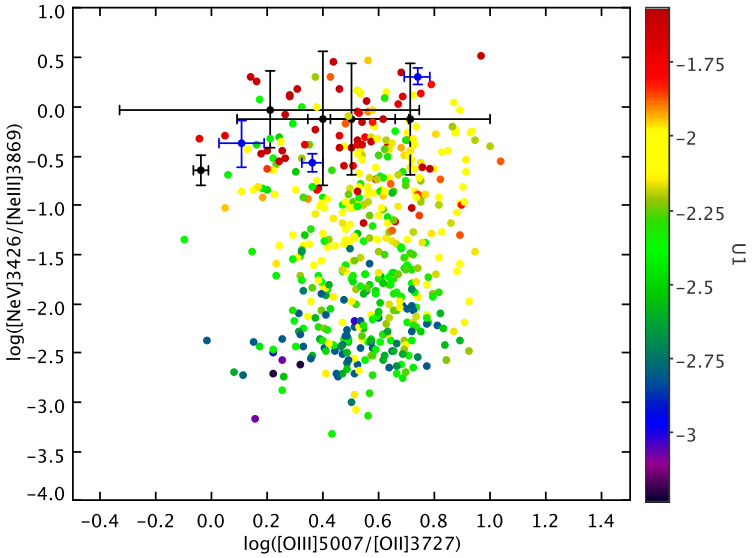

Figure 5.19: $[NeV]3426/[NeIII]3869$ vs $[OIII]5007/[OII]3727$; all samples best fit models with D/G=1. Symbols are as in Figure 5.17. Ionization paramenter value of the high ionization cloud (U1) is colour coded.

$[FeII]12570/Pa_\beta$ ratio is lower than 0.4 (Colina, 1993), the Veilleux et al. (1997) data show a ratio distribution with a median value around 1, compatible with the Riffel et al. (2006) and Heisler & De Robertis (1999) results, and the 80% of the sample has a value between 0.4 and 2.5. This result suggests that circumnuclear star-bursts are not the main source of [Fe II] emission in Seyfert galaxies. Concerning the shock mechanism the SNRs seem to underproduce $[FeII]/Pa_\beta$ ratio. Maybe strong AGN outflows and jet interactions could be able to increase this ratio (Veilleux et al., 1997). If the shock mechanism is working, a positive correlation between line fluxes and line width should be detected but no significant trend was observed by Veilleux et al. (1997) in their data. The grains could be dissolved if the shock waves velocity was higher than a few hundreds km/s but in the NLR we often observe a low velocity field. In $[FeII]12570/Pa_\beta$ vs $[OI]6300/H_\alpha$ diagram (Figure 5.21) we show the Veilleux et al. (1997) data and our S2 best fit models with D/G=1 and 0.75. The observed ratios are between the two sequences with a clear power law index trend. The ratios are well consistent with the 2C models. In this diagram the models are between the star-burst and SNRs regions (figure 5, Veilleux et al., 1997) then the photo-ionization hypothesis is well supported (Ramos Almeida et al., 2006; Alonso-Herrero et al., 1997).

Figure 5.22 shows $[FeII]12570/Pa_\beta$ vs $[SIII]9069, 9531/Pa_\beta$, ratios able to separate AGN from star-burst galaxies. In the diagram the S2 best fit models, with D/G=1 and D/G=0.25 are shown; the observed $[FeII]12570/Pa_\beta$ ratios by Riffel et al. (2006) are very similar and consistent with those previously mentioned in Veilleux et al. (1997). Compared to our models these diagrams show that the Iron is strongly depleted into dust.

The last two diagrams are relative to the metallicity. The $[NII]6584/[OII]7325$ and $[NII]6584/[SII]6724$ ratios are independent by the ionization parameter because both the ratios involve lines with similar ionization potential (Figure 5.23). The diagram is interesting because it is possible to distinguish two parameters, the metallicity and the density of the

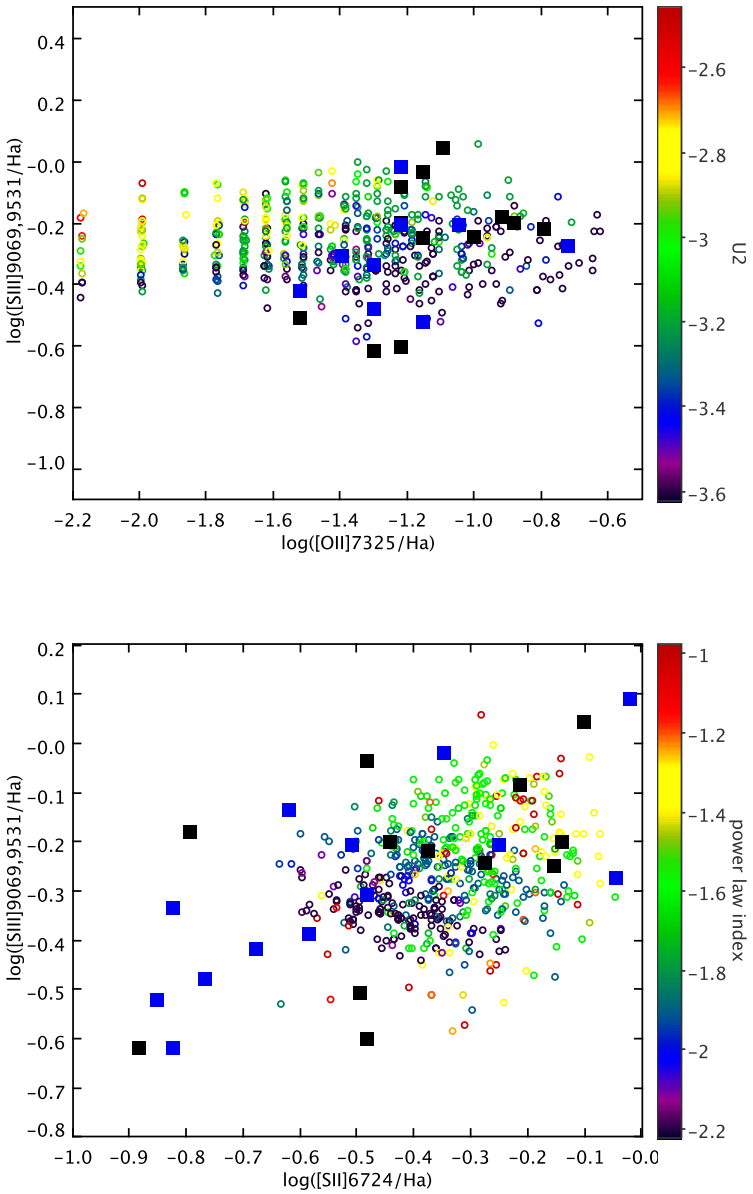

Figure 5.20: $[SIII]9069,9531/H_\alpha$ vs $[OII]7325/H_\alpha$ (*top*), $[SIII]9069,9531/H_\alpha$ vs $[SII]6724/H_\alpha$ (*bottom*). *Filled squares* are Osterbrock et al. (1992) data, Seyfert 2 are in *black* and Intermediate-type Seyfert in *blue*. *Open circles* are S2 best fit models with D/G=1. The values of ionization paramenter of the low ionization cloud (U2) and power-law index (α) are colour coded.

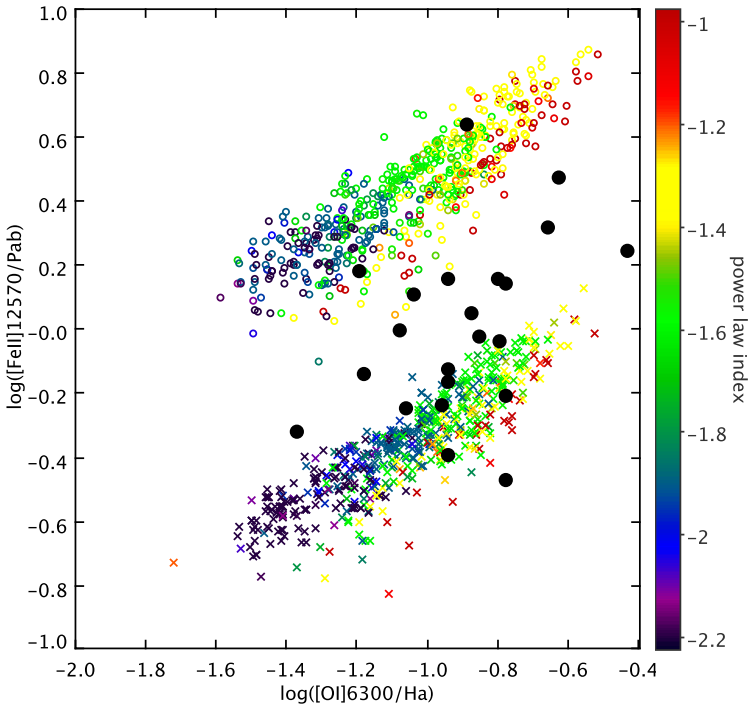

Figure 5.21: $[FeII]12570/Pa_\beta$ vs $[OI]6300/H_\alpha$. S2 best fit models with D/G=1 (*crosses*) and D/G=0.75 (*open circles*), the observed data (*filled black circles*) are obtained by Veilleux et al. (1997). Power-law index value (α) is colour coded.

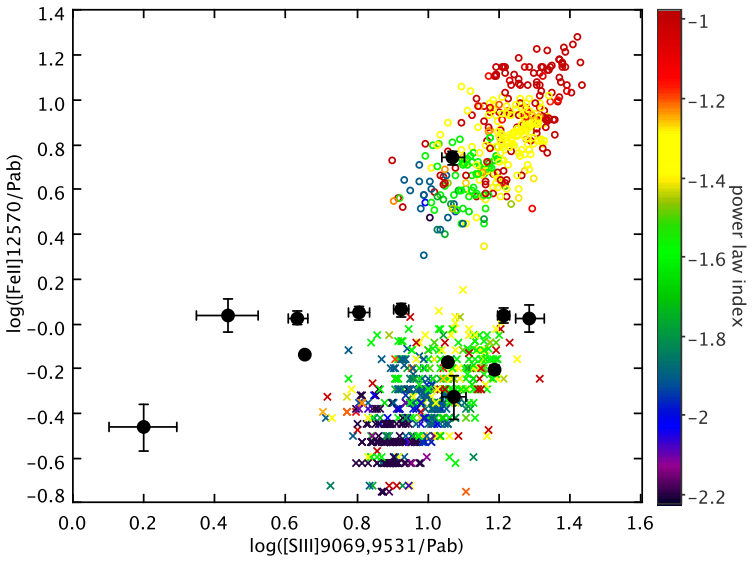

Figure 5.22: $[FeII]12570/Pa_\beta$ vs $[SIII]9069, 9531/Pa_\beta$. S2 best fit models with D/G=1 (*crosses*) and D/G=0.25 (*open circles*), the observed data (*filled black circles*) are obtained by Riffel et al. (2006). Power-law index value (α) is colour coded.

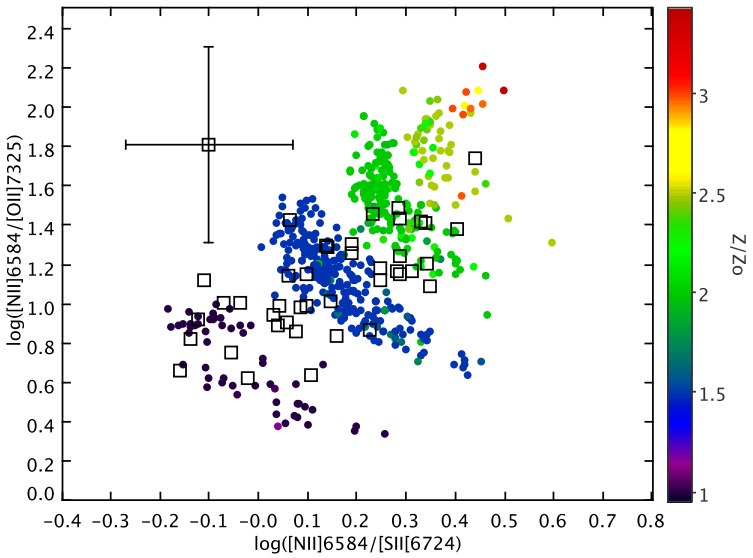

Figure 5.23: $[NII]6584/[OII]7325$ vs $[NII]6584/[SII]6724$. S2 best fit models, with D/G=1, are compared with our sample (*open squares*), only in 41 spectra it is possible to measure both $[OII]7320,7330$ lines. For each metallicity value (colour coded) the density sequence of the first cloud is plotted. The density increases from top left to bottom right.

2nd cloud (low ionization cloud). The metallicity degree is shown with the coloured scale and is given by the $[NII]6584/[SII]6724$ ratio, the density trend is represented by the sequence with fixed metallicity, the value increases from top right to bottom left. Here the models are compared with our S2 sample, unfortunately the $[OII]7320,7330$ lines are weak and only 41 spectra show both the lines. The trend is good even if the errors are large.

Finally $[NII]6584/[OII]3727$ vs $[NII]6584/[SII]6724$ is the best diagram sensitive to the metallicity. Here it is possible to use the SDSS data because these lines are measured in all the objects. The models have a low resolution in metallicity because we used few $Z/Z_{\odot}$ values, nevertheless the trend is clear (Figure 5.24), the observed data and the models are absolutely consistent. Again, the result is that the vast majority of these NLR have a metallicity between 1.5 and 2.5 $Z/Z_{\odot}$.

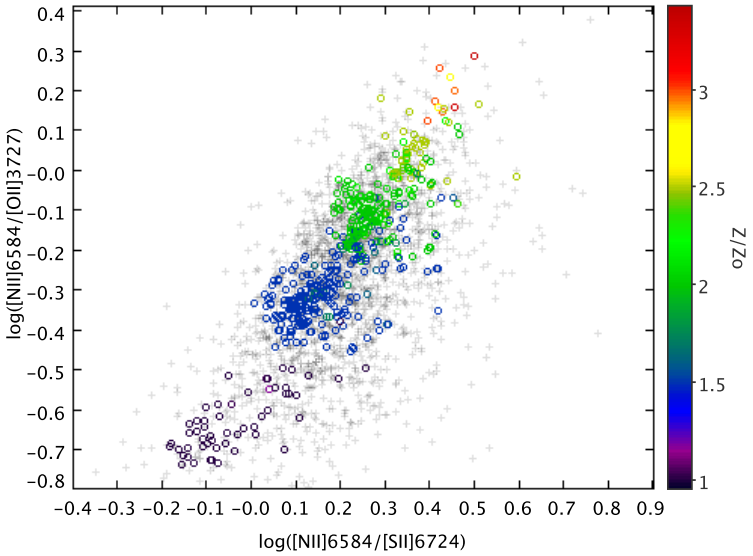

Figure 5.24: $[NII]6584/[OII]3727$ vs $[NII]6584/[SII]6724$. S2 best fit models with D/G=1 (*coloured open circles*) and S2 sample (*grey plus*). Metallicity value is colour coded.

.

.

Conclusions

The aim of this thesis is the spectroscopic analysis of the NLR in Seyfert galaxies and an attempt to reproduce their spectra with photo-ionization models using CLOUDY code. Recently, surveys as SDSS increased data archives permitting statistic investigations. At the same time the improvement of the computer calculus capacity and velocity allows us to develop complex models (the time required for our models is around 1 CPU month, ~ 40000 models). An accurate analysis was performed on 3153 Seyfert spectra obtained from SDSS-DR7. The physical parameters were directly measured or derived by composite (with two clouds) photo-ionization models.

The main achievements obtained in this thesis are summarized in five fundamental points.

1. Object selection with the O_{123} diagram. This diagram is able to separate very well Seyfert galaxies from the other emission line galaxies. It is possible to use this diagram even if the ratios are not corrected by reddening. The reddening acts only with a rigid displacement of the point distribution. It is important to note that the Kewley et al. (2006) Seyfert classification is absolutely consistent with our classification.

2. Multi-Gaussian fitting code, GGFIT. The code is based on the nonlinear least square fitting method. The code is able to fit complex features as H_α with narrow and broad components and $[NII]6548, 6584$.

3. Classification of the Seyfert spectra. From the SDSS-DR7 we selected 5678 spectra, they were measured with GGFIT code. The spectra were classified as narrow or broad by analysing the number of H_α components and their $FWHM$, then with Veilleux and Osterbrock diagrams 3153 Seyfert galaxies were extracted. Their spectra were divided in three samples, Seyfert 2 (S2), Seyfert 2b (S2b), a sample characterized by a possible weak broad component, that the SDSS spectral resolution does not allow to clearly disentangle, and finally Intermediate-type Seyfert (I-t).

4. Comparison of spectroscopic and physical properties between the samples.

   (a) The Av distribution shows a stronger reddening for S2 and S2b compared to I-t, the Av median values are respectively 1.5 for the first two samples and 1 for I-t. The stellar Av, found by STARLIGHT, is lower than the Av obtained by the Balmer decrement and weakly correlated.

   (b) The number of spectra with both $[OIII]5007, 4959$ lines fitted by two components is higher ($\sim$ 60%) in S2b and I-t compared to S2 ($\sim$ 25%). The $[OIII]5007$ luminosity is higher when an asymmetry is present and two Gaussian components are necessary for the fitting, the median value is $log(L) \sim 41.5\ erg/sec$, whereas it is $log(L) \sim 40\ erg/sec$ when a single Gaussian is used.

   (c) All the samples show good correlation between the lines having similar ionization potential.

   The distributions of the line intensities, relative to H_β, are always similar between S2 and S2b or between S2b and I-t, only in few cases they are common for all the samples. Therefore S2b sample shows that the relative line intensities are intermediate between S2 and I-t sample.

(d) The $[FeVII]$ coronal lines are detected in few cases in S2, about $\sim$ 1%, the number increases in S2b and I-t, $\sim 7-9\%$. The correlation coefficient between $log([OIII]4363/[OIII]5007)$ and $log([FeVII]6087/[OIII]5007)$ is ~ 0.6 for S2 and S2b and ~ 0.4 for I-t. Notwithstanding the similar critical density the detection of these lines is not correlated, $[FeVII]$ and $[OIII]4363$ may be formed in different regions or via different mechanisms: the coronal lines may be originated in shocks or in a very low density medium with high temperature.

(e) The $[ArIV]4711, 4740$ lines, useful to determine the density, are very rare independently of the samples. The critical density of these lines are $2.5 \cdot 10^4$ and $4 \cdot 10^5$ cm^{-3} for 4711 and 4740 respectively. Therefore the absence of $[ArIV]$ doublet supports the hypothesis of a low density medium ($1 - 10\ cm^{-3}$) surrounding filaments or clouds with high density ($> 4 \cdot 10^5 cm^{-3}$). The high density should be able to suppress $[ArIV]$ lines by collisional processes. However argon abundance is two orders of magnitude lower than oxygen abundance, thus $[ArIV]$ lines could also not be formed in a low density medium.

(f) The electron temperatures of $[OIII]$ are on average higher ($\sim$ 15000K) than those usually assumed in the photo-ionization case. $T_e[OIII]$ lower than 13000K, consistent with $T_e[OII]$ and $T_e[SII]$, is obtained if it is assumed a density of $1 \times 10^5\, cm^{-3}$. At least a two phase medium with low and high density is present.

(g) Only low ionization and Balmer lines in S2 show a correlation between their $FWHM$ and stellar velocity dispersion (σ_*). The other samples show a weak or even absent correlation. Only the low ionized regions move in the gravitational potential of the bulge. About 80% of the three samples show a mean $FWHM$ between 200 and 400 km/s.

(h) From the $[OIII]5007$ profile analysis we found that the narrow component has a mean value around 200 km/s whereas the 2nd component 600 km/s. S2 have always lower $FWHM$ in both the components, overall for the 2nd component. The $[OIII]5007$ 2nd component shows, in the vast majority of the cases ($\sim$ 75%), a blue shift and this is consistent with the asymmetry measures. There is no correlation between H_β and $[OIII]5007$ asymmetry with the exception of few cases ($< 10\%$). We introduce an other asymmetry parameter, the peak difference (pd) between the two fitted components: this is well correlated with the classical asymmetry parameter, A, introduced by Whittle (1985).

(i) With the assumption of a mean uniform distribution density of 10 cm^{-3}, the estimated ionized gas mass is on average around $3 \cdot 10^7 M_\odot$. From the pd parameters of H_β vs $[OIII]5007$ results that the most probable $F_{[OIII]5007}/F_{H_\beta}$ 2nd component ratio value is 10. From this value we calculate that about 1/3 of the total ionized mass has a bulk motion (a typical velocity value is 100 km/s).

(j) The turbulent energy is in the range $10^{54} - 10^{56} erg$, the kinetic bulk energy is an order of magnitude lower then the previous one instead the thermal energy is two order of magnitude lower.

(k) Assuming a density of 10 cm^{-3} the NLR radii are in the range $300 - 2000 pc$ and the dynamical time-scale is in the range $3 - 30 \cdot 10^6\, yr$.

(l) A lower limit of the accretion rate is found from the input momentum rate, assuming that the bulk motion of the 2nd component mass is directly powered by the BH. The range values is $0.0003 < \dot{M}_{acc} < 0.03 M/M_\odot$.

5. The models of the observed spectra.

   (a) Two-clouds models work reasonably well with S2 ($\sim$ 50%), whereas S2b and I-t samples are well fitted with less probability ($\sim$ 30%). Maybe in these cases a cloud with higher ionization level is necessary. Single clouds models are not very reliable, being able to fit spectra with a low number of measured lines (< 12), that is with low S/N ratio. So they give only apparently good results.

   (b) Dust-to-gas (D/G) values of 0.75 and 1 give the best χ^2 and the higher number of fitted spectra for the S2 sample. This means that with these abundance sets the D/G has about the Galactic ISM value or slightly lower.

   (c) The S2 power-law index is slightly lower than that obtained in I-t case and it is consistent with values ($\alpha \sim -2$) found in literature.

   (d) The metallicity is generally solar or super-solar for all the samples ($1 - 2.5\ Z/Z_{\odot}$).

   (e) Assuming the model line fluxes as empirical spectra, we compared the models with published data in the UV and NIR range. The main result is a good match in NIR, with a D/G ratio between 0.75 and 1.0. On the contrary, in UV range we did not obtain a good match. In this range the D/G must be reduced to 0.25 or less.

We can conclude that this work supports the local origin of the gas in the NLR of Seyfert galaxies. The obtained metallicity in these samples confirms that the Seyfert galaxies with low metallicity are really rare. It could be interesting to analyze the objects in the low metallicity region of the metallicity diagnostic diagram $[NII]6584/[OII]3727$ vs $[NII]6584/[SII]6724$ at different red-shift. A more sophisticated modelization of the NLR, multi-phase models (high and low ionization clouds respectively with high and low density distributions) and more resolution in the input parameters, should be able to get a larger number of matched spectra. The methods applied here, regarding the comparison between models and observed spectra, are just a suggestion of what it should be possible to do with a multi-processor machine.

We give three main suggestions about a natural continuation of this work: the first one should be the extension of data collection in UV and NIR from literature, in order to better test our models; the second one is observations of nearby Seyferts with NIR integral field spectroscopy, which should permit us to analyse in detail the D/G distribution inside the NLR; finally, the third consists of extending this analysis to higher redshift objects.

Bibliography

Abazajian, K. N. et al. 2009, ApJS, 182, 543

Afanasiev, V. L., Dodonov, S. N., Khrapov, S. S., Mustsevoi, V. V., & Moiseev, A. V. 2007, Astrophysical Bulletin, 62, 1

Aller, L. H., ed. 1984, Astrophysics and Space Science Library, Vol. 112, Physics of thermal gaseous nebulae

Alonso-Herrero, A., Rieke, M. J., Rieke, G. H., & Ruiz, M. 1997, ApJ, 482, 747

Antonucci, R. 1993, ARA&A, 31, 473

Antonucci, R. R. J. & Miller, J. S. 1985, ApJ, 297, 621

Asplund, M., Grevesse, N., & Sauval, A. J., eds. 2005, Astronomical Society of the Pacific Conference Series, Vol. 336, The Solar Chemical Composition

Baldwin, J. A., Phillips, M. M., & Terlevich, R. 1981, PASP, 93, 5

Bennert, N., Jungwiert, B., Komossa, S., Haas, M., & Chini, R. 2006, A&A, 456, 953

Bennert, N., Jungwiert, B., Komossa, S., Haas, M., & Chini, R. 2007, in Astronomical Society of the Pacific Conference Series, Vol. 373, The Central Engine of Active Galactic Nuclei, ed. L. C. Ho & J.-W. Wang, 521–+

Binette, L., Wang, J., Villar-Martin, M., Martin, P. G., & Magris C., G. 1993, ApJ, 414, 535

Binette, L., Wilson, A. S., & Storchi-Bergmann, T. 1996, A&A, 312, 365

Botte, V., Ciroi, S., Rafanelli, P., & Di Mille, F. 2004, AJ, 127, 3168

Bruzual, G. & Charlot, S. 2003, MNRAS, 344, 1000

Burles, S., Pope, A., Uomoto, A., Nichol, R., Merrelli, A., Brinkmann, J., Castander, F., Schlegel, D., & SDSS Collaboration. 1999, in Bulletin of the American Astronomical Society, Vol. 31, Bulletin of the American Astronomical Society, 1501–+

Capetti, A., Axon, D. J., Macchetto, F. D., Marconi, A., & Winge, C. 1999, ApJ, 516, 187

Cardelli, J. A., Clayton, G. C., & Mathis, J. S. 1989, ApJ, 345, 245

Cid Fernandes, R., Heckman, T., Schmitt, H., González Delgado, R. M., & Storchi-Bergmann, T. 2001, ApJ, 558, 81

Cid Fernandes, R., Mateus, A., Sodré, L., Stasińska, G., & Gomes, J. M. 2005, MNRAS, 358, 363

Ciroi, S., Afanasiev, V. L., Moiseev, A. V., Botte, V., Di Mille, F., Dodonov, S. N., Rafanelli, P., & Smirnova, A. A. 2005, MNRAS, 360, 253

Colina, L. 1993, ApJ, 411, 565

Contini, T., Treyer, M. A., Sullivan, M., & Ellis, R. S. 2002, VizieR Online Data Catalog, 733, 75

Corsini, E. M., Pizzella, A., Sarzi, M., Cinzano, P., Vega Beltrán, J. C., Funes, J. G., Bertola, F., Persic, M., & Salucci, P. 1999, A&A, 342, 671

Das, V., Crenshaw, D. M., & Kraemer, S. B. 2007, ApJ, 656, 699

Deo, R. P., Crenshaw, D. M., Kraemer, S. B., Dietrich, M., Elitzur, M., Teplitz, H., & Turner, T. J. 2007, ApJ, 671, 124

Dimitrijević, M. S., Popović, L. Č., Kovačević, J., Dačić, M., & Ilić, D. 2007, MNRAS, 374, 1181

Dopita, M. A. & Sutherland, R. S. 1995, ApJ, 455, 468

Everett, J. E. & Murray, N. 2007, ApJ, 656, 93

Falcke, H., Wilson, A. S., Simpson, C., & Bower, G. A. 1996, ApJ, 470, L31+

Ferland, G. J., Korista, K. T., Verner, D. A., Ferguson, J. W., Kingdon, J. B., & Verner, E. M. 1998, PASP, 110, 761

Ferruit, P., Wilson, A. S., Falcke, H., Simpson, C., Pécontal, E., & Durret, F. 1999, MNRAS, 309, 1

Fu, H. & Stockton, A. 2006, ApJ, 650, 80

—. 2007, ApJ, 666, 794

Ghosh, H., Pogge, R. W., Mathur, S., Martini, P., & Shields, J. C. 2007, ApJ, 656, 105

Greene, J. E. & Ho, L. C. 2005, ApJ, 627, 721

Groves, B. A., Dopita, M. A., & Sutherland, R. S. 2004, ApJS, 153, 9

Groves, B. A., Heckman, T. M., & Kauffmann, G. 2006, MNRAS, 371, 1559

Haas, M., Siebenmorgen, R., Pantin, E., Horst, H., Smette, A., Käufl, H., Lagage, P., & Chini, R. 2007, A&A, 473, 369

Hamann, F., Korista, K. T., Ferland, G. J., Warner, C., & Baldwin, J. 2002, ApJ, 564, 592

Heckman, T. M., Miley, G. K., van Breugel, W. J. M., & Butcher, H. R. 1981, ApJ, 247, 403

Heisler, C. A. & De Robertis, M. M. 1999, AJ, 118, 2038

Hicks, E. K. S., Davies, R. I., Malkan, M. A., Genzel, R., Tacconi, L. J., Sánchez, F. M., & Sternberg, A. 2009, ApJ, 696, 448

Hill, T. L., Heisler, C. A., Sutherland, R., & Hunstead, R. W. 1999, AJ, 117, 111

Ho, L. C. 2009, ApJ, 699, 638

Izotov, Y. I., Stasińska, G., Meynet, G., Guseva, N. G., & Thuan, T. X. 2006, A&A, 448, 955

Izotov, Y. I. & Thuan, T. X. 1999, ApJ, 511, 639

—. 2008, ApJ, 687, 133

Kewley, L. J., Groves, B., Kauffmann, G., & Heckman, T. 2006, MNRAS, 372, 961

Komossa, S. & Schulz, H. 1997, A&A, 323, 31

Komossa, S., Xu, D., Zhou, H., Storchi-Bergmann, T., & Binette, L. 2008, ApJ, 680, 926

Koski, A. T. 1978, ApJ, 223, 56

Kraemer, S. B., Bottorff, M. C., & Crenshaw, D. M. 2007, ApJ, 668, 730

Kraemer, S. B., Trippe, M. L., Crenshaw, D. M., Meléndez, M., Schmitt, H. R., & Fischer, T. C. 2009, ApJ, 698, 106

Kriss, G., Krolik, J., Grimes, J., Tsvetanov, Z., Espey, B., Zheng, W., & Davidsen, A. 1997, in Astronomical Society of the Pacific Conference Series, Vol. 113, IAU Colloq. 159: Emission Lines in Active Galaxies: New Methods and Techniques, ed. B. M. Peterson, F.-Z. Cheng, & A. S. Wilson, 453–+

Kuraszkiewicz, J. K., Green, P. J., Crenshaw, D. M., Dunn, J., Forster, K., Vestergaard, M., & Aldcroft, T. L. 2004, ApJS, 150, 165

Kwok, S. 2007, Physics and Chemistry of the Interstellar Medium, ed. S. Kwok

La Mura, G., Popović, L. Č., Ciroi, S., Rafanelli, P., & Ilić, D. 2007, ApJ, 671, 104

Lamassa, S., Heckman, T., Ptak, A., Hornschemeier, A., Martins, L., Sonnentrucker, P., & Tremonti, C. 2009, in Chandra's First Decade of Discovery, Proceedings of the conference held 22-25 September, 2009 in Boston, MA. Edited by Scott Wolk, Antonella Fruscione, and Douglas Swartz, abstract #140, ed. S. Wolk, A. Fruscione, & D. Swartz

Lawrence, A. 1987, PASP, 99, 309

Mainieri, V. et al. 2007, ApJS, 172, 368

Martin, P. G. & Rouleau, F. 1991, in Extreme Ultraviolet Astronomy, ed. R. F. Malina & S. Bowyer, 341–+

Martini, P., Regan, M. W., Mulchaey, J. S., & Pogge, R. W. 2003a, ApJS, 146, 353

—. 2003b, ApJ, 589, 774

Mathis, J. S. & Rosa, M. R. 1991, A&A, 245, 625

Miyaji, T., Wilson, A. S., & Perez-Fournon, I. 1992, ApJ, 385, 137

Mollá, M. & Hardy, E. 2002, AJ, 123, 3055

Murayama, T. & Taniguchi, Y. 1998, ApJ, 497, L9+

Nagao, T., Murayama, T., Shioya, Y., & Taniguchi, Y. 2003, AJ, 125, 1729

Nagao, T., Murayama, T., & Taniguchi, Y. 2001, PASJ, 53, 629

Nelson, C. H. & Whittle, M. 1996, ApJ, 465, 96

Netzer, H. 2008, New Astronomy Review, 52, 257

Nisini, B., Bacciotti, F., Giannini, T., Massi, F., Eislöffel, J., Podio, L., & Ray, T. P. 2005, A&A, 441, 159

Oliva, E., Marconi, A., & Moorwood, A. F. M. 1999, A&A, 342, 87

Osterbrock, D. E. 1978, Lick Observatory Bulletin, 775, 1

Osterbrock, D. E. & Ferland, G. J. Astrophysics of gaseous nebulae and active galactic nuclei, ed. , D. E. OsterbrockG. J. Ferland

Osterbrock, D. E., Tran, H. D., & Veilleux, S. 1992, ApJ, 389, 196

Ozaki, S. 2009, PASJ, 61, 259

Padovani, P. & Matteucci, F. 1993, ApJ, 416, 26

Pilyugin, L. S. & Thuan, T. X. 2005, ApJ, 631, 231

Pogge, R. W. 1988, ApJ, 332, 702

—. 1989, ApJ, 345, 730

Pogge, R. W. & De Robertis, M. M. 1993, ApJ, 404, 563

Radovich, M., Rafanelli, P., & Barbon, R. 1998, A&A, 334, 124

Rafanelli, P., Vaona, L., Ciroi, S., & Di Mille, F. 2008, Journal of Physics Conference Series, 133, 012026

Ramos Almeida, C., Pérez García, A. M., Acosta-Pulido, J. A., Rodríguez Espinosa, J. M., Barrena, R., & Manchado, A. 2006, ApJ, 645, 148

Rice, M. S., Martini, P., Greene, J. E., Pogge, R. W., Shields, J. C., Mulchaey, J. S., & Regan, M. W. 2006, ApJ, 636, 654

Riess, A. G. et al. 2009, ApJ, 699, 539

Riffel, R., Rodríguez-Ardila, A., & Pastoriza, M. G. 2006, A&A, 457, 61

Robinson, A. et al. 1994, A&A, 291, 351

Rosario, D. J., Whittle, M., Nelson, C. H., & Wilson, A. S. 2008, Memorie della Societa Astronomica Italiana, 79, 1217

Schartmann, M., Meisenheimer, K., Klahr, H., Camenzind, M., Wolf, S., & Henning, T. 2009, MNRAS, 393, 759

Schulz, H., Komossa, S., Schmitz, C., & Mücke, A. 1999, A&A, 346, 764

Shields, J. C. & Filippenko, A. V. 1990, AJ, 100, 1034

Smirnova, A. A., Gavrilović, N., Moiseev, A. V., Popović, L. Č., Afanasiev, V. L., Jovanović, P., & Dačić, M. 2007, MNRAS, 377, 480

Storchi-Bergmann, T., Mulchaey, J. S., & Wilson, A. S. 1992, ApJ, 395, L73

Storchi-Bergmann, T., Schmitt, H. R., Calzetti, D., & Kinney, A. L. 1998, AJ, 115, 909

Tadhunter, C. & Tsvetanov, Z. 1989, Nature, 341, 422

Temporin, S., Ciroi, S., Rafanelli, P., Radovich, M., Vennik, J., Richter, G. M., & Birkle, K. 2003, ApJS, 148, 353

Tsvetanov, Z. & Walsh, J. R. 1992, ApJ, 386, 485

Unger, S. W., Pedlar, A., Axon, D. J., Whittle, M., Meurs, E. J. A., & Ward, M. J. 1987, MNRAS, 228, 671

van Zee, L. & Haynes, M. P. 2006, ApJ, 636, 214

van Zee, L., Salzer, J. J., Haynes, M. P., O'Donoghue, A. A., & Balonek, T. J. 1998, AJ, 116, 2805

Veilleux, S., Cecil, G., & Bland-Hawthorn, J. 2005, ARA&A, 43, 769

Veilleux, S., Goodrich, R. W., & Hill, G. J. 1997, ApJ, 477, 631

Veilleux, S. & Osterbrock, D. E. 1987, ApJS, 63, 295

Veilleux, S., Tully, R. B., & Bland-Hawthorn, J. 1993, AJ, 105, 1318

Vila Costas, M. B. & Edmunds, M. G. 1993, MNRAS, 265, 199

Villar-Martín, M., Humphrey, A., Martínez-Sansigre, A., Pérez-Torres, M., Binette, L., & Zhang, X. G. 2008, MNRAS, 390, 218

Vladilo, G. 2002, ApJ, 569, 295

Wagner, S. J. 1997, in Astronomical Society of the Pacific Conference Series, Vol. 113, IAU Colloq. 159: Emission Lines in Active Galaxies: New Methods and Techniques, ed. B. M. Peterson, F.-Z. Cheng, & A. S. Wilson, 298–+

Wall, J. V. & Jenkins, C. R. Practical Statistics for Astronomers, ed. , J. V. WallC. R. Jenkins

Walsh, J. L., Barth, A. J., Ho, L. C., Filippenko, A. V., Rix, H., Shields, J. C., Sarzi, M., & Sargent, W. L. W. 2008, AJ, 136, 1677

Wang, J. & Zhang, E. 2007, ApJ, 660, 1072

Whittle, M. 1985, MNRAS, 213, 1

Whittle, M., Rosario, D. J., Silverman, J. D., Nelson, C. H., & Wilson, A. S. 2005, AJ, 129, 104

Wilson, A. S. 1992, in Physics of Active Galactic Nuclei, ed. W. J. Duschl & S. J. Wagner, 307–+

Wilson, A. S. 1997, in Astronomical Society of the Pacific Conference Series, Vol. 113, IAU Colloq. 159: Emission Lines in Active Galaxies: New Methods and Techniques, ed. B. M. Peterson, F.-Z. Cheng, & A. S. Wilson, 264–+

Wilson, A. S. & Tsvetanov, Z. I. 1994, AJ, 107, 1227

Wilson, A. S., Wu, X., Heckman, T. M., Baldwin, J. A., & Balick, B. 1989, ApJ, 339, 729

Yonehara, A. 2006, ApJ, 646, 16

Zhang, K., Wang, T., Dong, X., & Lu, H. 2008, ApJ, 685, L109

Acknowledgements

This research has made use of:

- SDSS-DR7 for the spectra selection. *Funding for the SDSS and SDSS-II has been provided by the Alfred P. Sloan Foundation, the Participating Institutions, the National Science Foundation, the U.S. Department of Energy, the National Aeronautics and Space Administration, the Japanese Monbukagakusho, the Max Planck Society, and the Higher Education Funding Council for England. The SDSS Web Site is http://www.sdss.org/. The SDSS is managed by the Astrophysical Research Consortium for the Participating Institutions. The Participating Institutions are the American Museum of Natural History, Astrophysical Institute Potsdam, University of Basel, University of Cambridge, Case Western Reserve University, University of Chicago, Drexel University, Fermilab, the Institute for Advanced Study, the Japan Participation Group, Johns Hopkins University, the Joint Institute for Nuclear Astrophysics, the Kavli Institute for Particle Astrophysics and Cosmology, the Korean Scientist Group, the Chinese Academy of Sciences (LAMOST), Los Alamos National Laboratory, the Max-Planck-Institute for Astronomy (MPIA), the Max-Planck-Institute for Astrophysics (MPA), New Mexico State University, Ohio State University, University of Pittsburgh, University of Portsmouth, Princeton University, the United States Naval Observatory, and the University of Washington. (http://www.sdss.org/dr7/)*

- IRAF for the spectra preparation. IRAF is the Image Reduction and Analysis Facility, a general purpose software system for the reduction and analysis of astronomical data. *IRAF is distributed by the National Optical Astronomy Observatories, which are operated by the Association of Universities for Research in Astronomy, Inc., under cooperative agreement with the National Science Foundation. (http://iraf.noao.edu/)*

- NED provided the object extinctions (E_{B-V}) : *NASA/IPAC Extragalactic Database (NED) which is operated by the Jet Propulsion Laboratory, California Institute of Technology, under contract with the National Aeronautics and Space Administration. (http://nedwww.ipac.caltech.edu/)*

- CLOUDY, photoionization code for the calculus of the models: *Calculations were performed with version 06.02 of Cloudy, last described by Ferland et al. (1998). The citation is the following review paper in PASP Ferland et al. (1998). (http://www.nublado.org/)*

- STARLIGHT, spectral syntesis code used in the subtracting the stellar continuum from the spectra: *The STARLIGHT project is supported by the Brazilian agencies CNPq, CAPES and FAPESP and by the France-Brazil CAPES/Cofecub program. (http://www.starlight.ufsc.br/)*

- TOPCAT, Tool for OPerations on Catalogues And Tables, used in the preparation of tables and figures. *The program is available under the GNU General Public Licence. It was initially developed within the now-terminated Starlink project in the UK, and was more recently developed and supported by its author as part of the AstroGrid project. Its underlying table processing facilities are provided by STIL (http://www.star.bris.ac.uk/ mbt/topcat/).*